Investigation of the Optical Properties of Nanostructured Transparent Conducting Oxides

by

Ting Wang

A thesis
presented to the University of Waterloo
in fulfillment of the
thesis requirement for the degree of
Doctor of Philosophy
in
Chemistry

Waterloo, Ontario, Canada, 2013

AUTHOR'S DECLARATION

I hereby declare that I am the sole author of this thesis. This is a true copy of the thesis, including any required final revisions, as accepted by my examiners.

I understand that my thesis may be made electronically available to the public.

Ting Wang

Abstract

Transparent conducting oxides (TCOs) usually have high conductivity and transparency in the visible range and have been widely used in daily life. Recently, TCOs have attracted great interest due to their potential applications in various new optical and electrical devices (flat-panel displays, energy efficient windows, etc.). Nanostructured TCOs can induce new size related properties, for example, when sizes of TCOs are controlled at the nanometer scale, various defects can introduce different defect-related optical emissions. These new nanostructured TCOs combining traditional and new size dependent properties may be used for construction of next generation optical devices.

To investigate the optical properties of TCOs at nanoscale, in this thesis, several new kinds of colloidal nanocrystals (NCs) of TCOs have been synthesized and their optical emission and transparency have been explored. The first part of my work focuses on ITO (indium tin oxide) NCs demonstrates phase and size dependence of surface plasmon absorption in the near infrared region. The second part of the thesis describes colloidal synthesis of γ-Ga_2O_3 with size tunable photoluminescence, further study reveals that the photoluminescence is defect related and can be tuned by changing the defect concentration. In the last part of my study, I develop a methodology for lanthanide doped γ-phase Ga_2O_3 NCs and reveal tunable chromaticity of the lanthanide doped NCs.

Homogeneous colloidal ITO NCs with various Sn doping level can be prepared in a simple solution method. By controlling initial Sn doping concentration, rhombohedral or cubic phase ITO nanocrystals can be synthesized. Different NC phases show dramatic difference in electrical and optical properties. Cubic ITO NCs show strong absorption in the near infrared region arising from the surface plasmons. Free electron concentration is related to the difference in donor states related to tin dopants. With higher donor activation energy in rhombohedral phase NCs, free electron concentration in reduced in the conduction band. The increased replacement of organic protective ligands by anions in solution leads to oriented attachment of larger NCs and forms flower shape clusters. These results demonstrate tuning of the optical and electrical properties of complex oxide NCs by selecting their crystal and electronic structures through size and composition and allow for a designed preparation and controlled self-assembly of ITO NCs.

Also, I report colloidal synthesis of gallium oxide NCs with γ phase crystal structure and uniform size distribution. As synthesized NCs exhibit size tunable photoluminescence from purple to blue. With increasing NC size, emission shifts to lower energies. The optical emission is dominated by

defect related donor-acceptor pair recombination and has lifetime of milliseconds. Also, the phosphorescence decay rate increases with decreasing NC size. The defect related photoluminescence efficiency can be controlled by changing the reaction environment. A reducing environment leads to an increase in emission intensity by increasing the oxygen vacancy concentration, while blue emission is suppressed under oxidizing conditions. These results allow for a rational and predictable tuning of the optical properties. These defect-related donors are implicated in electrical conductivity rendering gallium oxide NCs promising materials for optoelectronic devices.

For further understanding the defect-related photoluminescence in colloidal TCO NCs, we implement steady-state and time-resolved luminescence studies and to address the role for NC size, structure, defects and surface capping on the PL energy, efficiency and dynamics. The strong blue emission with a quantum yield of ~25 % is oxygen vacancy related and can be assigned to donor-acceptor pair recombination. The emission energy and photoluminescence lifetime can be determined by donor and acceptor binding energies and Coulombic interactions between donors and acceptors. Low temperature luminescence measurements reveal that the donor and acceptor binding energies are also size dependent. Large sized NCs (diameter ~6.0 nm) have a binding energy around 205 meV increasing by ca. 30 meV in diameter 3.0 nm NCs. Surface defects can also influence donor acceptor recombination by trapping valence band holes. The removal of the surface defects can effectively eliminate surface hole-trapping and enhance the donor acceptor pair emission. This part of the mechanistic study of the donor acceptor pair recombination can be useful for introducing and manipulating photoluminescence properties in oxide nanostructures by tuning native defect interactions.

In the last part of my thesis I describe my research on europium (Eu)-doped γ-phase Ga_2O_3 NCs. Nanocrystals with varying Eu^{3+} concentration have been synthesized and the optical properties of these colloidal nanocrystals have been investigated. Steady state and time resolved emission spectra were collected. In the time resolved spectrum, emission shows a combination of two identical features in the blue and red spectral range. The broad blue emission originates from defects related to donor acceptor pair recombination with a life time of 4-6μs. Sharp narrow red emission arises from lanthanide f-f transitions and has a life time about 1-3 ms. Two characteristic decay rates allow for tuning of the relative intensities and sample chromaticity by tuning delay time or gate time. The nanocrystals, exhibiting time tunable dual emission, may have potential applications in biosensing, imaging and time sensitive optical devices.

Acknowledgements

As a true scientist, Professor Pavle V. Radovanovic has strong faith in science and quite devoted to scientific research. Luckily, I can do my PhD in his group. Under his supervision, I learned how to explore the world of nanoscience and learn how to investigate the scientific obstacle by logical design and accurate experiment. His spirit towards truth and his interest in exploring the unknown inspires me to further my study. His continuous guidance, encourage and support help me grow in the right direction and experience real pleasure while solving scientific problems.

I sincerely thank all my committee members, Professor Holger Kleinke, Professor Eric Prouzet and Professor Dmitriy Soldatov for their advice and help during my study. I would also like to thank Professor Bo Cui from Electrical and Computer Engineering Department and Professor Byron Gates from Simon Fraser University for their precious time and kindness being my external committee members.

I am very grateful to my fellows in the group: Shokouh Farvid, Melanie Chiu, Manu Hegde, Tahereh Sabergharesou, Vadim Chermanov and my previous labmates Ian Hosein, Vladimir Blagojevic, Ling Ju, Neeshma Dave, Abulikemu Mutalifu, and Hongyu Wu for their friendship and help in the research progress. Their kind help and support makes the lab such a comfort place to stay.

Also, I would like to thank Fred Pearson from McMaster University for all wonderful TEM measurements. Many thanks to Liyan Zhao in Prof. Tong Leung's group for all XPS measurement. I would also like to thank group members in Prof. Kleinke's group for their help in XRD measurements and Randy Fagan for assistance in previous Raman spectroscopies.

I would like to thank my parents for their support and understanding through my PhD study. Also, special thanks to my wife congcong, for her love, patience and understanding of my research.

Table of Contents

List of Figures

List of Tables

List of Abbreviations

acac	Acetylacetonate
bcc	Body-centered cubic
BE	Bound exciton
CIE	Commission Internationale De L′E′clairage
DAP	Donor acceptor pair
DDA	1-Dodecylamine
ED	Electric dipole
EDX	Energy dispersive X-ray spectrum
FRET	Forster resonant energy transfer
FTIR	Fourier transform infrared spectroscopy
ITO	Indium tin oxide
LED	Light-emitting diode
LLP	Limited ligand protection
MD	Magnetic dipole
NC	Nanocrystal
NIR	Near infrared
OA	Oleylamine
PL	Photoluminescence
QBS	Quinine bisulfate
rh	Rhombohedral
TCO	Transparent conducting oxide
TOPO	Trioctylphosphine oxide
TEM	Transmission electron microscopy
UV	Ultraviolet
XANES	X-ray absorption near-edge structure
XPS	X-ray photoelectron spectroscopy
XRD	X-ray diffraction

Chapter 1 Introduction

Transparent conducting oxides (TCO) have been attracting scientific and practical interest because of their transparency, as well as a range of crystal lattice structures and technologically relevant properties [1,2]. Among TCOs , ITO (Indium Tin Oxide) and gallium oxide are widely known to be wide band gap semiconductors exhibiting both high conductivity [3] and optical transparency [4,5]. Owing to their unique properties they can be used in optoelectronics, including the development of inexpensive light-emitting diodes (LEDs) and displays [6], as well as for sensors [7] and photocatalysts [8]. Recently, a large amount of research has been focused on nanostructured TCOs since these materials combine traditional and new size dependent properties. This combination of properties allows for the design of novel multifunctional devices.

The electrical conductivity and optical emissions of TCOs can be induced by intrinsic defects or extrinsic dopants. In this chapter, using ITO as an example, the principle optical and electrical properties of TCOs will be given, and it can help understanding my research on ITO nanocrytals. I will also discuss the importance of defects on induced luminescence in these materials through the concept of DAP (Donor Acceptor Pair) recombination. Defects induced DAP recombination is the main mechanism for explain in the light emission in γ-phase Ga_2O_3. Finally, I will review the mechanisms of lanthanide-doped semiconductors, which will help in understanding the third part of my research on lanthanide doped Ga_2O_3.

1.1 Electrical and Optical Properties of TCOs, Using ITO as an Example

Since the first observation of both electrical conductivity and transmittance in cadmium oxide (CdO) in 1907, people have a continuing interest in finding new types of transparent conducting oxides (TCO) [9]. After years of extensive research and emerging number of TCOs explored

(oxides of Cd, Sn, Zn and their alloys), Indium tin oxide (ITO, with Sn doped in indium oxide) is believed to be the best among TCOs based on its reported transmittance and conductivity. As such has found various applications in electronic, opto-electronic and mechanical devices [10]. This part of the introduction will largely focus on ITO as a model system.

1.1.1 Optical Properties of ITO

Transmission of visible light is an important feature of TCO materials. High transparency between 400 nm and 700 nm is crucial for many practical applications. ITO materials can have a transparency around 95 % in the visible light range, which is ideal for transparent optical device [11].

A typical transmittance spectrum of TCOs is shown in **Figure 1.1**. At the high energy range (left part of the spectrum), the TCOs show strong near band edge absorption, and at low energy side (right part of the spectrum) a strong reflection. Between these two regions where the light is absorbed or reflected, there is a transparent region which is defined as the transmission window.

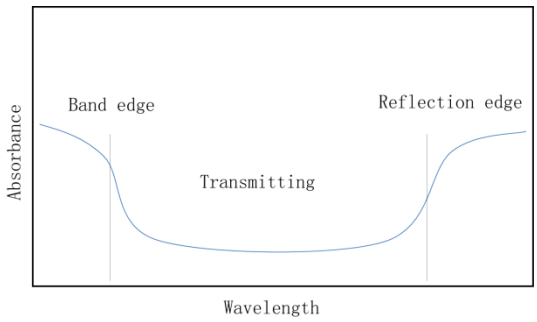

Figure 1.1 Absorption spectrum of a typical transparent conducting oxide.

In the near UV part, the photon energy is high enough and comparable to the bandgap of the TCOs (usually 3-4 eV), the light can be absorbed by the material and electrons in TCO can be excited from valence band to conduction band. In this process, no light can be transmitted. For ITO, the bandgap is around 4 eV which means this near band edge absorption can occur between 300 nm to 400 nm, leaving the transmission window widely open.

In the long wavelength range, other than absorption, the light is reflected due to electronic plasmon resonance and this kind of phenomenon can be explained by the Drude free electron theory [12]. In the Drude free electron model, in a given electromagnetic field, the electric field

will cause the electron oscillation (known as the plasmon). This plasmon can oscillate at a certain frequency. The wavelength of this oscillation is usually around 1,000 nm to 3,000 nm [13], which is the reflection edge in **Figure 1.1**. Also, the plasmon resonance can influence the dielectric constant, which directly relates to optical properties:

$$\sqrt{\varepsilon} = n + ik \quad \textbf{(eq 1.1)}$$

In this equation, the real part n stands for the refractive index and k is the extinction coefficient. With different n and k values, the dielectric constant is different and influences the reflection and absorption directly. At longer wavelengths (larger than the reflection edge), the extinction coefficient is large and the material has a constant reflectance. In the transmission window region, the k value is almost zero and the absorption is very small. The refractive index n is almost constant and has a relationship with frequency of the electromagnetic field as following:

$$n = \sqrt{\varepsilon_\infty}\sqrt{1 - (\omega_R/\omega)^2} \quad \textbf{(eq 1.2)}$$

Here, ε_∞ is the relative permittivity when frequency is high, and ω_R is the frequency at reflection edge [14]. When $\omega > \omega_R$, the second part on the right of the equation can be estimated as 1, refractive index n is just the square root of the high frequency permittivity ε_∞.

In real optical experiments, the value of n and k cannot be measured directly. Instead, we can measure the normal incidence reflectivity R and absorption coefficient α and using the following equation to determine the n and k values:

$$R = \frac{(1-n)^2+k^2}{(1+n)^2+k^2} \quad \textbf{(eq 1.3)}$$

$$\alpha = \frac{2\omega k}{c} \quad \textbf{(eq 1.4)}$$

Also, for the transparency measurement, taken a thin film as an example, the following equation can be used:

$$T = (1 - R)e^{-\alpha d} \quad \textbf{(eq 1.5)}$$

Here, d is the thickness of the film, since the absorption coefficient α has a direct relationship with frequency, with a different excitation wavelength, the transmittance is different [15].

1.1.2 Electrical Properties of ITO and the Correlation with Optical Properties

For a free electron, we can consider its energy as the following equation:

$$E = \frac{\hbar^2 k^2}{2m} \quad \textbf{(eq 1.6)}$$

In this equation, m is the mass of the electron and k stands for the vector of the electron momentum at a certain eigenstate.

When we consider electrons in the crystal lattice, lattice periodicity must be taken into consideration. For wavevector k=±π/a, the energy will have a splitting, and this energy difference is the band gap E_g. With enough excitation energy, the electrons at the top of the valence band can be excited to the bottom of the conduction band, when electrons with vector k near k_m, the energy of the electrons can be:

$$E(k) \simeq E(k_m) + (\frac{\partial^2 E}{\partial k^2})_{k=k_m} k^2 \quad \textbf{(eq 1.7)}$$

This kind of energy dispersion is the same as dispersion of a free electron. So the electron at the top of the valence band or bottom of the conduction band acts as free electron with effective mass m*.

The conductivity of a material is defined by the following equation:

$$\sigma = ne\mu \quad \textbf{(eq 1.8)}$$

here, e is the electron charge, μ is the mobility of the charge carriers and n is the number of charge carriers. From this equation, we know that to increase the conductivity, we can either increase the number of charge carriers (free electrons for n-type materials) or increase the carrier mobility. The charge carriers can be increased by introducing dopants or vacancies. The mobility of the charge carriers is influenced by intrinsic scattering. When number of charge carriers increased, the intrinsic scattering mechanism will limit the mobility and greatly influence the conductivity.

For a good transparency in visible light range, a large band gap (at least 3 eV) is necessary. For ITO, the valence band is formed by oxygen 2p orbital and the conduction band is formed by metal s band. Oxide materials usually have a relatively large band gap due to the low energy 2p bands. Without doping, pure indium oxide does not exhibit good conductivity. By doping Sn atoms in the lattice, a large number of extra electrons (donors) are introduced in the lattice and these donor states can alter the conduction band. With increasing donor density, the donor states can form a band which merges in the conduction band [16]. The critical density n_c for this kind of merging can be calculated by Mott's criterion:

$$n_c^{1/3} a_0^* \approx 0.26 \quad \textbf{(eq 1.9)}$$

the effective Bohr radius a_0^* can be calculated using:

$$a_0^* = \frac{h^2 \varepsilon_0 \varepsilon}{\pi e^2 m_c^*} \quad \textbf{(eq 1.10)}$$

For ITO, the static dielectric constant ε has a value of 8.9 [17], and the effective mass of electron in the In_2O_3 conduction band m_c^* has a relationship with electron restmass as [18] $m_c^* = 0.35 m_e$. The effective Bohr radius a_0^* of indium oxide lattice can be calculated to be about 1.3 nm. Critical density n_c is about 10^{18} cm^{-3}, but Sn doping in In_2O_3 can induce electron density up to 10^{21} cm^{-3}, which is a much larger charge carrier than the critical number. The extra electrons can be expected to freely transfer to the conduction band. The highest occupied level determines the Fermi energy and can be expressed as:

$$E_F = \frac{h^2 k^2}{8\pi^2 m_c^*} \quad \textbf{(eq 1.11)}$$

Figure 1.2 shows schematic illustration of the electronic band structure of an ITO material. In ITO materials, the bottom part of the conduction band has been occupied and those lower energy states have been blocked, which means the optical band gap has been enlarged by doping. Ideally, the bands show as parabolic shape. In reality, the band may be distorted by many-body interactions, like the electron-electron and electron-ion scattering, so the effective mass in this region can be very difficult to determine [19].

Other than increasing the number of charge carriers, another possibility for increasing the conductivity is through increasing the carrier mobility. The carrier mobility is greatly influenced by scattering mechanisms. For example, for small sized nanocrystals (diameter smaller than 50 nm for ITO), grain boundary scattering must be considered [20]. For highly doped ITO material (60 % Sn for example), neutral impurity scattering must be considered [18]. Also, the Sn dopants can intrinsically introduce ionized impurity scattering in the lattice. Among all scattering mechanisms, the ionized impurity scattering should be the main reason for limiting the mobility of the charge carriers [17,21].

The dopants in the lattice exist as ionized impurities. Among the ionized impurities and the free electrons there are Coulombic interactions. This Coulombic interaction sets a limitation for the conductivity. The ionized impurity scattering can be calculated by Born approximation [21], in which the ionized impurities assumes to form a uniform background of immobile charges, the

free electrons form as screening (Thomas-Fermi screening). After taking the non-parabolic band shape into consideration [22], they can calculate the effective mass at the Fermi-energy as follows:

$$m^* = m_0^* \sqrt{1 + 2C \frac{h^2 (3\pi^2 n)^{2/3}}{4\pi^2 m_0^2}} \qquad \textbf{(eq 1.12)}$$

This equation indicates that the effective mass will be larger due to scattering mechanism, which will lower the Fermi energy and shrink the band gap.

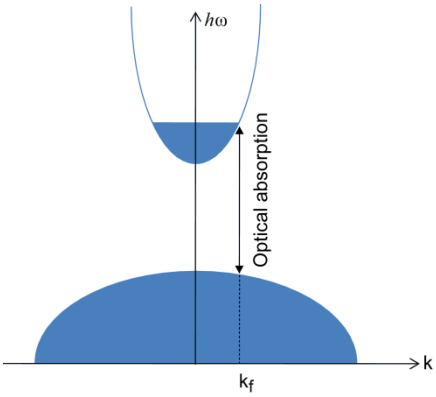

Figure 1.2 Schematic representation of the band structure of an ITO material. The blue part indicates the occupied parts of the band.

The optical property of an ITO material is directly related to its electrical properties. For example, the energy position of the plasmon band is directly proportional to the electron plasma frequency (ω_p), which has a square root dependence on the free electron concentration [23]:

$$\omega_p = \sqrt{\frac{Ne^2}{m^* \varepsilon_{opt}\, \varepsilon_0}} \qquad \textbf{(eq 1.13)}$$

Large number of free carriers (N) will induce a higher frequency, shorter plasma wavelength. By tuning the free charge carriers, the plasma wavelength of ITO material can be tuned (1500 nm to 4000 nm) [24].

There are two opposite mechanisms determining the apparent band gap of the ITO material: Burstein-Moss effect [25] and scattering effect. The Burstein-Moss effect is mainly due to the gradual occupation of the lowest level of the conduction band and blocking of the effective energy transfer from these low conduction levels, which cause widening of the band gap. In competition, the scattering mechanism will enlarge the effective mass, lower the Fermi energy

and narrow the band gap.

$$E_g = E_{g0} + E_{BM} - h\sum \quad \textbf{(eq 1.14)}$$

In this equation, E_{g0} indicates the intrinsic band gap, the E_{BM} stands for the contribution from the Burstein-Moss effect and the term $h\sum$ stands for the band gap narrowing from electron scattering.

1.2 Mechanism for DAP (Donor Acceptor Pair) Luminescence and Lanthanide Luminescence

There has been a significant interest in luminescence materials due to their various applications. Different kinds of luminescence materials usually have different emission mechanisms. For example, the Hg fluorescent lamps emit UV light due to electric transitions of Hg atoms [26]. $CaWO_4$ (used for X-ray detection) emits due to charge transfer from WO_4 group. Among all these mechanisms, the DAP mechanism is of special importance for semiconductors. Also, the energy transfer from some localized exciton to light emitting ions can also explain the lanthanide emission in semiconductor materials.

1.2.1 Mechanism for DAP (Donor Acceptor Pair) Luminescence-Using β-Ga_2O_3 as an Example

In semiconducting materials, there has been much effort to induce different kinds of dopants as donors and acceptors. These donors and acceptors can form different energy levels between conduction band and valence band. Initially, the donors and acceptors are all ionized (D^+ and A^-). When high energy light is absorbed by the lattice, electrons are excited from the valence band to the conduction band [27]. The electrons in the conduction band can be captured by ionized donors (D^+ to D^X), and the holes left in the valence band can also captured by the ionized acceptors (A^- to A^X), thus, through a tunneling process, electron can transfer from donor to acceptor sites [28]. At the acceptor sites, a trapped exciton is formed, and by radiative recombination, DAP luminescence is generated. Since the final states are still ionized states (ionized donors and ionized acceptors), there is Coulombic interactions between them [29]. The distance between the donor and acceptor influence the emission energy:

$$E = E_g - (E_D + E_A) + \frac{e^2}{4\pi\varepsilon r} \pm nE_{phonon} \quad \textbf{(eq 1.15)}$$

In this equation, E_g stands for the band gap energy of the lattice. E_D and E_A stands for the binding energy of donors and acceptors. The term $E_C = e^2/4\pi\varepsilon r$ stands for the Coulombic interaction between the ionized donor and acceptor. Since the larger the distance, the smaller the E_C values, the emission energy will be smaller for large distance DAPs. Since the donors and acceptors are all in the crystal lattice, the distance is not continuous but discrete due to the donor and acceptor positions. When interaction with excited state is small, no phonon is released, the emission can form a spectrum with sharp lines (**Figure 1.4**). When emission takes place between the completely relaxed excited state to ground state, the emission peak is termed the zero phonon line. Also, when the excited states are coupled with host lattice vibration and give longitudinal optical phonons, the emission will show relaxed, more smooth emission spectrum.

The width of the emission band is mainly given by the Coulombic term. And from the DAP model we can deduce a few interesting results. First, different wavelength of DAP band will show different time decay curve [27]. The higher energy part will have faster decay rate, which is caused by the fact that the higher energy emission indicates small distance DAP, which has large E_C value. Also, since the low energy part of the spectrum decays slower, it can be easily saturated by high power excitation. So, a peak shift to high energy is expected for high power excitation.

When we consider β-phase gallium oxide as an example, the donor is an oxygen vacancy (V_o^x), and the acceptor is a gallium-oxygen vacancy pair ((V_O, V_{Ga})^x), this will be the neutralized form of the donor and acceptor. In reality, the donor and acceptor are more stable when they are in ionized form. It is therefore more reasonable to consider the donor as $V_o^{\cdot\cdot}$ and acceptor as (V_O, V_{Ga})$'$ and these ionized donor acceptor can act as DAP:

$$(V_o, V_{Ga})^x + V_o^x \rightarrow (V_o, V_{Ga})' + V_o^{\cdot} + hv \quad \textbf{(eq 1.16)}$$

When electrons and holes are trapped by the ionized defects, the DAPs can undergo recombination. If the distance between donor and acceptor is r, the rate of recombination can be defined using the following equation:

$$W(R) = W_0 \left| \int_V \psi_D(\vec{r}) \psi_A(\vec{r} - \vec{R}) d\vec{r} \right|^2 \quad \textbf{(eq 1.17)}$$

In this equation, W_0 works as a constant, ψ_D and ψ_A stands for the envelope function for the donor and acceptor. In order to analyze the data, we need to give a few assumptions to simplify the equation. Both the donor and acceptor envelope function can be approximated by hydrogenic

function (ψ_D (R) ~ exp(-R/R_D), ψ_A (R) ~ exp(-R/R_A)). The Bohr radius can be obtained by hydrogenic energy equation: $R_D=e^2/2\varepsilon E_D$. So if we can know the donor binding energy E_D and the static dielectric constant ε, we can calculate the Bohr radius of the donor and acceptor, and taking the less tightly bonded carrier Bohr radius into the equation [30,31], we can get:

$$W(R) = W_0 e^{-2R/R_D} \quad \textbf{(eq 1.18)}$$

Also the maximum emission peak shifting with time can be given by [32,33]:

$$\ln(W_0 t) = \frac{4E_D}{E_C} + \ln(1 - \frac{E_C}{E_D}) \quad \textbf{(eq 1.19)}$$

From this equation, we know that E_C is smaller than E_D. If we take the largest and smallest Coulombic interaction as $E_{C,\infty}$ and $E_{C,0}$, we can get:

$$E_{C,\infty} - E_{C,0} = \Delta hv \quad \textbf{(eq 1.20)}$$

the shift of the maximum emission energy can be mainly due to the changing of Coulombic interaction. Also, if we took the far distance $E_{C,0}$ as 0, we will notice that the peak shift will be smaller than the donor binding energy.

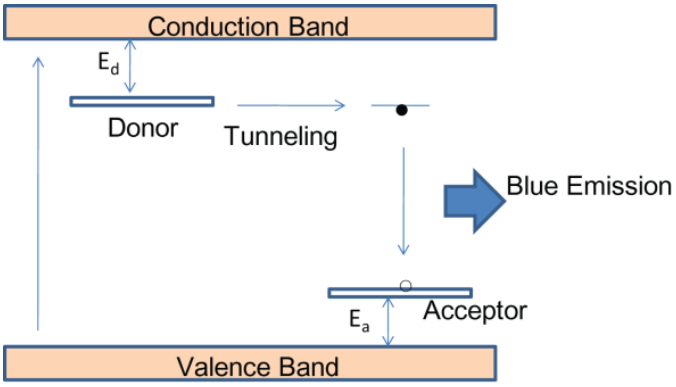

Figure 1.3 Scheme for blue luminescence in gallium oxide. After excitation, the excited electrons are trapped in donor level (oxygen vacancies) and holes trapped in acceptor level. Via tunneling process, the exciton can be formed at the acceptor site, and radiatively recombines, emitting a blue photon.

The current study of DAP emission of β-phase gallium oxide shows that, the electrons in donor band can be delocalized to show conductivity and also show broad blue emission with strong Stokes shift, which is a localized feature. The conductivity may be induced by the oxygen vacancy clusters, which can delocalize the electrons. The blue emission may include both the donors and acceptors (pairs). The tunneling effect for an electron transfer from donor to acceptor

site is the rate determining step. Upon tunneling event, radiative recombination of the exciton at the acceptor site will give rise to the broad blue emission [4,5,34].

1.2.2 Mechanism for Lanthanide Luminescence

1.2.2.1 Lanthanide Luminescence in Solids

The excitation of lanthanide luminescence can take place by either the host lattice or impurity dopants [35,36]. In most of the learned cases, the excitation occurs through dopant ions. These emission centers are called activator ions. When activator ions cannot absorb enough energy for excitation (low absorption cross section for lanthanides [37]), we can add sensitizers, which can absorb enough energy and transfer them to the activators. Lanthanide emission color can be tuned by changing the dopant without changing the crystal lattice. Lanthanide ions emit at particular positions, which are hardly influenced by chemical environments.

Other than the band to band transition induced luminescence and two center transition luminescence, lanthanide emissions are all one center luminescence. Other transition metal ions or molecular ions may also hold this kind of luminescence. In principle, the characteristic one center luminescence can be usually very sharp (emission width a few nm). But sometimes, broad band luminescence can also be observed. The emission band width is related to the character of the ground and excited state. The distance between the center ions and the surrounding environment can also play a key role. All these facts can be explained using the configuration coordinate diagram.

K_g and K_e means the metal ligand distance in ground states and excited states. E_g and E_e stands for the energy at which the maximum absorption and emission intensity occurs. The phonon energy in the relaxation process can be expressed as $S_g\hbar\omega_g$ and $S_e\hbar\omega_e$. S_g and S_e are the Huang-Rhys factors, which give us the number of phonons involved in the relaxation process. By using the configuration diagram, it's easier for us to understand the large Stokes shift and broad feature of certain center ion emissions [38].

Broad band emission can be observed in a lot of transition metals, like the Mn d-d transitions. For lanthanides, the d-f transition can also have quite broad band width. Other than that, the lone pair emission from Tl^+, Pb^{2+}, Sb^{3+} can all be broad center emission. Contrary to broad centered emission, sharp characteristic emissions can usually be caused by similar ground and excited state with stable chemical bonding character. The lanthanide f-f transition, which is hardly

participating in chemical bonding, is also quite sharp and circumstance independent.

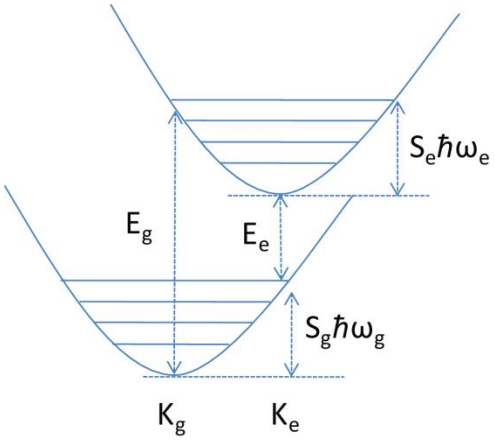

Figure 1.4 configuration coordinate diagram shows the band structure with ground state and excited state.

One example for the broad band emission is the optically allowed transition from 5d orbital to the 4f orbitals. The Eu^{2+} emission can usually be characterized in three different types [39]: the most common one is the normal d-f broad emission. This d-f transition occurs from the relaxed $4f^6 5d^1$ level, to the ground state $4f^7[^8S_{7/2}]$. This transition is both spin and dipole allowed, compared with parity forbidden f-f transition, they can have a relatively large efficiency. Another kind of d-f luminescence is characterized by narrow UV emission which is the $^6P_{7/2}$-$^8S_{7/2}$ emission after phonon relaxation of the $5d^1$ to the excited f state. This kind of f-f transition is often accompanied with broad band d-f emission at room temperature. Also, large Stokes shift and broad emission can also be attributed to the auto-ionization of the excited 5d orbital electrons. The electrons radiatively recombine with holes and transfer back to the ground state. Unlike the 4f electrons which are well shielded by the 5s and 5p orbitals, which are just insensitive to the surrounding environment, since the 5d electrons are unshielded, they are just interacting with the surrounding ions. When we consider the crystal field in the octahedral environment, the 5d orbitals will have a large crystal field splitting, and the splitting decreasing with increased size surrounding polyhedrons [40]. If we compare the crystal field splitting for Ce^{3+} and Eu^{2+}, Eu^{2+} is about 20 % smaller than Ce^{3+}.

Up to now, there have been few reports about the Eu^{2+} ions on a trivalent site, most of the Eu^{2+} dopants are on divalent or monovalent sites. Due to a large gap between the ground state and the excited $4f^6 5d$ state, the excited state is usually inside the conduction band of the crystal lattice,

followed by the auto-ionization, the photoluminescence will be quenched. One way to stabilize the Eu^{2+} ions is to induce charge compensation defect in the first anion coordination shell [41,42], like an ion vacancy. Also, the local ionic environment may be quite different for different kind of ions (Eu^{2+}, Eu^{3+}).

Before we go into the detailed energy transfer process for lanthanide ions in semiconductors, we will review the lanthanide emission theory briefly, which have been well defined a long time ago [43]. In nature, the absorption (emission) of light due to excitation or transfer electrons circling the nucleus is not random, it must obey certain parity rule (such as Laporte's rule, which defines the total angular momentum changes an odd number from initial to final state): When we just consider the pure 4f orbitals, the eigenstates of the even parity crystal field Hamiltonian usually define the magnetic dipole (MD) intensity, but when we consider the electric dipole (ED) intensity, we must consider mixed parity, which means consideration extends out 4f wavefunction and consider odd parity Hamiltonian. In systems with symmetric center, the odd parity vibration will mainly contribute to the fluctuation of crystal field potentials, which indicate a ED transfer mostly silent in centrosymmetric system. For example, with initial angular momentum J and final angular momentum states J', for $\Delta J=0,\pm1$ (excluding J=J'=0), the MD transitions are usually more intense than the ED vibronic transitions. These transition lines are MD allowed and ED forbidden. Oppositely, when $\Delta J=2$, 4, 6 these transitions are ED dominate and are the ED allowed transitions. In crystals without an inverse center, the contributions from vibrational modes will be less and the ED and MD transitions can both be observed in these systems. When the lanthanide ions can be inserted into a crystal lattice, the crystal field will split the J states into 2J+1 sub-states (Stark sub-states) [44]. Transition between all these sub-states also depends on the symmetry of the crystal lattice.

The symmetry defined transition rules are only valid in the ideal situation (no large distortion, no overlap of the 4f-5d wavefunctions). In reality, the so called forbidden transition is not totally forbidden. It just has a low transition probability compared to the allowed transition. According to the Judd-Ofelt theory, the ED transition intensity can be derived from the following equation:

$$D_{ED} = e^2 \sum_{\lambda=2,4,6} \Omega_\lambda \left|\langle \Psi \| U^\lambda \| \Psi' \rangle\right|^2 \qquad \textbf{(eq 1.21)}$$

Here, e stands for elementary charge (4.803×10^{-10} esu). The bracketed part is the dimensionless

matrix elements and is not influenced by chemical environment. Ω_λ stands for the influence of chemical surrounding on the lanthanide ions and can be experimentally determined.

Due to the fact that f-f transition is parity forbidden, the f-f absorption coefficient ε is quite low. Still, with high power direct f-f excitation (such as excited by a laser source), we can still get intense f-f emission. One important parameter for lanthanide emission is the intrinsic quantum yield, which is defined as:

$$Q_I = \frac{K_r}{K_r + K_{nr}} \quad \textbf{(eq 1.22)}$$

In this equation, the K_r and K_{nr} stands for the radiative and nonradiative rate constant. Contributions to the nonradiative constant mainly comes from lattice vibration, energy back transfer and surface dangling bonds vibrations [45]. Value of the intrinsic quantum yield is greatly influenced by the energy gap between the excited state and highest ground state. A small gap usually induces non-radiative recombination. As an empirical rule, when the energy gap is smaller than 6 high energy phonons, the multiphonon non-radiative de-excitation will dominate the process. The relationship between the intrinsic quantum yield and overall luminescence quantum yield can be expressed as:

$$Q_{all} = \eta_{sens} Q_I \quad \textbf{(eq 1.23)}$$

Usually, the overall quantum yield can be measured directly. The intrinsic quantum yield can be estimated if we know the radiative and non-radiative decay rate. Thus, we can calculate the sensitization of efficiency η_{sens}.

To know the radiative decay rate, we need to get the radiative decay probability, which can be determined by the following equation:

$$A(\Psi_J, \Psi'_{J'}) = \frac{64\pi^4 \tilde{\upsilon}^3}{3h(2J+1)} \left[\frac{n(n^2+2)^2}{9} D_{ED} + n^3 D_{MD} \right] \quad \textbf{(eq 1.24)}$$

In this equation, Ψ_J and $\Psi'_{J'}$ indicate the initial and final state of the transition. $\tilde{\upsilon}$ is the transition energy. h is Plank's constant and n as refractive index. D_{MD} and D_{ED} are the magnetic dipole and electric dipole intensity, respectively. Definition of D_{ED} has been given in **eq 1.21** and the D_{MD} definition is given below:

$$D_{MD} = \left(\frac{eh}{4\pi m_e c}\right)^2 |\langle \Psi || L + 2S || \Psi' \rangle|^2 \quad \textbf{(eq 1.25)}$$

Since the bracketed part can be known thus from all equations above we can calculate the radiative decay rate. However, this calculation may not give accurate results. In another situation,

when we already know the emission related absorption spectrum, we can use the following equation:

$$K_r = 2303 \times \frac{8\pi c n^2 \tilde{\upsilon}^2 (2J+1)}{N_A (2J'+1)} \int \varepsilon(\tilde{\upsilon}) d\tilde{\upsilon} \qquad \textbf{(eq 1.26)}$$

For Eu ions, the equation can be simplified as:

$$K_r = A_{MD}\, n^3 (\frac{I_{all}}{I_{MD}}) \qquad \textbf{(eq 1.27)}$$

A_{MD} is equal to $15s^{-1}$, the intensity ratio in the bracket stands for the integrated Eu emission over integrated $^5D_0$-$^7F_1$ emission. The decay rate is not a constant and it will be influenced by the emitting state and the crystal lattice.

1.2.2.2 Lanthanide Luminescence in Semiconductors

Lanthanide ion doped semiconductors have been studied for a long time for their fascinating electrical and optical properties. Due to shielded 4f electrons that are seldom influenced by surrounding environments, the emission energy is strongly localized. Up until now, many studies have focused on the ZnS:Tb, Eu materials as long life light emitters [46]. The Er doped Si or SiO_2 [47] are used for optical communication or as amplifiers [48]. The so called resonant or direct excitation is defined as the excitation of the lanthanide ions with the same energy as higher level 4f states. The non-resonant or indirect excitation means that the excitation of the host lattice first, then transfer of the energy to the lanthanide ions.

The excitation of lanthanide ions doped in semiconductors may be due to resonant excitation or non-resonant processes. One mechanism called impact excitation occurs when hot electrons are scattered by lanthanide ions and transfer their energy to the 4f electrons. Another indirect mechanism may involve electrons and holes in the lattice. The host lattice may first be excited, and then the energy of the non-radiative recombination of electrons and holes can transfer to the lanthanide ions. The excited electron and a nearby hole can form either a free exciton or a bound exciton. The bound exciton may be induced by incorporation of large lanthanide ions inside the lattice (lattice distortion). Alternatively, the bound exciton may be induced by local defects and impurities. The impurities or defects should be close to the lanthanide ions for efficient energy transfer. Also, it is possible for the excited electron to be captured by the lanthanide valence band, and subsequently a hole is also captured. Then, the impurity related donor acceptor pair may induce the recombination and transfer the energy to the lanthanide ions [49].

After electrons are excited from valence band to conduction band, remaining free carriers can form free excitons. These free excitons can interact with the lanthanide ions and transfer the energy non-radiatively to the lanthanide ions. One correlation of this kind of energy transfer will be the decrease of free exciton emission intensity while lanthanide emission intensity increases. One of the most important excitation mechanisms is the energy transfer from the bound excitons (BEs) to the lanthanide ions. BEs can be trapped by impurities, local or external defects. An electron from the conduction band or a hole from the valence band can be captured by a trap in the band gap. The BE can be formed by attracting a free hole or electron from defect levels. Electrically active local defects may act such as traps to form BEs [50].

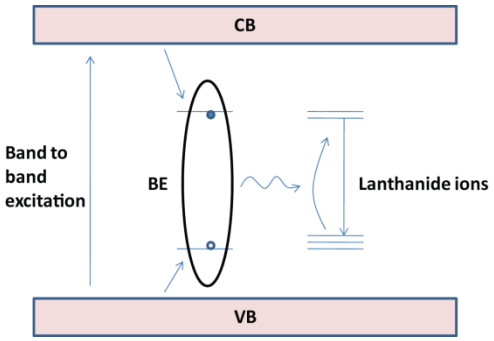

Figure 1.5 Lanthanide ion excitation through band to band transition.

Figure 1.5 demonstrates several different steps in the lanthanide excitation through band to band transition. After electron excitation from the valence band to the conduction band, the electrons can be captured, forming a trapping site; followed by binding with a hole from the valence band, the BEs can form in this way and non-radiative transfer of the energy to the lanthanide ions occurs.

Excitation of lanthanide ions may also involve donor acceptor pairs (DAPs), and is observed in lanthanide doped Ⅱ-Ⅵ semiconductors. For all lanthanide ions with a 3+ charge, the ground level may be within the valence band. Due to the tendency for charge compensation, the lanthanide ions may be associated with acceptors to form DAPs. When excited, an electron can transfer from the acceptor to the lanthanide ion, which acts as a donor. Then, following a non-radiative recombination, the DAP transfers its energy to the lanthanide ion. The energy transfer rate is strongly dependent on the spatial distance of the DAP and the lanthanide ions. It also depends on the overlap of the donor emission and the acceptor absorption if the transfer is

resonant. Another situation is that, if the lanthanide ion is not a direct component of DAP, and instead, is quite close to the DAP, the transfer efficiency can be high only when one of the components in the DAP is close to the lanthanide ion [51].

Our excitation mechanisms for the lanthanide ions in semiconductors all involve non-radiative energy transfer from localized excitons (or DAPs) to lanthanide ions. One mechanism available to explain this phenomena is the Forster Resonant Energy Transfer (FRET), which relies on the dipole-dipole interaction and is well-known for all kinds of materials [52]. Another explanation is Dexter-type energy transfer, which involves higher order, shorter distance interactions [53].

Now we consider the energy transfer process with one energy donor and one energy acceptor. The donor will transfer from its excited state to its ground state, $D^* \rightarrow D$, and the acceptor will undergo a transition from its ground state to its excited state $A \rightarrow A^*$. Both transitions have normalized wavefunctions $g_D(E)$ and $g_A(E)$ respectively. With one operator, H', the donor acceptor state vector transfer from $|D^*,A\rangle$ to $|D,A^*\rangle$. The overlap between the donor emission and acceptor absorption is directly related to the energy transfer efficiency.

$$W_{DA} = \frac{2\pi}{\hbar}|\langle D, A^*|H'|D^*, A\rangle|^2 \int g_D(E) g_A(E) dE \qquad \textbf{(eq 1.28)}$$

The energy transfer system is non-radiative and no photon emission or absorption is observed. The main driving force for this transfer is the coupling effect (dipole-dipole, dipole-quadrupole, quadrupole-quadrupole). Also, the energy transfer may be non-resonant in the case where there is an energy mismatch between the donor emission and acceptor absorption. Such energy transfer requires vibration induced electron-phonon coupling to be taken into consideration. Dexter proposed an equation with vibronic components:

$$W_{DA} = \frac{2\pi}{\hbar}|\langle D, A^*|H'|D^*, A\rangle|^2 S_{DA} \qquad \textbf{(eq 1.29)}$$

When we consider the energy transfer in the lattice, random dopant distribution is usually assumed. This kind of approximation may not be valid in some cases. For example, when samples are synthesized at high temperature or excited with high energy, the defect migration may need to be considered.

With a lost anion, an anion vacancy forms, and the anion vacancy states formed below the conduction band bottom are mainly due to the empty cation orbitals pointing to the anion vacancy. In a similar way, the cation vacancy is formed by the surrounding anion lone-pair orbitals. When

the strength of the bonds in the lattice is stronger, the delocalization energy will be higher, and defect states are deeper in the band gap. The point defects in solids have a tendency to be expelled out towards the surface for better stabilization of the crystal. Electrostatically, the positively and negatively charged defects may migrate closer to one another. Even without electrostatic interaction, if we consider the difference between dopant and lattice cations, such as the ionic radius, electronegativities, and ionization potentials, the defects may still show a nonrandom distribution. For example, the dopant with lower ionic potential will have a higher tendency to attract an anion vacancy. Thus, anion vacancies inside the lattice may not be randomly distributed and may be around the dopant cations. This kind of vacancy stabilization may also influence the defect level in the band gap. When dopants with lower ionization potentials are doped in the lattice, the anion vacancies have a tendency to agglomerate around them, thus losing their role as effective traps [54].

1.3 Conclusion

In this chapter, we have provided an overview of the mechanism for electrical and optical properties in transparent conducting oxides. The characteristic reflection for ITO is induced by electrons in the conduction band, and the scattering mechanism which limits the conductivity is also discussed. In wide band gap semiconductors, defect induced DAP emission is quite common and potentially important in optical devices. We discussed several common features of DAP emission, such as the wide broad emission band, large Stokes shift, and emission energy related decay curves. Finally, we discussed the possible mechanism for lanthanide doped semiconductors. The lanthanide dopant can be sensitized by the host lattice through nonradiative energy transfer. Energy transfer from DAP to lanthanide ions, which is important in our study, has also been discussed.

1.4 Research Motivation and Thesis Scope

Transparent conducting oxides have fantastic electrical conductivity and optical transparency and are widely used in optical and electrical devices. Due to various applications of transparent conducting oxides, the study of nanostructured TCOs can be important practically. TCOs in nanoscale can induce size dependent new properties and the multifuctional nanostructured TCOs

can be used as functional units in next generation optical and electrical devices.

Up to now, various rules have been established for explanation of the properties, like the transmittance, luminescence in bulk TCOs. But not a lot of theoretical work has been done on nanostructured TCOs. Most of the current research on these nanostructured TCOs are like stamp collecting, people only observe interesting phenomena and pretty structures, but don't have deep understanding on the theories and rules behind these fancy pictures. First of all, my research on nanostructured TCO can produce new kinds of materials with combining traditional and new size related properties, which have potential applications. Also, the uniform colloidal NCs in my research provide an ideal platform for verifying important rules in nanoscale. All these research can further our understanding towards nanoworld and have practical and theoretical importance.

In this thesis, I choose two typical wide band gap TCOs, ITO and Ga_2O_3, to study their nanostructure related optical properties. By a simple solution method, I successfully synthesized uniform colloidal NCs for ITO and Ga_2O_3. In the following chapters, I describe the common features of these NCs (size, composition, uniformity) and also conduct extensive investigation on optical properties of these NCs using various techniques. The mechanisms related to their unique optical properties are also proposed.

ITO is one of the most commonly used TCOs due to its high conductivity and transparency. In our recent studies we showed that metastable *rh*-In_2O_3 can be stabilized by controlling the size and growth kinetics of In_2O_3 NCs, which gives us a chance to incorporate Sn^{4+} into two different NC phases of indium oxide lattice. In **chapter 2**, I report the synthesis and optical and electronic properties of colloidal *rh*- and *bcc*-ITO NCs. The influence of Sn^{4+} doping on phase stabilization has been examined and the electrical conductivity and optical transparency of these two phases have been described.

From **chapter 3**, the research will mainly focus on γ-phase Ga_2O_3. Previous investigations of Ga_2O_3 have mainly focused on monoclinic β-phase due to its thermal stability. Due to difficulties in controlled synthesis and isolation, γ-phase Ga_2O_3 has been much less studied and understood. In **chapter 3**, I report colloidal synthesis of gallium oxide NCs with γ-phase crystal structure and uniform size distribution. As synthesized NCs exhibit size tunable photoluminescence from purple to blue. In **chapter 4**, I implement steady-state and time-resolved luminescence and address the role for NC size, structure, defects and surface capping on the PL energy, efficiency and dynamics.

In previous study, TCO NCs were proven to be effective host materials for sensitization of lanthanide emission. In **chapter 5**, I describe my research on lanthanide-doped γ-phase Ga_2O_3 NCs and collected the steady state and time resolved emission spectra. I demonstrate the tuning of sample chromaticity by tuning delay time or gate time, indicate their potential applications in biosensing and time sensitive devices. In **chapter 6**, the final conclusions summarize all the work been done in this thesis.

Chapter 2 Free Electron Concentration in Colloidal Indium Tin Oxide Nanocrystals Determined by Their Size and Structure

2.1 Introduction

The possibility of imparting specific optical, electrical, or magnetic properties into semiconductor nanocrystals (NCs) rests largely upon the ability to dope these materials with selected impurity ions. *In-situ* doping of colloidal NCs from solution has, therefore, become a very active area of research in recent years [1,2]. Initial work has largely focused on doping Mn^{2+} ions into II-VI NCs [3-9]. These efforts have often yielded contradictory results, and different mechanisms of doping NCs from solution have been proposed. A theoretical study has suggested that binding energies for manganese atoms (Mn^0) on various semiconductor surfaces can be used to predict the possibility of doping Mn^{2+} into particular NCs [10]. This study has predicted that manganese dopants are more easily incorporated into NCs having the zinc-blende structure compared to those having the wurtzite structure, which has been signified as the main reason for the early difficulties [7] in doping CdSe NCs. Subsequent experimental results [11,12] have shown, however, that high Mn^{2+} doping concentrations can be successfully achieved in wurtzite NCs, suggesting that a more comprehensive picture is needed to describe the incorporation of dopant ions from the solution phase. It has been proposed that hard-soft acid-base surface chemistry [13] and the nature of the dopant ion with respect to the structure of the NC host lattice [12,14] also play important roles. The developments of different synthetic approaches and the improved understanding of the doping mechanism have led to a successful doping of a range of colloidal NCs with various dopant ions [14-18].

Transparent conducting oxides (TCOs) have considerable technological importance because of their transparency, conductivity, and a variety of possible crystal structures. These properties call for an optimization and expansion of the existing functionalities of TCO-NCs [19-23]. Tailoring electrical properties of TCO-NCs by doping has been one of the focal points of such research efforts [24-28]. The most widely studied and used TCO is indium tin oxide (ITO) [29]. In spite of a range of applications of ITO in flat-panel displays, energy-efficient windows, solar cells, and gas sensors, the synthesis of colloidal ITO NCs with controlled sizes, shapes, and crystal structures remains a challenge. This is partly due to the lack of understanding of the influence of tin dopants on the growth, structure, and properties of ITO NCs. Several methods have been

reported for the synthesis of ITO NCs, including colloidal [24,27,30], microwave [26], and

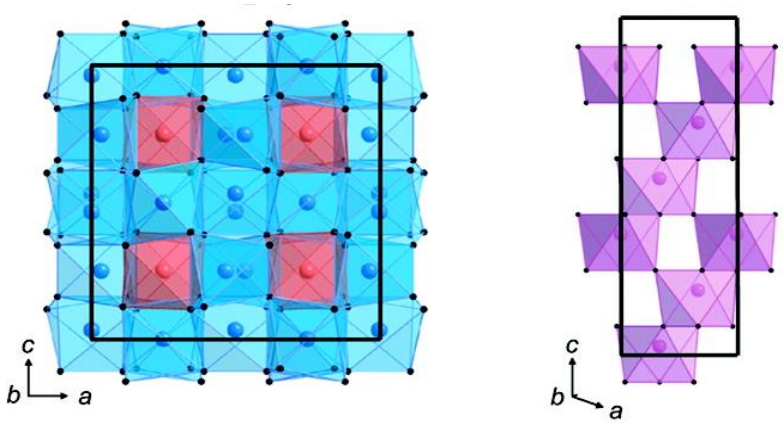

Figure 2.1 Crystal unit cell of cubic bixbyite-type In_2O_3 (*bcc*-In_2O_3, left), and corundum-type In_2O_3 (*rh*-In_2O_3, right) viewed along the b-axes. The angle between a- and b- axes for *rh*-In_2O_3 is 120 º. Reprinted with permission from ref [14]. Copyright 2009 American Chemical Society.

solvothermal [28] synthesis. In many cases relatively broad size distributions have been obtained [24, 26, 28]. While the syntheses of In_2O_3 NCs have largely been optimized [31-35], the origin of size distribution of ITO NCs is still poorly understood. Indium oxide exists in two possible phases: cubic bixbyite with body-centered cubic crystal structure (*bcc*-In_2O_3, stable phase) and corundum with rhombohedral structure (*rh*-In_2O_3, metastable phase, graph of both phases can be seen in **Figure 2.1** [14]). In^{3+} cations exhibit two characteristic sites, known as b- and d-sites, in *bcc*-In_2O_3. One-fourth of In^{3+} are in b-sites and have D_{3d} point group symmetry (trigonally compressed octahedral coordination). Three-fourths of In^{3+} cations reside in highly distorted octahedral d-sites. Metastable *rh*-In_2O_3 [36] consists of hexagonal close packed oxygen ions, with In^{3+} filling up two-thirds of the six-coordinate C_{3v} sites. A majority of the literature reports the studies of ITO NCs with cubic bixbyite structure (*bcc*-ITO NCs) [24,26-28,30]. Doping corundum In_2O_3 NCs and a direct comparison between *rh*-ITO and *bcc*-ITO NCs are essential for understanding the influence of dopants on the growth and the optical and electrical properties of ITO NCs. Such a comparison could lead to the rational preparation of ITO NCs with the desired size, structure, and composition and to better understanding of the structure-function relationship in TCOs.

In our recent studies we showed that metastable *rh*-In_2O_3 can be stabilized by controlling the size and growth kinetics of In_2O_3 NCs [32]. Furthermore, the presence of dopant impurities in

solution leads to inhibition of NC growth by dopant binding to NC surfaces [14]. Together, these effects could allow for *in-situ* inhibition of In_2O_3 NC growth using Sn^{4+} ions and simultaneous studies of their incorporation into different NC phases. In this chapter I report the synthesis and optical and electronic properties of colloidal *rh*- and *bcc*-ITO NCs based on this dopant effect. An increased starting concentration of Sn^{4+} inhibits NC growth and allows for size-based stabilization of *rh*-ITO. Size selective precipitation enables the isolation of the dimorphs under identical synthesis conditions. Although Sn^{4+} incorporation is similar in both NC lattices, the free electron density is much higher in *bcc*-ITO than in *rh*-ITO NCs, indicating that electrical properties strongly depend on the size and structural changes of the host lattice. The presence of a free electron gas in *bcc*-ITO NCs leads to the formation of the localized plasmon oscillations, which can be described by the Drude-Lorentz model.

2.2 Experimental Section

2.2.1 Materials

All reagents and solvents are commercially available and were used as received. Indium(III) acetylacetonate ($In(acac)_3$, 98 %) and tin(IV) chloride pentahydrate ($SnCl_4 \cdot 5H_2O$, 98 %) were purchased from Strem Chemicals. Oleylamine (70 %) and tri-*n*-octylphosphine oxide (TOPO, 90 %) were purchased from Sigma-Aldrich.

2.2.2 Synthesis of In_2O_3 and ITO NCs

All syntheses were carried in the inert atmosphere. In a 100 mL three-neck round-bottom flask 0.9 g of $In(acac)_3$, 7.2 g of oleylamine, and varying amounts of $SnCl_4 \cdot 5H_2O$ were mixed under the flow of argon. The mixture was degassed and heated to 250 ℃, and the reaction was allowed to proceed for 1 h under constant stirring in argon. The reaction mixture was subsequently cooled to room temperature. Two fractions of NCs were obtained by the size selective precipitation [37]. Large NCs were first precipitated by centrifugation at 3000 rpm for 10 min. Small NCs were then precipitated from the supernatant by adding 20 mL of ethanol and centrifuging for 15 min. The precipitates of large NCs were blue, while those of small NCs were white. All NC precipitates were heated in melted TOPO, followed by precipitation with ethanol. This procedure was repeated three times to ensure the removal of surface-bound dopant ions [14]. The obtained nanocrystals were easily dispersed in hexane or toluene.

For time evolution studies, the reaction mixture was prepared in the identical way with the initial precursor concentrations corresponding to [Sn]/[In] = 0.15. The aliquots were taken at different times upon reaching the final reaction temperature of 250 ℃ (5, 10, 20, 30, and 60 min). The nanocrystals were precipitated with ethanol and redispersed in hexane after centrifuging and washing with ethanol. Synthesis of In_2O_3 NCs using $InCl_3$ precursor was performed in the same way and with the same concentration of In^{3+} ions.

2.2.3 Characterization and Measurements

Nanocrystals were characterized by X-ray diffraction using a powder diffractometer (INEL) with a position-sensitive detector and monochromatic Cu $K_{\alpha 1}$ radiation (λ = 1.5406 Å). Raman spectra were recorded using a Renishaw 1000 Raman spectrometer with a cooled CCD detector (New Mills, UK). The samples were excited with Melles Griot 33 mW helium-neon laser at 632.8 nm. XPS spectra were collected with VG Scientific CLAM-2 spectrometer, consisting of a hemispherical analyzer of a 100 mm mean radius and a triple-channeltron detector, using Al $K_{\alpha 1}$ radiation (1486.6 eV photon energy) as the excitation source. After digesting the NCs using nitric acid for 24 h, the solutions of the sample were also sent to University of Guelph for elemental analysis using inductively coupled plasma atomic emission spectrometry (ICP-AES). Indium L_3-edge XANES measurements were performed at the soft X-ray microcharacterization beamline (SXRMB) 06B1-1 (energy range: 2.1-10 keV; resolution $\Delta E/E$: 1×10^{-4} using Si (111) crystal) at the Canadian Light Source (CLS). XANES data were simultaneously recorded in total fluorescence yield and total electron yield modes. Transmission electron microscopy (TEM) images were collected with a JEOL-2010F microscope operating at 200 kV. The absorption spectra were collected with a Varian Cary 5000 UV-vis-NIR spectrophotometer.

2.3 Results and Discussion

2.3.1 Crystal Structure and Phase Selectivity of ITO NCs

X-ray diffraction (XRD) patterns of larger ITO NCs isolated from the samples prepared with different starting concentrations of Sn^{4+} are shown in **Figure 2.2a**. All XRD patterns match very well the pattern of bulk *bcc*-In_2O_3. In contrast, the XRD patterns of small NCs isolated from the same reactions by the size-selective precipitation correspond to *rh*-In_2O_3 (**Figure 2.2b**). At the starting concentrations of precursors corresponding to [Sn]/[In] $\leq$ 0.05 only larger NCs can be

isolated, while at high starting concentrations of Sn^{4+} ([Sn]/[In] ≈ 0.4), only small NCs are formed. The broadening of XRD peaks in **Figure 2.2b** is much more pronounced than the peak broadening in **Figure 2.2a**, consistent with a smaller size of *rh*-ITO NCs. XRD data clearly indicate that bimodal particle size distribution is formed in the presence of Sn^{4+} precursor and that the two fractions of NCs have different crystal structures. We have previously shown that metastable *rh*-In_2O_3 can be spontaneously stabilized in colloidal NCs below critical size, owing to the surface energy and/or surface stress contributions [32]. We have further demonstrated that the presence of transition-metal dopants inhibits the NC growth causing the stabilization of *rh*-In_2O_3 if the dopant precursor concentration is sufficiently high to inhibit the NC growth to below ca. 5 nm in size [14].

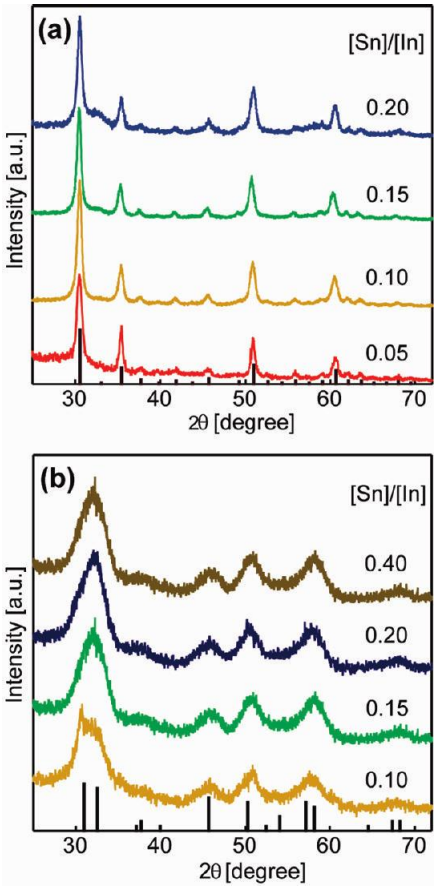

Figure 2.2 XRD patterns of large (a) and small (b) ITO NCs obtained by size selective precipitation of as-synthesized samples prepared with different starting Sn^{4+} concentrations. The starting concentration ratios of Sn to In are indicated in the graphs. Black lines represent the XRD pattern of bulk cubic bixbyite In_2O_3 (JCPDS 06-0416) in (a) and corundum In_2O_3 (JCPDS

21-0406) in (b).

The results in **Figure 2.2** indicate that impurity-induced inhibition of NC growth and the concomitant stabilization of *rh*-In_2O_3 phase is a general phenomenon applicable not only to first-row transition-metal ions as magnetic dopants but also to other ionic impurities. The incorporation of Sn^{4+} ions into *bcc*- and *rh*-In_2O_3 NCs can be achieved by the same synthetic method under identical conditions, while the size-structure correlation allows for selective isolation of a particular phase.

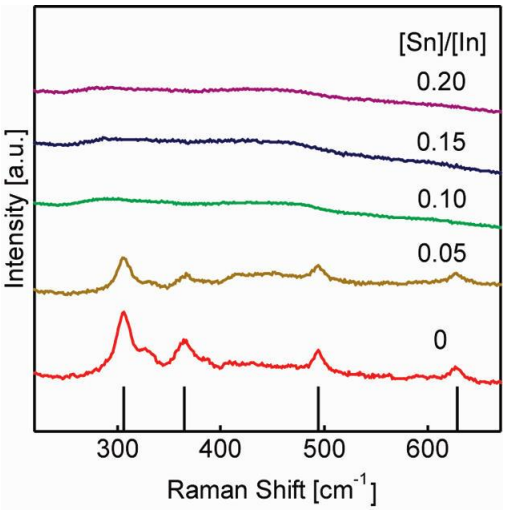

Figure 2.3 Raman spectra of *bcc*-ITO NCs isolated from the samples synthesized with different starting concentrations of Sn^{4+}. Numbers indicated in the graph are the starting concentration ratios of Sn^{4+} and In^{3+} precursors ([Sn]/[In]). Red trace is a spectrum of undoped *bcc*- In_2O_3 NCs; black lines represent the Raman peaks of bulk cubic bixbyite In_2O_3.

Raman spectra of larger ITO NCs isolated by the size selective precipitation for different starting concentrations of Sn^{4+} are shown in **Figure 2.3**. The peaks observed for undoped In_2O_3 NCs (red trace) are in very good agreement with the peaks reported for *bcc*-In_2O_3 (black lines) [38]. The intensity of the Raman peaks rapidly drops with increasing concentration of Sn^{4+}. At low starting Sn^{4+} concentrations ([Sn]/[In] ≈ 0.05, brown trace) all peaks characteristic for *bcc*-In_2O_3 are observed although they are significantly less pronounced than those in pure In_2O_3 NCs. The Raman spectra completely vanish with further increase in Sn^{4+} concentration. Although larger NCs retain cubic bixbyite crystal structure for all doping concentrations, as evidenced from the XRD patterns, the broadening and eventual disappearance of Raman peaks indicate that

interstitial or substitutional doping of Sn^{4+} ions into *bcc*-In_2O_3 NCs causes a decrease in phonon correlation lengths due to local crystal lattice disorder. This phenomenon has been reported for doped *bcc*-In_2O_3 using different structural techniques [39,40]. Similar results were obtained for *rh*-In_2O_3 NCs (**Figure 2.4**), for which the Raman spectra vanish at even lower Sn^{4+} concentrations, due to small NC sizes.

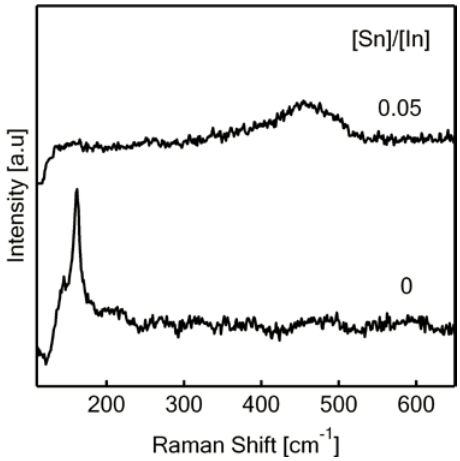

Figure 2.4 Raman spectra of *rh*-In_2O_3 ([Sn]/[In]=0) and *rh*-ITO NCs ([Sn]/[In]=0.05). The spectrum of un-doped In_2O_3 NCs shows a peak at 162 cm^{-1} characteristic for corundum-type In_2O_3 [16], which disappears for *rh*-ITO NCs. The Raman spectra of *rh*-ITO NCs prepared with higher Sn^{4+} precursor concentrations are the same as the spectrum shown in the graph indicating a local crystal lattice disorder due to the presence of Sn^{4+} dopants.

2.3.2 Composition and Electronic Structure of ITO NCs.

To determine the composition of ITO NCs for different starting concentrations of Sn^{4+} and to understand the speciation of tin dopants and their effect on the structure and properties of ITO NCs, we performed X-ray photoelectron spectroscopy (XPS) and X-ray absorption near-edge structure (XANES) study of *bcc*- and *rh*-ITO NCs. Representative XPS spectra for ITO NCs synthesized with [Sn]/[In] = 0.15 are shown in **Figure 2.5**. **Figure 2.5a** shows a typical survey spectrum of ITO NCs. The presence of indium, tin, and oxygen are clearly observed. Other samples show similar results with different relative intensities of Sn 3d peaks. The concentrations of tin in ITO NCs obtained with different starting concentrations of $SnCl_4 \cdot 5H_2O$ were determined from the relative integrated intensities of In and Sn XPS peaks (**Table 2.1**). The

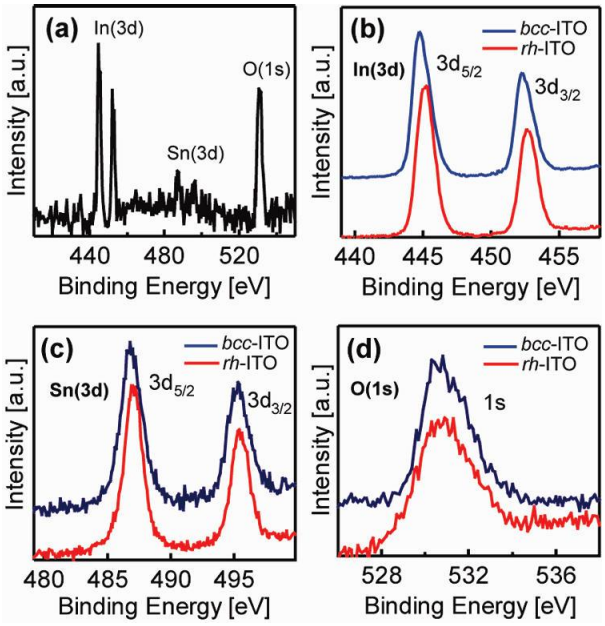

Figure 2.5 (a) XPS survey spectrum of typical ITO NCs. (b-d) XPS spectra of *bcc*-ITO (blue line) and *rh*-ITO NCs (red line) synthesized with [Sn]/[In] = 0.15 in different spectral regions: (b) In 3d, (c) Sn 3d, and (d) O 1s.

Table 2.1 Doping Concentrations of Sn^{4+} Ions in Colloidal ITO NCs Determined from XPS Spectra.

starting Sn^{4+} concentration ([Sn]/[In])	Sn^{4+} doping concentration in ITO NCs (at. %)	
	bcc-ITO	*rh*-ITO
0	0	
0.05	4.5	
0.10	8.6	9.0
0.15	12.3	13.8
0.20	18.5	17.4
0.40		32.7

doping concentrations increase with increasing amounts of $SnCl_4 \cdot 5H_2O$. At intermediate starting concentrations of Sn^{4+} ([Sn]/[In] = 0.10-0.30), for which both cubic bixbyite and corundum phases can be obtained from the same batches, similar doping concentrations were found in both phases (although on average somewhat higher in *rh*-ITO NCs), indicating a similar propensity for tin incorporation during colloidal synthesis of In_2O_3 NCs. This result is consistent with the previous findings that Sn^{4+} has strong preference for the b-site in *bcc*-In_2O_3 [41], which is similar to In^{3+} site in *rh*-In_2O_3. Inductively coupled plasma atomic emission spectrometry (ICP-AES)

analysis showed the same trend, although the measured tin concentrations were systematically lower, most likely due to difficulties with fully digesting ITO NCs for analysis. Indium 3d XPS peaks for *bcc*- and *rh*-ITO NCs are shown in **Figure 2.5b**. For *bcc*-ITO NCs the peak maximum of In $3d_{5/2}$ peak is centered at 444.7 eV, which is in a very good agreement with the results previously reported for bulk ITO with cubic bixbyite structure [42]. Indium 3d peaks for *rh*-ITO NCs are shifted to higher energies (445.2 eV for In $3d_{5/2}$), but the peaks for *bcc*-ITO NCs appear somewhat broader and more asymmetric, possibly due to the presence of In^{3+} in two different sites (b and d). On the other hand, Sn 3d spectra shown in **Figure 2.5c** are nearly identical for *bcc*- and *rh*-ITO NC (Sn $3d_{5/2}$ peak maxima are at ca. 487 eV), suggesting very similar speciation of tin ions in both NC lattices. Similar spectra have been reported for Sn^{4+} in bulk ITO and SnO_2 [42,43]. In contrast, the energies of $3d_{5/2}$ peaks for Sn^{2+} or metallic Sn^0 have been found to be centered at 485.6 and 484.9 eV, respectively [42]. The results of this work, therefore, strongly suggest the presence of Sn^{4+} substitutionally doped in In_2O_3 for both NC phases. Furthermore, the similarity of Sn 3d XPS spectra for *bcc*- and *rh*-ITO NCs corroborate that Sn^{4+} ions are predominantly doped into b-sites in *bcc*-ITO NCs. The same oxidation state of tin is consistent with the fact that both NC structures are obtained from the same reaction in which Sn^{4+} is not reduced to Sn^{2+} or Sn^0 during incorporation into NCs. **Figure 2.5d** shows XPS spectra of *bcc*- and *rh*-ITO NCs in the O 1s peak range. Relatively broad asymmetric peaks are recorded with maxima at ca. 530.7 eV and shoulders on the high energy side centered at ca. 532.5 eV. The main peak at 530.7 eV is assigned to oxygen sites in In_2O_3 NCs. The feature on the high energy side is most reasonably attributed to the O-H group or other forms of oxygen on NC surfaces [42,44]. We note that hydroxides are important intermediates in In_2O_3 NC formation [32]. This feature is

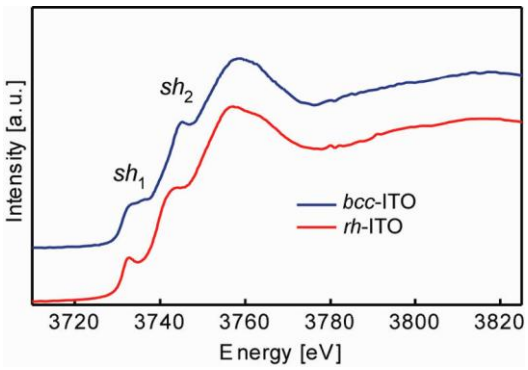

Figure 2.6 Indium L_3-edge XANES spectra of *bcc*-ITO (blue line) and *rh*-ITO NCs (red line).

usually more pronounced in small *rh*-ITO NCs owing to larger surface areas.

The change in the band structure of In_2O_3 due to a change in In^{3+} coordination can be effectively probed by XANES [45], making it an excellent complementary tool to XPS. Representative In L_3-edge X-ray absorption spectra of *bcc*- and *rh*-ITO NCs are shown in **Figure 2.6**. A comparison of the two spectra reveals distinctly different features. The shoulder at ca. 3735 eV (sh_1) is broader and more structured in *bcc*-ITO than in *rh*-ITO NC spectrum. On the other hand, a shoulder centered at ca. 3745 eV (sh_2) in the *bcc*-ITO NC spectrum is sharper and shifted to higher energies with respect to that in the *rh*-ITO spectrum. These differences indicate a different electronic band structure associated with In^{3+} in *bcc*- and *rh*-In_2O_3 NCs [45]. While the coordination number of In^{3+} sites is the same in *bcc*- and *rh*-ITO, the electronic band structure and the distribution of the density of states are not [46]. Importantly, these XANES measurements suggest that the electronic structure of Sn^{4+} substitutionally incorporated for In^{3+} in different ITO NC phases is also different.

2.3.3 Relationship between Size, Structure, and Self-Assembly of ITO NCs

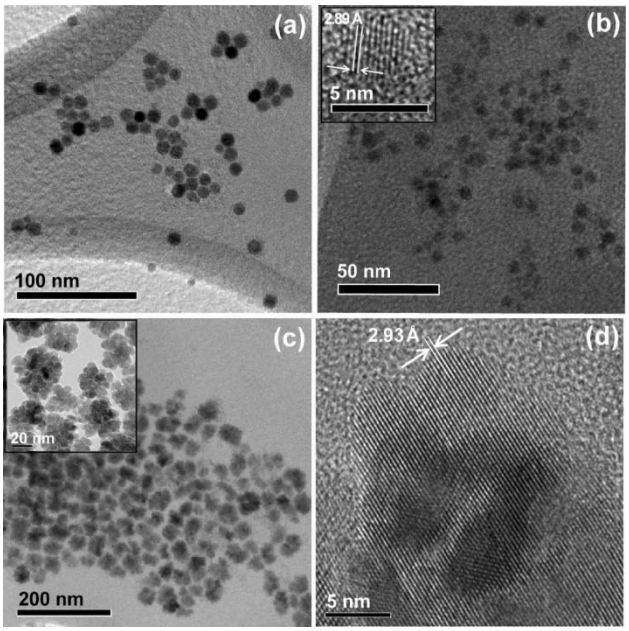

Figure 2.7 (a) TEM image of undoped In_2O_3 NCs. (b) TEM image of *rh*-ITO NCs obtained by size selective precipitation under the identical synthesis conditions as NCs in (a) with [Sn]/[In] = 0.15. Inset: lattice resolved TEM image of a single NC; the measured *d*-spacing of 2.89 Å correspond to {104} lattice plane of *rh*-In_2O_3. (c) Overview TEM image of *bcc*-ITO NCs

obtained in the same reaction as NCs in (b). Inset shows magnified flowerlike clusters resulting from the assembly of NCs. (d) Lattice-resolved TEM image of a typical nanoflower. Extended lattice fringes indicate the oriented attachment, and the measured lattice spacings of 2.93 Å match {222} *d*-spacing of *bcc*- In_2O_3. The average NC sizes are: (a) ~9 nm, (b) ~4.5 nm, (c)~50 nm, (d)~7.5 nm.

Typical transmission electron microscopy (TEM) images of In_2O_3 and ITO NCs synthesized under identical conditions are shown in **Figure 2.7**. In the absence of Sn^{4+} precursor the described synthesis yields only well-dispersed *bcc*-In_2O_3 NCs having spherical morphology and an average diameter of ca. 9 nm (**Figure 2.7a**). Parts b and c of **Figure 2.7** show fractions of *rh*-ITO and *bcc*-ITO NCs, respectively, isolated from the same batch ([Sn]/[In] = 0.15) by size selective precipitation. The small *rh*-ITO NCs have an average size of about 4.5 nm (**Figure 2.7b**) and corundum crystal structure (**Figure 2.7b**, inset). Surprisingly, *bcc*-ITO NCs are isolated as flowerlike clusters with relatively

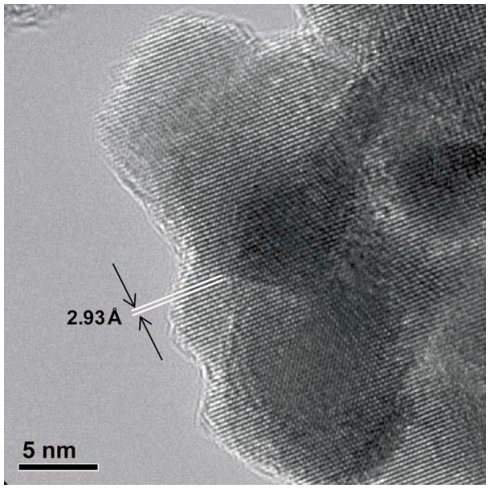

Figure 2.8 Lattice resolved TEM image of a single flower-like cluster assembled from *bcc*-ITO nanocrystals. The cluster is single crystalline, as evidenced from the continuous lattice fringes, indicating the oriented attachment of nanocrystals. The measured lattice spacings of 2.93 Å correspond to {222} d-spacing of *bcc*-In_2O_3.

uniform sizes of ca. 50 nm (**Figure 2.7c**). **Figure 2.7d** shows high resolution TEM image of a cluster assembled from *bcc*-ITO NCs. An average size of NCs within the cluster is about 7.5 nm, somewhat smaller than the size of free-standing NCs obtained in the absence of Sn^{4+} precursor. This reduction in size is consistent with the inhibition of NC growth in the presence of impurity ions. Importantly, lattice fringes in the nanoflower structures are extended over a number of NCs

and often across the entire cluster (**Figure 2.8**), indicating a spontaneous alignment and fusion of constituent NCs. This observation strongly suggests an oriented attachment of *bcc*-ITO NCs.

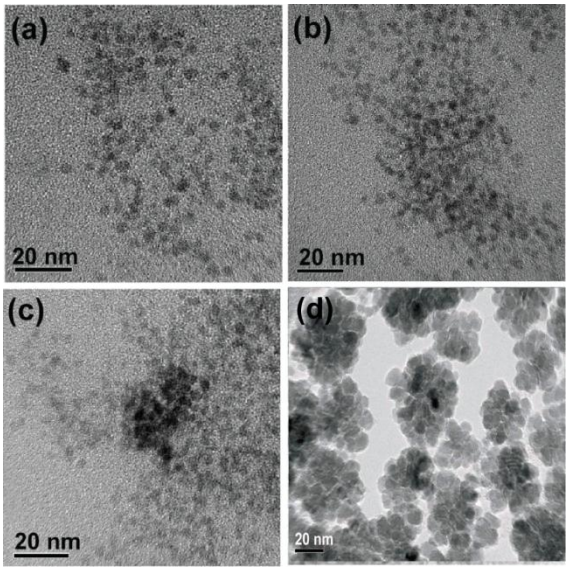

Figure 2.9 TEM images of ITO NCs 5 (a), 10 (b), 20 (c), and 30 min (d) after reaching the final reaction temperature (250 ℃). The images show temporal evolution of flowerlike clusters from NCs.

Oriented attachment has been associated with attractive van der Waals interactions between NCs [47,48]. It has been shown that most NCs possess permanent dipole moment, likely due to noncentrosymmetric crystal lattice or anisotropic distribution of localized surface charges [49]. The dipole-dipole interactions have been proposed to lead to the oriented attachment of NCs along particular crystallographic axes and the formation of one-dimensional nanostructures (nanowires) [47,48]. Three-dimensional assembly of *bcc*-ITO NCs in this work indicates uniform NC interactions in all directions.

It has been suggested that pure In_2O_3 NCs can spontaneously undergo oriented attachment at the early stages of the growth when they are not well-developed and when there is a diminished stabilization by organic ligands (limited ligand protection (LLP) method) [34]. In our work the flower-shaped *bcc*-ITO NC clusters were obtained in the identical way as undoped free-standing In_2O_3 NCs with full ligand protection, and the oriented attachment was observed for larger NCs at a more advanced growth stage. The presence of electrolytes has been shown to lead to adsorption of ions on In_2O_3 surfaces, which significantly enhances the surface charge density

[50]. ITO NCs were synthesized using $SnCl_4 \cdot 5H_2O$ as a precursor, which increases the ionic strength of the reaction mixture mostly due to the presence of Cl^- ions. Adsorption of Cl^- ions on NC surfaces could lead to lower NC surface coverage by organic molecules (oleylamine), which decreases the surface protection and favors the nanoflower cluster formation, as described by LLP hypothesis. We note that In_2O_3 nanoflowers in the work of Narayanaswamy et al [34] were obtained using indium acetate ($In(Ac)_3$) which is, similarly to $InCl_3$, an ionic precursor and can also cause the surface exchange of protective organic ligands by acetate anions. The charging of the NC interfaces by Cl^- adsorption could also lead to a local dipole moment formation [49], fostering van der Waals interactions and assembly of NCs.

To test the influence of ionic strength on the *bcc*-ITO NC self-assembly due to adsorption of chloride ions, we performed the synthesis of In_2O_3 NCs under the same conditions using $InCl_3$ as a precursor. The formation of nanoflowers with essentially the same structure and morphology was observed, clearly indicating the role of Cl^- ions on the NC assembly. We observed similar NC assembly (although to varying degrees) using other ionic precursors, including $In(NO_3)_3$, suggesting a general role of the ionic strength in NC attachment. Mobility of a NC joining a cluster could then allow for its reorientation and the oriented attachment in order to minimize the

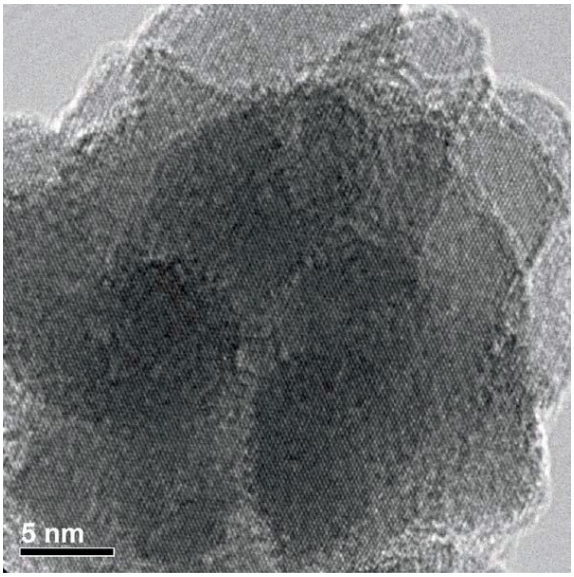

Figure 2.10 High resolution TEM image of a single flower-like cluster assembled from *bcc*-ITO nanocrystals. The parallel lattice fringes extend over the entire cluster, confirming an oriented attachment.

total surface free energy. This process is evident from the high resolution TEM image in **Figure 2.10**. We further explored why *bcc*-ITO NCs undergo oriented attachment while *rh*-ITO NCs do not, by monitoring the evolution of the nanoflower formation (**Figure 2.9**). At the early stages of NC growth the initially formed *rh*-ITO NCs are well-dispersed (**Figure 2.9a**). As the reaction progresses, NCs grow in size and begin to cluster (**Figure 2.9b,c**). After 30 min well-defined nanoflowers consisting of larger NCs coexist with smaller freestanding NCs (**Figure 2.9d**). With further NC growth, nanoflowers became a prevalent reaction product. The images in **Figure 2.9** demonstrate a direct correlation between NC growth and attachment and are consistent with the NC assembly due to increasing adsorption of ions and concurrent displacement of oleylamine during NC growth. The dipole moment associated with surface charging has been shown to increase linearly with NC size [49], which could also partly explain significantly more pronounced aggregation and assembly of larger *bcc*-ITO NCs compared to smaller *rh*-ITO NCs. On the basis of our control experiments, we conclude that the adsorption of Cl^- ions and displacement of the protective ligands on the NC surfaces are primarily responsible for promoting attractive van der Waals interactions between NCs. The obtained NC flowerlike clusters are uniform in size, suggesting homogeneous van der Waals interactions. The formation of ITO NCs with different sizes and structures and their isolation from the reaction mixture are shown schematically in **Figure 2.11**. Further studies of the interactions of TCO-NCs, including the detailed mechanism of the resulting self-assembly, are currently under way in our laboratory.

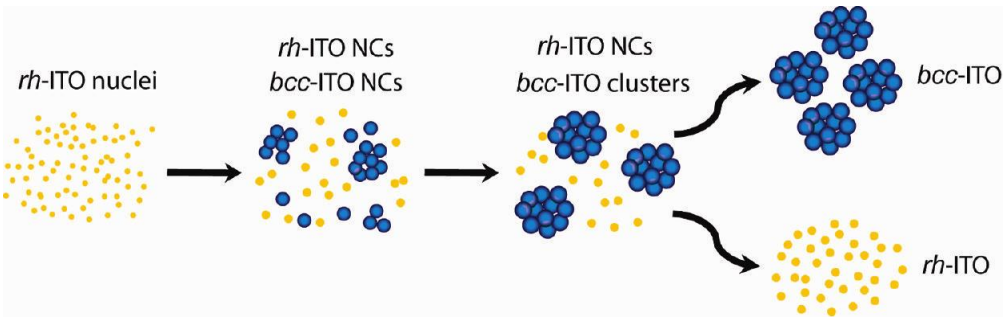

Figure 2.11 Schematic illustration of the growth and assembly of ITO NCs. Nanocrystal phase separation is based on the difference in NC sizes and their oriented attachment (*rh*-ITO NCs are shown as yellow and *bcc*-ITO NCs as blue spheres).

2.3.4 Size and Phase Dependence of the Free Electron Concentration in ITO NCs

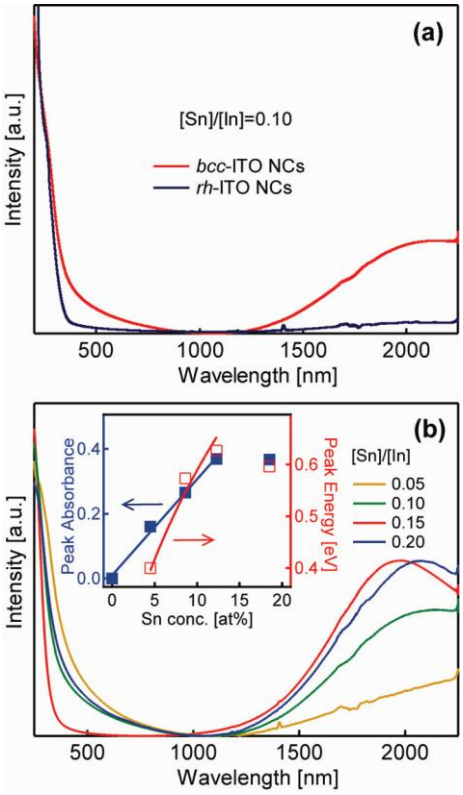

Figure 2.12 (a) Absorption spectra of *bcc*-ITO (red line) and *rh*-ITO NCs (blue line), obtained by NC size selection from the sample synthesized with the starting precursor concentrations corresponding to [Sn]/[In] = 0.10. (b) Band-gap-normalized (adjust to be the same band gap absorption) absorption spectra of *bcc*-ITO NCs isolated from the samples synthesized with different precursor concentration ratios ([Sn]/[In]), as indicated in the graph. Inset: maximum plasmon band absorbance in near IR region (blue squares) and peak energy position (open red squares) as a function of Sn^{4+} doping concentration. The blue and red lines are the best linear and square root fits to the experimental data (**eq 2.1** and **eq 2.2**), respectively.

To understand the electronic structure and the optical and electrical properties of ITO NCs with different crystal structure and composition, we performed absorption spectroscopy studies. **Figure 2.12a** compares the absorption spectra of typical *rh*- and *bcc*-ITO NCs. Both spectra exhibit a shoulder in the UV region at ca. 260 nm (*rh*-ITO NCs) or 275 nm (*bcc*-ITO NCs). These transitions are assigned to the interband absorption (band-gap absorption) and are blue-shifted with respect to bulk and undoped *bcc*-In_2O_3 NCs owing to the quantum size [32] or Burstein-Moss effect [29]. The onset of the broad featureless band in the near-infrared (NIR) region, observed only for *bcc*-ITO NCs (**Figure 2.12a**), is of a particular interest in this study. It

arises from the resonant excitation of NC plasmons by electromagnetic radiation, which occurs in the NIR in the case of *bcc*-ITO NCs. The interference from the vibrational overtones of solvent molecules prevented the clear data collection at lower energies. This plasmon band is associated with free electrons in the conduction band and can be quantitatively described by the modified Drude-Lorentz theory [25,29], originally developed as a model for the free electron gas in metals [51]. Based on this model, the absorption coefficient (α) associated with the free electrons in semiconductors is directly proportional to the charge carrier density (*N*) [51], according to the following expression:

$$\alpha_{\text{free electrons}} = \frac{Ne^2}{m^*\varepsilon_0 nc\tau\,\omega^2} \qquad \textbf{(eq 2.1)}$$

where *e* is the electron charge, *m** is the effective mass of an electron, ε_0 is the vacuum permittivity, τ is the mean time between two electron scattering events, *n* is the refractive index of undoped semiconductor, and *c* and *ω* are the speed and frequency of light, respectively. This transition often gives degenerately n-doped oxides a blue color and is, therefore, referred to as the blue band. The energy position of the plasmon band is directly proportional to the electron plasma frequency (ω_p), which has a square root dependence on the free electron concentration:

$$\omega_p = \sqrt{\frac{Ne^2}{m^*\varepsilon_{opt}\,\varepsilon_0}} \qquad \textbf{(eq 2.2)}$$

where $\varepsilon_{opt} = n^2$ is a dielectric constant measured in the transparent region of the spectrum of an undoped semiconductor. The plasmon band maxima (solid blue squares) and positions (open red squares) in *bcc*-ITO NC absorption spectra normalized for the band-gap intensity are plotted as a function of Sn^{4+} doping concentration in **Figure 2.12b** (inset). The absorption intensity increases linearly with increasing Sn^{4+} doping concentration as expected from **eq 2.1** (blue line in the inset is a linear fit to the experimental data), owing to the corresponding increase in the free electron concentration (*N*). Above the doping concentration of ca. 12 at. % the absorbance declines due to electron trapping around Sn^{4+} doping sites, which decreases the free electron density [24]. The plasmon band energy dependence on the Sn^{4+} doping concentration is also shown in **Figure 2.12b** (inset). The plasmon band shifts to shorter wavelengths (higher energies) with increasing Sn^{4+} concentration up to ca. 12 at. %, at which point it reverses the trend. Peak energy positions are readily fit to **eq 2.2** for Sn^{4+} doping concentrations below ca. 12 at. % (red line). Based on the

representative electronic structure and optical parameter values for bulk *bcc*-In_2O_3 ($m^* = 0.3m_0$, $\varepsilon_{opt} = 4.0$) [52,53], the maximum concentration of free electrons in *bcc*-ITO NCs is determined to be ca. 3.3×10^{20} cm^{-3} (for 12.3 at. % of Sn^{4+}). Both plasmon energy and intensity behaviors are in agreement with the Drude predictions for the free electron gas formation in semiconductors. The conductivity of ITO NCs in the properly prepared pellets has been shown to follow the same trend [28], confirming the correlation between the plasmon band and electrical conductivity, as predicted by the Drude model. The conductivity depends, however, on a number of factors, including the NC networking, connectivity, and surface terminations, and as such it is a less direct method than the optical absorption for determining charge carrier concentration in the case of colloidal NCs.

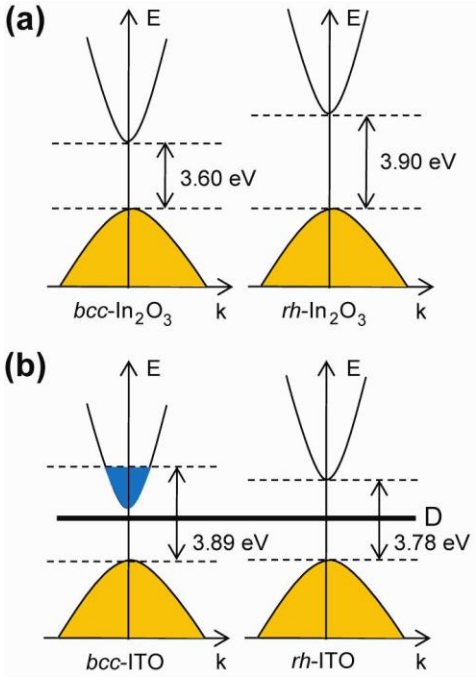

Figure 2.13 Schematic representation of the band structure of (a) undoped *bcc*- and *rh*-In_2O_3 NCs and (b) *bcc*- and *rh*-ITO NCs with 12.3 at. % Sn^{4+}. Solid black line denotes donor states (D), and the blue area indicates the filled conduction band states in (b). The apparent ("optical") band gap of ITO NCs in (b) is determined by two competing mechanisms: (i) widening due to the Burstein-Moss effect, which is dominant for *bcc*-ITO NCs, and (ii) narrowing due to many-body effects, which is dominant for *rh*-ITO NCs.

Unlike the oriented-attached *bcc*-ITO NCs, which exhibit a very strong blue band (**Figure 2.12a**, red trace), *rh*-ITO NCs show very little absorption in the NIR region, indicating low charge carrier concentration (**Figure 2.12a**, blue trace). This is consistent with a markedly different color of these two parts of the same sample. While *bcc*-ITO NCs have deep blue color, *rh*-ITO NCs are colorless for all starting concentrations of Sn^{4+}. These results indicate that under identical synthesis conditions and for similar doping concentrations Sn^{4+} dopants lead to much higher free electron concentration in *bcc*-ITO than in *rh*-ITO NCs. Such a strong dependence of the electrical properties may be attributed to different electronic structure of Sn^{4+} dopants in these two structures. Sn^{4+} ions introduce donor states in In_2O_3 NCs, and their ability to donate electrons to the conduction band is directly related to Sn^{4+} energy levels relative to the In_2O_3 NC band gap. The position, dispersion, and character of the conduction band determine the characteristics of the band structure and, hence, the optoelectrical properties of ITO [54]. As discussed above, the size and structure of the *bcc*- and *rh*-In_2O_3 dimorphs are critical for defining these parameters [32,46] and, therefore, the relative position of the donor states in given ITO NCs. The direct band gap of 3.75 eV has widely been referenced for In_2O_3. This value has recently been revised to 2.9 and 3.0 eV for *bcc*- and *rh*-In_2O_3, respectively [55]. It has been suggested that the optical transitions from the valence band minimum to the conduction band maximum are dipole moment forbidden in *bcc*-In_2O_3 due to the symmetry of the cubic bixbyite crystal structure [56]. These transitions are not forbidden in *rh*-In_2O_3, but the density of states near the bottom of the conduction band has been found to be very small compared to typical direct band-gap semiconductors [55]. Consequently, the onset of the band-gap absorption appears systematically higher in both dimorphs.

Figure 2.13 shows a schematic illustration of the electronic structure of undoped *bcc*- and *rh*-In_2O_3 NCs (**Figure 2.13a**), and *bcc*- and *rh*-ITO NCs (**Figure 2.13b**), determined from the absorption spectra. We defined the apparent band gaps by extrapolating the leading edge of the optical absorbance to the baseline of the absorption spectra. The band gap of *rh*-In_2O_3 NCs is ca. 0.3 eV larger than that of *bcc*-In_2O_3 NCs due to a strong quantum size effect in sub-5 nm diameter *rh*-In_2O_3 NCs (**Figure 2.13a**) [32]. The position of the donor states with respect to the conduction band minimum determines the donor activation energy and the concentration of electrons in the conduction band. Owing to a larger band gap of *rh*-In_2O_3 compared to *bcc*-In_2O_3 NCs, the donor activation energy is significantly higher in *rh*-ITO NCs, prohibiting any

appreciable concentration of free electrons in the conduction band (**Figure 2.13b**). The final band-gap energies in ITO NCs shown in **Figure 2.13b** are the result of the two opposing mechanisms: (1) band gap widening due to the Burstein-Moss effect associated with increased conduction band occupancy (dominant for *bcc*-ITO NCs) and (2) band-gap narrowing due to many-body interactions, such as electron-electron and electron-ion scattering (dominant for *rh*-ITO NCs). Assuming a similar position of the donor states in both dimorph NCs, the donor activation energy is estimated to be about 0.3 eV higher in *rh*-ITO than in *bcc*-ITO NCs. The necessity to simultaneously control charge carrier density and optical transparency therefore renders well-designed *bcc*-ITO NCs favorable building blocks for functional structures and devices.

2.4 Conclusions

In summary, we reported a comparative study of doping Sn^{4+} into colloidal In_2O_3 NCs having different crystal structures. We showed that the presence of $SnCl_4 \cdot 5H_2O$ as the tin precursor leads to inhibition of NC growth, causing bimodal size distribution of ITO NCs. This bimodal size distribution is accompanied by the bimodal phase, such that NCs below ca. 5 nm in size have corundum crystal structure (metastable phase), while larger NCs have cubic bixbyite structure. Cubic bixbyite ITO NCs exhibit strong absorption in the NIR region peaking at around 2000 nm. This absorption is a result of the resonant plasmon oscillations which arise from the free conduction band electrons in *bcc*-ITO NCs and can be described by the Drude model of the free electron gas. This behavior is distinctly different from *rh*-ITO NCs which do not exhibit a significant absorption in the NIR. The difference between the free electron concentrations in *bcc*- and *rh*-ITO NCs arises from a different electronic structure of the donor states originating from Sn^{4+} in these two NC dimorphs. This difference is associated with significantly larger donor activation energy in *rh*-ITO NCs compared to *bcc*-ITO NCs. The results in this article emphasize an important point that seemingly subtle changes in the size and crystal structure of complex oxide NCs cause dramatic difference in their electronic structure and properties. Colloidal methods and the size-structure dependence allow for accessibility, precise tuning, and separation of different NC phases and therefore a convenient engineering of the electronic structure and properties of TCO-NCs as functional building blocks.

Chapter 3 Size-Tunable Phosphorescence in Colloidal Metastable γ-Ga_2O_3 Nanocrystals

3.1 Introduction

The past two decades have seen tremendous advancements in the area of synthesis and properties of colloidal nanocrystals (NCs). These advancements have largely been fueled by the technological promise of these nanostructures in photonics [1], electronics [2], photovoltaic solar cells [3], catalysis [4], and biological imaging [5]. Among different types of colloidal NCs, II–VI semiconductor quantum dots have been most widely studied because of their size-tunable optical properties associated with quantum confinement effect [6]. This photoluminescence (PL) tunability has been particularly attractive for photonic devices, including light emitting diodes (LEDs) [1]. The optical studies of wide band gap oxide semiconductor NCs, also known as transparent conducting oxide (TCO) NCs, have only recently started to emerge [7-11], motivated by their functional properties and inexpensive, environmentally friendly preparation. TCOs such as ZnO, SnO_2 and In_2O_3 are transparent in the visible and have high n-type conductivity [12,13], which is promising for the next generation optical, electrical, and photovoltaic devices. Photoluminescence of TCO-NCs is usually dominated by surface complex formation [7] or defect-based deep-level emission [8-10] with a small or negligible contribution from band edge UV emission. Developing the methods to control the PL energy and efficiency in these materials is, therefore, of significant interest.

Gallium oxide (Ga_2O_3) has one of the largest band gaps among TCOs ($E_g \approx 4.9$ eV). It is a polymorphic material, exhibiting five different crystal structures (α, β, γ, δ and ε phases) [14]. The investigations of Ga_2O_3 have mainly focused on monoclinic β-phase due to its thermal stability [13,15-18]. The other four phases have only been sparingly studied [8,19,20]. Previous studies of PL of β-Ga_2O_3 have indicated ultraviolet (UV) and blue emission upon the band gap excitation, depending on the preparation conditions and a post synthetic treatment [15-18]. UV emission has been attributed to the recombination of a self-trapped exciton, and is mostly independent of the sample treatment [15,18]. The blue emission arises from the recombination of an electron trapped on a donor (oxygen vacancy, V_O^x) and a hole trapped on an acceptor (gallium-oxygen vacancy pair, $(V_O, V_{Ga})^x$) [15,16]. The large Stokes shift of the blue luminescence

suggests the localized nature of recombining electrons and holes. This emission, known as the donor-acceptor pair (DAP) recombination, is strongly correlated with the n-type electrical conductivity, indicating that the corresponding donor states are rather shallow [13,15,16]. Metastable γ-Ga_2O_3 has a defective spinel-type structure (Fd3m space group), which is similar to γ-phase Al_2O_3, with Ga^{3+} ions occupying the octahedral (O_h) and tetrahedral (T_d) sites ($Ga^{3+}(T_d)/Ga^{3+}(O_h) \approx 0.6$) [20].

In this chapter, I report the synthesis of truly colloidal γ-Ga_2O_3 nanocrystals (NCs) and, for the first time, demonstrate size-tunable PL in Ga_2O_3. The observed PL is dominated by associated donor-acceptor pair recombination and has a lifetime of several milliseconds. This electron-hole recombination between charged defect sites acting as donors and acceptors is strongly influenced by Coulombic interactions and, as such, is dependent on their separation. These results allow for predictable tuning of the optical properties of Ga_2O_3 and demonstrate the possibility of manipulating the localized defect interactions through NC size. Also, we demonstrate *in-situ* chemical control and optimization of the DAP emission of colloidal γ-Ga_2O_3 NCs by controlling the internal defect formation in the solution phase. The presence of an oxidizing agent reduces the PL intensity, while the presence of a reducing agent enhances the PL intensity by determining the concentration of oxygen vacancies in NCs. The concentration of the oxygen vacancies can also be controlled by kinetic annealing of NCs in solution. Owing to the chemical control of defect-induced PL and conductivity, colloidal Ga_2O_3 NCs have the potential to be used as building blocks in opto-electonics, sensors and catalysis.

3.2 Experimental Section

3.2.1 Materials

All reagents and solvents used for the synthesis of Ga_2O_3 nanocrystals are commercially available. Gallium acetylacetonate (99.99 %) was purchased from Strem Chemicals. Oleylamine (70 %) and tri-*n*-octylphosphine oxide (90 %) were purchased from Aldrich Chemical Co. Toluene (99.98 %, EMD Chemicals), hexanes (99.9 %, Fischer Scientific) and absolute ethanol were all used as received. All gasses (compressed argon (>99 %, impurity H_2O, N_2, O_2), oxygen (high purity, grade 4.3, 99.993%) and hydrogen (high purity, grade 5.0, 99.999%) were purchased from Praxair.

3.2.2 Synthesis of Ga_2O_3 Nanocrystals

The size-controlled synthesis of colloidal γ-Ga_2O_3 NCs was performed in oleylamine (OA) as a coordinating solvent. In a 100 mL flask 0.5 g of gallium acetylacetonate ($Ga(acac)_3$) was mixed with 7.0 g of OA, and the temperature of the mixture was raised to 80 ℃. After $Ga(acac)_3$ was fully dissolved, the solution was degassed and heated to 200-310 ℃ at the average rate of 3 ℃/ min while continuously stirring under a flow of argon. This reaction mixture was refluxed at the desired temperature for 7 h. The NCs were then precipitated with an equal volume of ethanol and centrifuged at 3000 rpm for 5 min. The obtained white powder was washed 3 times with ethanol followed by centrifugation. Finally, NCs were capped with tri-*n*-octylphosphine oxide (TOPO) and dispersed in hexane or toluene. The average size can be tuned by growth temperature from 3.3 ± 0.5 nm (at 200 ℃) to 6.0 ± 1.1 nm (at 310 ℃).

3.2.3 Measurements and Data Analysis

The crystallization and phase of the nanocrystals were analyzed by X-ray diffraction (XRD). XRD patterns were collected with an INEL powder diffractometer with a position-sensitive detector, utilizing monochromatic Cu $K_{\alpha 1}$ radiation (λ=1.5406 Å).

Transmission electron microscopy (TEM) images were obtained on FEI Titan 80-300 Cryo-In-situ microscope operating at 300 kV. The specimens were prepared by dropping dilute colloidal suspensions of NCs in toluene on copper grids (300 mesh) with lacey formvar/carbon support films purchased from Ted Pella, Inc. The absorption spectra of γ-Ga_2O_3 NCs dispersed in hexane were collected with a Varian Cary 5000 UV-vis-NIR spectrophotometer. Quartz cuvettes (*Spectrosil*, Starna Cells Inc.) having the transparency range 170-2700 nm and the standard 1 cm optical path length were used for collecting the absorption spectra.

Photoluminescence measurements were recorded with a Varian Cary Eclipse Fluorescence Spectrophotometer. For delayed photoluminescence spectra the samples were excited at the maximum of the excitation band with pulsed Xenon flash lamp and the emission intensity at each point in a spectrum was recorded 2 ms after the excitation. The total decay time for each data point before the sample was excited again was 0.02 s. The time-resolved data were collected upon excitation of nanocrystals into the band gap using a Xenon flash lamp. The data points were collected at the peak of the low-energy component (delayed photoluminescence spectra) with the initial delay of 3 μs and the data collection time (gate time) of 1 μs for each point.

For a direct comparison of PL intensities under different atmosphere, the concentrations of

colloidal NCs in hexane were adjusted to exhibit absorption of 0.1 at 230 nm. For the delayed PL measurements, the samples were excited at 230 nm with a pulsed Xenon flash lamp, and the emission intensity at each point was recorded with various delay times (0.1, 0.2, 0.5 and 1ms) after excitation. Relative quantum yields of γ-Ga_2O_3 NC samples were calculated using quinine bisulfate (QBS) as the reference substance. A solution of QBS was prepared in 1 N H_2SO_4 as previously reported [23]. The quantum yield of QBS under these conditions was determined to be 0.55.

3.3 Results and Discussion

3.3.1 Sample Characterization

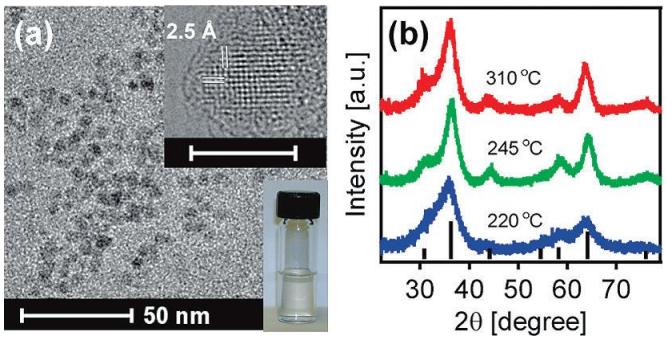

Figure 3.1 (a) TEM image of 6.0 ± 1.1 nm Ga_2O_3 NCs synthesized at 310 ℃. Insets: (Top) High resolution TEM image of a single NC (scale bar, 5 nm). Lattice spacings match (311) d-spacing of cubic Ga_2O_3. (Bottom) Photograph of a NC colloidal suspension. (b) XRD patterns of Ga_2O_3 NCs prepared at different temperatures. Black lines: XRD of bulk cubic Ga_2O_3.

A transmission electron microscopy (TEM) image of typical NCs synthesized at 310 ℃ is shown in **Figure 3.1a**. The NCs have quasispherical morphology with an average size of 6.0 ± 1.1 nm (**Figures 3.2, 3.3**), and form clear colorless suspensions in nonpolar organic solvents (**Figure 3.1a**, bottom inset). These NCs are highly crystalline and have a cubic crystal structure (γ-Ga_2O_3), as evident from the high resolution TEM image (**Figure 3.1a**, top inset) and X-ray diffraction (XRD) pattern (**Figure 3.1b**, red). The broadening of XRD peaks increases for NCs synthesized at lower reaction temperatures due to a decrease in average NC sizes (**Figure 3.1b**). We have recently shown that metastable phases of TCOs can be spontaneously stabilized with high selectivity in colloidal NCs by controlling their sizes and growth kinetics, owing to the surface energy and surface stress contributions [2,13]. The formation of γ-Ga_2O_3 NCs

demonstrates the generality of that process and indicates that the size-structure correlation in colloidal syntheses leads to a high degree of structural selectivity and phase purity even for materials that exhibit several allotropic modifications.

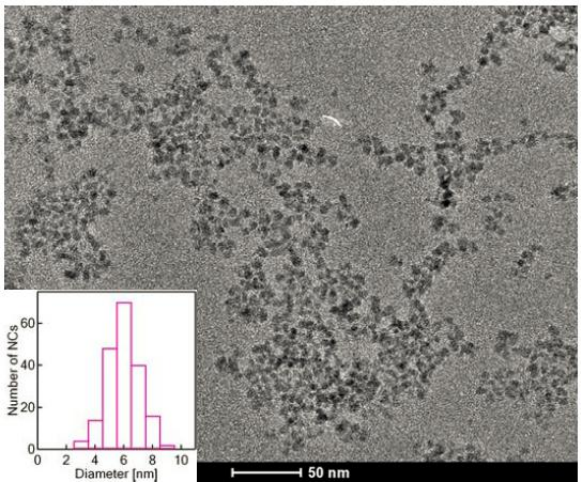

Figure 3.2 Overview TEM image of γ-Ga_2O_3 nanocrystals synthesized at 310 ℃ as described. Inset: Nanocrystal size distribution; the distribution was determined from TEM images by measuring the diameters of ca. 200 nanocrystals. The average nanocrystal size was determined to be 6.0 ± 1.1 nm.

3.3.2 Tunable Luminescence of γ-Ga_2O_3 Nanocrystals

The absorption spectra of the series of γ-Ga_2O_3 NCs are nearly identical (**Figure 3.4**) indicating the negligible effect of quantum confinement in the studied size range, contrary to some previous suggestions [11]. This is expected based on the large effective mass of electrons ($m_e \approx 0.34m_0$) and tight exciton binding in Ga_2O_3 [12]. **Figure 3.5a** shows PL spectra of γ-Ga_2O_3 NCs ranging in diameters from 3.3 to 6.0 nm, excited in the conduction band. The syntheses resulted in NCs which are strongly emissive from near-UV to blue, with an average quantum yield of 23%. The observed PL is size tunable, and the spectra exhibit a significant red shift with increasing NC size. The large Stokes shifts (**Figure 3.6**) indicate a localized nature of recombining electrons and holes. A photograph of 3.3 and 6.0 nm diameter NC samples (**Figure 3.5b**) qualitatively illustrates the intensity and size dependence of the emitted light. These data, together with the PL spectra of bulk β-Ga_2O_3 (**Figure 3.7**), indicate that both size and structure play a key role in defining the properties of Ga_2O_3. Optical excitation of β-Ga_2O_3 through the

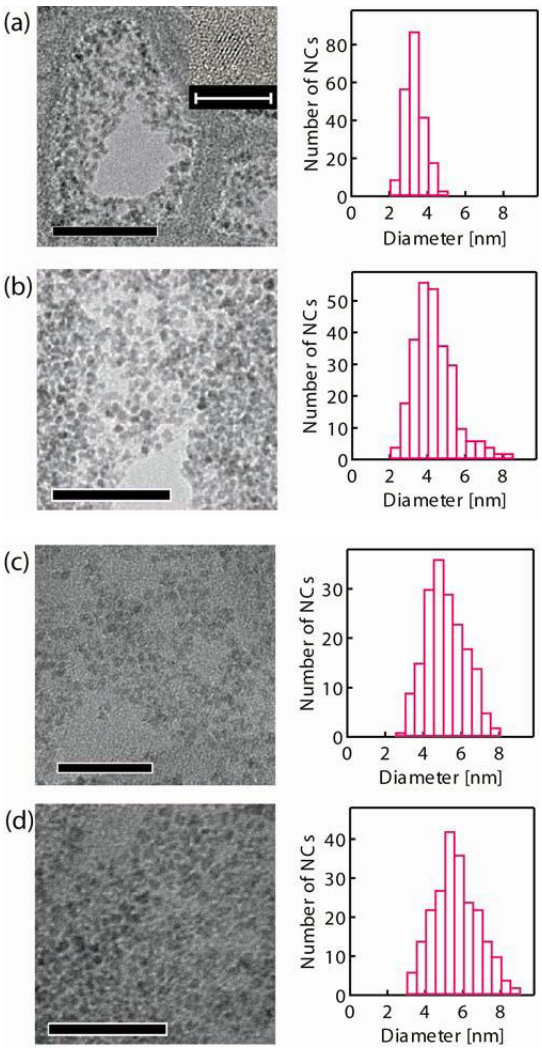

Figure 3.3 TEM images (left panels) and size distribution diagrams (right panels) of γ-Ga_2O_3 nanocrystals synthesized at different temperatures: (a)200 ℃, (b)220 ℃, (c)250 ℃, (d)280 ℃. The size distributions were determined from high resolution TEM images by measuring ca. 200 nanocrystals. Scale bars in TEM images are 50 nm. The average nanocrystal sizes are: (a) 3.3 ± 0.5, (b) 4.2 ± 0.9, (c) 5.1 ± 1.1, and (d) 5.5 ± 1.2 nm. Inset in (a) shows high resolution image of a single nanocrystal (scale bar, 5 nm).

band gap usually results in two different emission components, UV (high-energy) and blue (low-energy). UV emission has been attributed to the recombination of a self-trapped exciton, while the blue emission arises from the tunnel recombination of an electron on a donor with a hole on an acceptor, where the donor is an oxygen vacancy (V_O^X) and the acceptor could be either a gallium ion vacancy (V_{Ga}''') or a pair of charged vacancies ((V_O,V_{Ga})′) [10]. The dominant blue

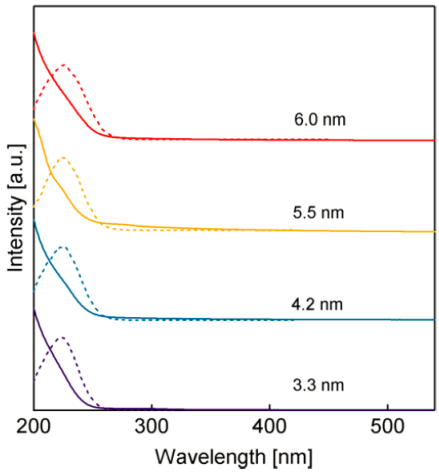

Figure 3.4 Absorption (solid lines) and excitation (dashed lines) spectra for a series of γ-Ga_2O_3 nanocrystals. The average NC sizes are shown in the graph. The band edge energies are essentially unchanged for all samples indicating negligible effect of quantum confinement in Ga_2O_3 in the studied size range.

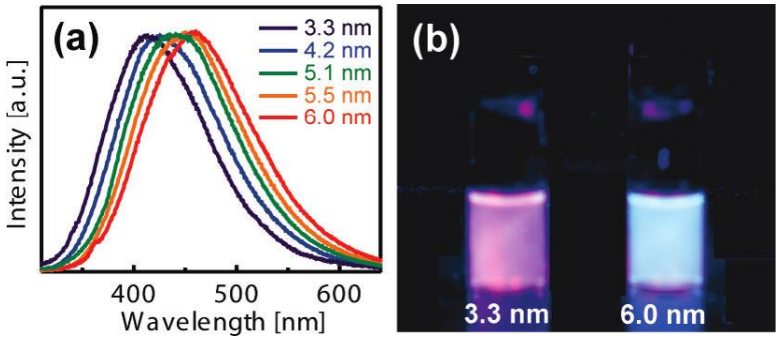

Figure 3.5 (a) 300 K PL spectra of γ-Ga_2O_3 NCs ranging from 3.3 to 6.0 nm excited with λ = 250 nm. (b) Photograph of colloidal 3.3 and 6.0 nm γ-Ga_2O_3 NCs illuminated with 250 nm UV light.

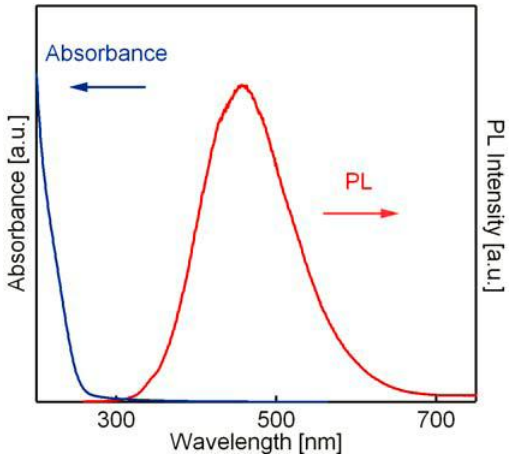

Figure 3.6 Absorption and photoluminescence spectra of 6.0 nm γ-Ga_2O_3 nanocrystals showing large Stokes shift consistent with the localized nature of the observed photoluminescence.

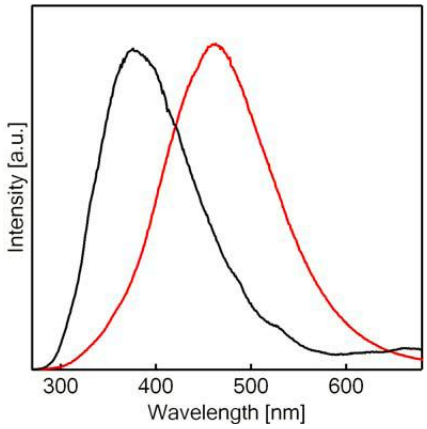

Figure 3.7 Photoluminescence spectra of bulk β-Ga_2O_3 powder (black trace) and 6.0 nm γ-Ga_2O_3 nanocrystals (red trace). The blue shift of the photoluminescence of bulk β-Ga_2O_3, which is opposite from the shifts observed for increasing sizes of γ-Ga_2O_3 nanocrystals (Figure 3.5a), may be attributed to the difference in the structure and energy levels of internal defects in β-Ga_2O_3 (bulk) and in γ-Ga_2O_3 (nanocrystals).

emission has a much longer lifetime [4] and can be distinguished by delayed PL measurements. **Figure 3.8a** shows the PL spectra of γ-Ga_2O_3 NCs 2 ms after excitation. For delay times t > 100 μs after excitation, the high-energy component vanishes (the half-life has been suggested to be ca. 30 ns in β-Ga_2O_3) [4], and the low energy component remains as phosphorescence. This afterglow persists for several milliseconds upon the initial excitation. The decay dynamics of this feature was studied for different NC sizes using time-resolved PL (**Figure 3.8b**). The decay curves cannot be fit accurately to either single or biexponential functions, suggesting that the decay dynamics is not driven by the transition probability of the recombination centers. Importantly, the decay rate is strongly size dependent and increases with decreasing NC size. The half-lives for 3.3, 4.2, and 6.0 nm NCs are determined to be 4.66, 4.90, and 5.67 μs, respectively. This phenomenon has not been previously reported due to the unavailability of colloidal NCs with controlled sizes and size distributions.

Both steady-state and time-resolved PL results can be considered in the context of the associated donor-acceptor pair (DAP) model [14]. According to this model an electron excited into the conduction band is trapped by a donor (in this case an oxygen vacancy). The first step in the relaxation process is a tunnel transfer of the electron from the donor to an acceptor to form a

trapped exciton. This step is followed by recombination of the

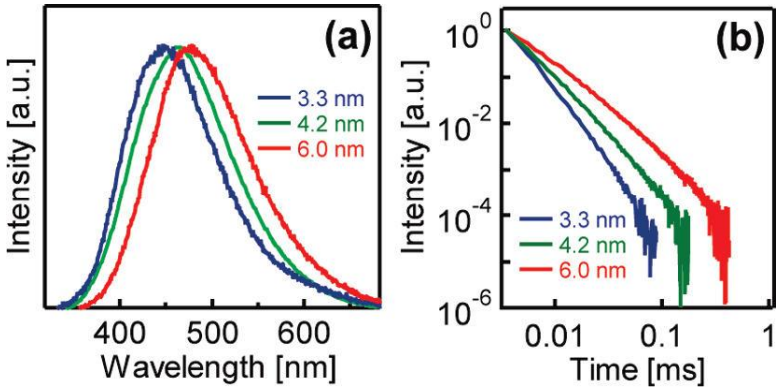

Figure 3.8 (a) Delayed PL spectra of γ-Ga_2O_3 NCs having different sizes, collected 2 ms after excitation into band gap. (b) Phosphorescence decay dynamics of γ-Ga_2O_3 NCs in (a). The samples were excited at 250 nm and measured at maximum of the phosphorescence peak.

exciton at the acceptor site. The energy of emitted light is determined by the Coulombic interactions between ionized donors and acceptors and can be expressed as:

$$E = E_g - (E_d + E_a) + E_C \pm nE_{phonon} \quad \textbf{(eq 3.1)}$$

where E_g is the band gap energy, E_d and E_a are the donor and acceptor binding energies, respectively, $E_C = e^2/4\pi\varepsilon r$ is the Coulombic interaction term, and E_{phonon} represents the energies of phonons involved in the radiative transitions. The average donor-acceptor separation (r) decreases with decreasing NC size leading to an increase in the emission energy. Assuming that E_d and E_a are size independent, r is estimated to be within an order of magnitude larger in 6.0 than in 3.3 nm NCs. The emission intensity arising from donor-acceptor recombination at time t depends on the concentration of the majority defects, in this case donors, and the recombination probability for a donor-acceptor pair with separation r[14].

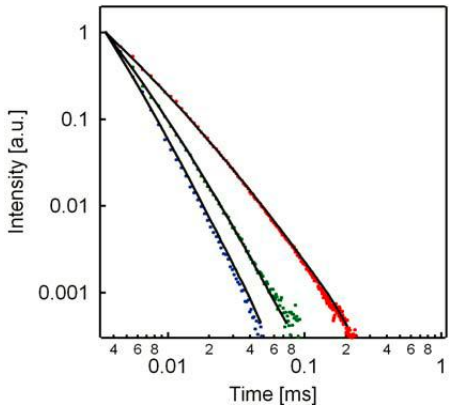

Figure 3.9 Calculated phosphorescence decay curves (black lines) for γ-Ga_2O_3 NCs with the diameters of 6.0 (red dots), 4.2 (green dots) and 3.3 nm (blue dots) using DAP model.

Shortening of the phosphorescence lifetime with decreasing NC size is therefore also associated with reduced distances between donors and acceptors. The calculated phosphorescence decay curves using modified DAP model are in very good agreement with the experimental data for different NC sizes (**Figure 3.9**) [14]. Taken together these data suggest that a decrease in *r* with decreasing NC size is a consequence of the higher concentration of point defects and smaller domain volumes. A higher defect concentration may be caused by a lower synthesis temperature and possibly a greater propensity for defect formation in NCs with higher surface areas.

3.3.3 In situ Tuning of the Blue Photoluminescence of Colloidal Ga_2O_3 Nanocrystals

Absorption and PL spectra of colloidal γ-Ga_2O_3 NCs synthesized in Ar atmosphere for different durations of time at 220 ℃ are shown in **Figure 3.10a**. The PL spectra correspond to the same concentrations of the NC suspensions, as evidenced from the identical absorption spectra. These

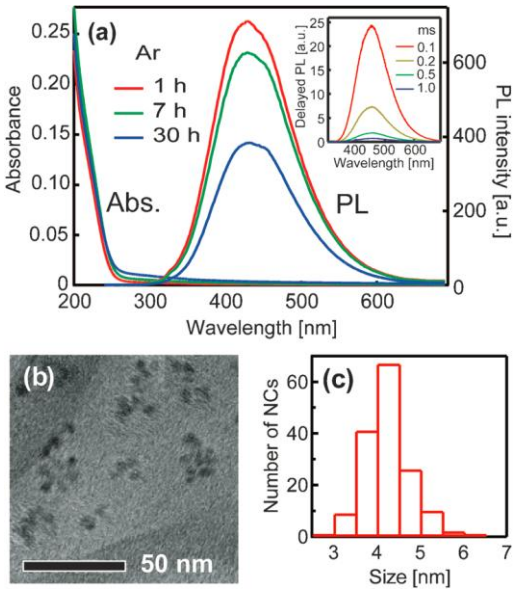

Figure 3.10 (a) Absorption and PL spectra of Ga_2O_3 NCs synthesized at 220 ℃ for 1 (red), 7 (green) and 30 h (blue). Inset: Delayed PL spectra of NCs prepared in 30 h synthesis, collected at different delay times upon excitation, as indicated in the graph. The samples were excited at 230 nm for the PL measurements. (b, c) TEM image (b) and the corresponding size distribution histogram (c) of Ga_2O_3 NCs synthesized for 1 h at 220 ℃.

PL spectra exhibit large Stokes shifts and show a broad blue emission with a maximum around 430 – 440 nm. This emission band can be assigned to the associated DAP recombination involving a few nearby pairs of V_O^x and $(V_O, V_{Ga})^x$ [8,15]. The PL intensity decreases with increasing synthesis time, falling by over 40 % for 30 h relative to 1 h reaction. Concurrently with the decrease in intensity the centre of gravity of PL bands experiences small but observable shifts to lower energies (ca. 430 nm for 1 h vs. 438 nm for 30 h).

Delayed PL spectra of NCs prepared in 30 h synthesis are shown in the inset of **Figure 3.10a**. The emission intensity decreases with increasing delay time, but the spectra can be recorded even after 1 ms upon excitation. To study the effect of NC size on the blue emission in Ga_2O_3 NCs we examined the samples prepared at different temperatures by transmission electron microscopy (TEM). The average NC size for the sample synthesized for 1 h at 220 ℃ is 4.2 ± 0.6 nm (**Figure 3.10b** and **c**). The NC sizes and their distributions experience negligible changes for different reaction times (**Figure 3.11**), indicating that NC growth reaches the equilibrium point after less than 1 h of heating. The nanocrystals have γ-Ga_2O_3 crystal structure (**Figure 3.12**) and their sizes are predominantly determined by the reaction temperature rather than synthesis time.

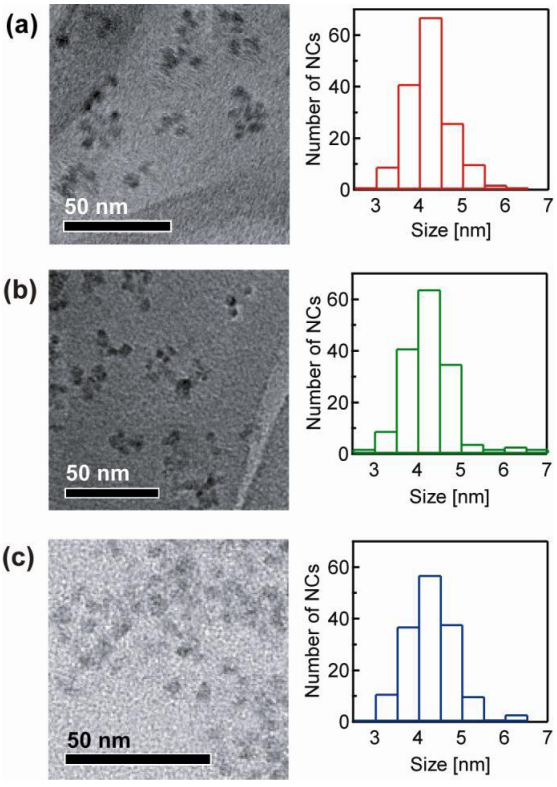

Figure 3.11 TEM images (left) and size distribution histograms (right) of γ-Ga_2O_3 NCs synthesized at 220 ℃ for (a) 1, (b) 7 and (c) 30 hours. The average NC sizes are indicated in the figure. The data demonstrate negligible change in the average NC size with increasing heating time. Average size: (a)4.2 ± 0.6 nm, (b) 4.2 ± 0.6 nm, (c) 4.3 ± 0.7 nm.

Clearly, the observed emission intensity dependence on the synthesis duration cannot arise from a simple change in the NC size. Instead, this dependence can be explained by the defect formation in the NCs. With a prolonged heating time at elevated temperatures the NCs undergo kinetic annealing in solution, leading to a lower concentration of structural defects and a decrease in the PL intensity. Furthermore, the defect concentration determines the average separation between oppositely charged donor and acceptor vacancy sites. Coulombic term contribution to the PL energy is inversely proportional to the separation between donor and acceptor sites ($E_C = e^2/4\pi\varepsilon r$, where e is the electron charge, ε is the absolute permittivity of material (dielectric constant) and r is the donor-acceptor separation) [8,21], leading to a slight shift of PL bands to lower energies for kinetically annealed NCs having a low defect concentration. Given the statistical removal of defects (donor and acceptor sites) in NCs during solution phase annealing, the red shift of the PL band, due to an increase in the average defect separation, is less pronounced than the decrease in the PL intensity.

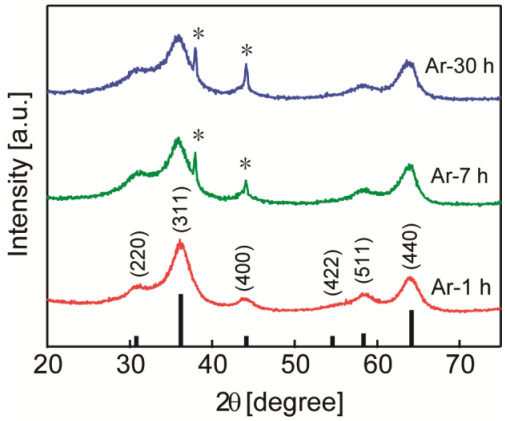

Figure 3.12 XRD patterns of γ-Ga_2O_3 NCs synthesized at 220 ℃ in argon flow for different durations, as indicated in the graph. The vertical red lines represent the XRD pattern of bulk γ-Ga_2O_3 NCs (JCPDS 20-0426). The stars indicate the peaks from Al sample holder.

Similar growth behaviour and size distribution is also observed for larger NCs synthesized at 310 ℃. The average NC size at this temperature is 6.0 ± 1.1 nm. Steady state and delayed PL

spectra of Ga_2O_3 NCs synthesized for 1, 7 and 30 h at 310 ℃ are shown in **Figure 3.13**. The PL maxima are observed between 450 and 460 nm and decrease in intensity with increasing heating time, similarly to the samples prepared at 220 ℃. The integrated PL band intensities for different synthesis durations are plotted in **Figure 3.14a**. The PL intensity decreases more sharply for the higher reaction temperature. The integrated delayed PL intensities are plotted as a function of delay time in **Figure 3.14b**. The nanocrystals prepared at 220 ℃ decay at a significantly faster rate, indicating the smaller average separation between donor and acceptor sites, and therefore a stronger wavefunction overlap. Taken together, the data in **Figure 3.14** confirm kinetic annealing of the functional defects in colloidal TCO-NCs in solution, and the temperature control of the defect separation responsible for PL.

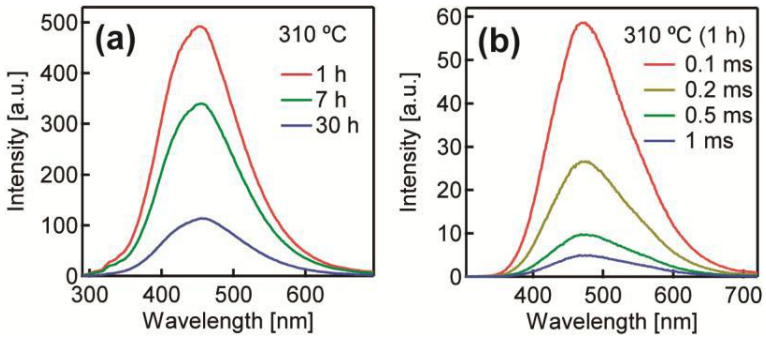

Figure 3.13 (a) PL spectra of Ga_2O_3 NCs synthesized at 310 ℃ for 1 (red), 7 (green) and 30 hours (blue). The spectra correspond to the same NC concentrations as those in Figure 3.10a. (b) Delayed PL spectra of the same NCs prepared for 1 hour, obtained 0.1 (red), 0.2 (olive), 0.5 (green) and 1.0 ms (blue) upon excitation with 230 nm pulse.

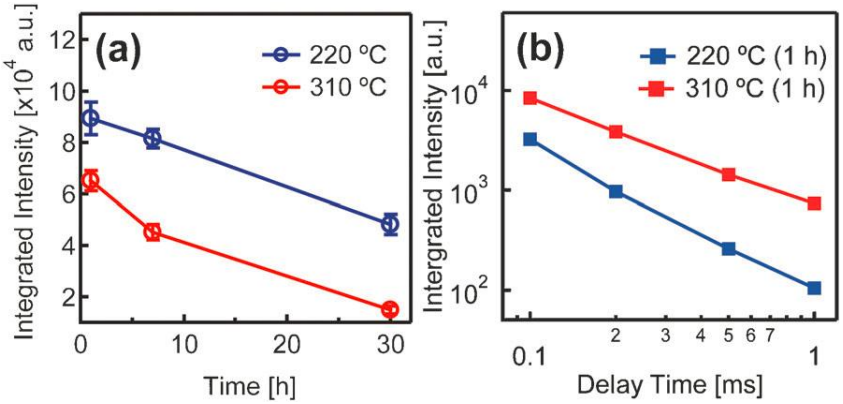

Figure 3.14 (a) Integrated PL intensity of colloidal Ga_2O_3 NCs as a function of the synthesis time at 220 and 310 ℃. The data correspond to the same NC concentrations. (b) Delayed PL intensity dependence on the delay times for NCs synthesized for 1 h at 220 and 310 ℃.

In order to make these materials broadly applicable for photonic technologies, and to further understand the mechanism of the blue emission, it is critical to expand the methods for the optimization of PL properties by *in situ* control of the defect formation in NCs in solution. Compared to semiconductor quantum dots, for which the quantum efficiency can be controlled by surface coating [22], enhancing defect-related PL requires the ability to impact the NC structure and stoichiometry in solution. Given the nature of the defects responsible for PL in Ga_2O_3 NCs (oxygen vacancies) we hypothesized that a reducing environment could lower the amount of oxygen in the reaction mixture and enhance the concentration of oxygen vacancies. To test this hypothesis we prepared Ga_2O_3 NCs in a hydrogen-rich environment. **Figure 3.15a** shows PL spectra of colloidal γ-Ga_2O_3 NCs synthesized at 220 ℃ for 1, 7 and 30 h in a controlled flow of a mixture H_2/Ar (H_2/Ar=3:7 flow ratio). Similarly to the synthesis in 99% argon, the PL intensity decreases with increasing synthesis times. However, the recorded PL bands have notably higher intensities and are slightly blue-shifted compared to those for NCs synthesized for the same amounts of time in Ar. Both of these effects indicate higher concentration of oxygen vacancies (*vide supra*). To confirm the origin of the change in PL we performed the same reaction in an oxidizing environment using a mixture of O_2/Ar as an oxidizing agent (**Figure 3.15b**). The spectra obtained for the same concentration of NCs, prepared at the same temperatures and having the same sizes have lower intensities than the analogous spectra of NCs prepared in Ar/H_2 or Ar. The preparation in oxygen-rich environment reduces the concentration of oxygen vacancy sites, leading to a significant decrease in PL intensity. Furthermore, 30 h solution-phase annealing in oxidizing conditions (**Figure 3.15b**, blue line) leads to a notable red shift of the PL band attesting to a pronounced increase in the average donor-acceptor separation. The results for the PL intensity of NCs prepared in different environments are summarized in **Figure 3.15c**.

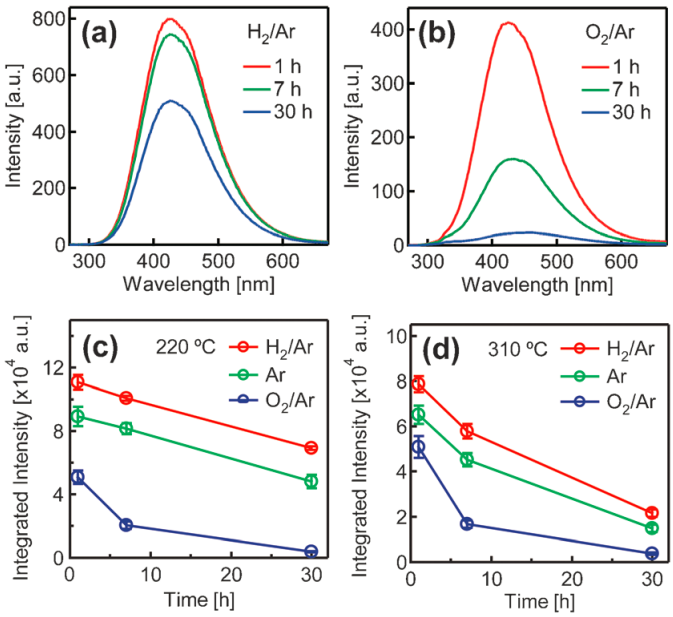

Figure 3.15 (a, b) PL spectra of Ga_2O_3 NCs prepared for different durations in H_2/Ar (a) and O_2/Ar mixtures (b). (c, d) Integrated PL intensity of colloidal Ga_2O_3 NCs as a function of synthesis time in different chemical environments at 220 ℃ (c), and 310 ℃ (d). The data correspond to the same NC concentrations.

The synthesis of Ga_2O_3 NCs for 1 h in a mildly reducing environment of H_2/Ar enhances the PL quantum yield by up to 15 %, while the synthesis in an oxidizing environment reduces it by over 40 %. The quantum yield of the NCs synthesized in H_2/Ar flow for 1 h is determined to be ca. 30 %. This value is among the highest reported quantum yields for TCO-NCs [10]. The decrease in PL intensity by oxidation is much larger than its increase by reduction, suggesting relatively high concentration of the oxygen vacancies in these NCs. Consequently, the saturation of the existing oxygen vacancies is more favourable than the formation of the new ones. The measured PL intensity after 30 h reaction in O_2/Ar is only 7.4 % of that after 1h. Similar results are obtained for NCs prepared at 310 ℃ (**Figure 3.15d**), confirming the same trends and establishing the dependence of PL on NC size, synthesis temperature and the chemical environment.

3.4 Conclusions

In this chapter we reported the first size-controlled synthesis of colloidal γ-Ga_2O_3 NCs and demonstrated size tunable PL from UV to blue. The NCs exhibit long lifetime phosphorescence arising from donor-acceptor pair recombination. The size controlled synthesis of colloidal γ-

Ga_2O_3 NCs enables the manipulation of their optical properties by tuning the interactions of localized defects. These defects are also responsible for electrical conductivity, and the ability to tune their optical properties is very promising for application in multifunctional optoelectronic materials and devices.

Also, we demonstrated *in situ* control of the native defect formation in colloidal NCs in solution, and chemical manipulation of the optical properties of NCs that are not subject to quantum size effects. We anticipate that stronger reducing agents, which can be used in higher concentrations under described conditions, could lead to further increase in NC emission. In a broader context, the results of this work suggest a possibility of introducing and manipulating new properties of colloidal NCs by solution-phase control of the formation of internal structural defects.

Chapter 4 Size-Dependent Electron Transfer and Trapping in Strongly Luminescent Colloidal Gallium Oxide Nanocrystals

4.1 Introduction

The interest in transparent conducting oxides (TCOs) partly stems from their transparency to visible light coupled with high electrical conductivity [1-5], size-dependent properties [6-9], chemical stability, and structural versatility [10-12]. Furthermore, these materials are largely environmentally benign, and can be prepared by simple solution- or gas-phase methods. Imparting new functional properties into TCO nanostructures can lead to improved understanding of the structure-property and property-property correlations in the solid state, and holds promise for the development of new technological applications [13-17]. One of the approaches to expanding the degrees of freedom in inorganic nanostructures is through the controlled formation and manipulation of defects. While incorporation of dopant ions into nanostructures has been a hotly pursued topic in the past decade [18,19], much less is understood about the formation of native defects and their role in defining and controlling functional properties. This is particularly true for colloidal nanocrystals (NCs) prepared by solution methods.

One of the ubiquitously important functionalities is the emission of light. Transparent materials combining high electrical conductivity and strong luminescence can be very promising for many technologies, including photonics, optoelectronics, and chemical and biological sensors. Photoluminescence (PL) of TCOs generally consists of a combination of the band edge emission (usually in UV) and a deep level emission (usually in the visible range) [9,20-22]. Deep level emission is characterized by a significant Stokes shift when TCOs are excited into the band gap and is associated with localized intra-band gap defect states [6,9,20-22]. Although PL of various colloidal TCO NCs has been measured, the quantum yields of these suspensions are usually relatively weak and/or difficult to control [9,21,22]. Gallium oxide has a band gap of ca. 4.9 eV and exists in five different allotropic modifications (α, β, γ, δ, and ε phases) [12,23]. Monoclinic β phase is stable at room temperature [12] and thus the investigations of the structure and optical properties of this TCO have mostly focused on β-Ga_2O_3 [24-30]. All other polymorphs have rarely been studied [6,12,23,31-33]. Metastable γ-Ga_2O_3 has a defective spinel structure (Fd3m) in which Ga^{3+} ions occupy octahedral and tetrahedral sites [23,32]. Unlike normal spinel-

structure stoichiometry (hypothetically, it should be Ga_3O_4), in γ-Ga_2O_3, among every 18 cationic sites, two sites are vacant in order to retain charge neutrality [32]. Previous studies have suggested that spinel γ-Ga_2O_3 type lattice contains vacancies on both cation and anion sites [34].

We have reported [6,35] the first synthesis of colloidal γ- Ga_2O_3 NCs with long lifetime size- and composition-tunable blue-green PL. This PL has been associated with the recombination of an electron bound to a donor, and a hole bound to an acceptor, and is known as the donor-acceptor pair (DAP) emission [36,37] (**Figure 4.1a**). Although the exact nature of the localized donor and acceptor sites has been debated over the years, it is widely considered that the donor is an oxygen vacancy (V_o^x), and the acceptor is a gallium-oxygen vacancy pair ((V_O, V_{Ga})^x) [25,27,28]. Upon the excitation of Ga_2O_3 NCs into the band gap, a hole on an acceptor and an electron on a donor are recreated, giving

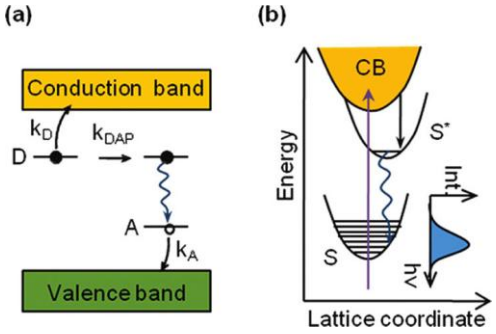

Figure 4.1 (a) Schematic representation of the DAP recombination mechanism, involving a transfer of an electron trapped on a donor (D) to an acceptor (A) site (k_{DAP}), at which the recombination occurs. Detrapping of an electron from a donor to the conduction band (k_D) and a hole from an acceptor to the valence band (k_A) is also indicated. (b) The configuration coordinate diagram showing the exciton recombination on an acceptor site, involving strong coupling to lattice vibrations. The equilibrium value of a lattice coordinate changes between the excited (S*) and ground states (S), leading to large wave function overlap for a transition to a high vibronic state and contributing to broadening of the PL band.

rise to the blue emission, according to the following equation:

$$(V_o, V_{Ga})^x + V_o^x \rightarrow (V_o, V_{Ga})' + V_o^{\blacksquare} + hv \qquad \textbf{(eq 4.1)}$$

The energy of the DAP emission can be calculated based on the Ga_2O_3 NC band gap energy (E_g), donor and acceptor binding (ionization) energies (E_D and E_A, respectively), and Coulombic attraction between the charged donor and acceptor sites using the following equation:

$$E = E_g - (E_D + E_A) + \frac{e^2}{4\pi\varepsilon r} \pm nE_{phonon} \qquad \textbf{(eq 4.2)}$$

Coulombic interaction term ($E_C = e^2/4\pi\varepsilon r$), which depends on the average separation (r) between donor and acceptor sites in NC lattice, has been identified as a possible origin of the size dependent PL energy and decay dynamics [6]. The blue PL band in Ga_2O_3 is broad and shows no discrete DAP lines, which is associated with a strong phonon coupling (**Figure 4.1b**) or a wide distribution of donor and acceptor states [36,38]. A detailed understanding of the mechanism of DAP recombination and the role of NC size and surfaces in defining PL properties could provide a guideline for manipulating PL in oxide nanostructures by engineering of native defects and their interactions.

In this chapter, I report the studies of the DAP recombination mechanism in colloidal γ-Ga_2O_3 NCs. The photoluminescence of a series of NC sizes was investigated at different temperatures (5-300 K) in steady-state and time-dependent modes. The NCs were also subjected to thermal and chemical treatments to examine the influence of the crystal structure, defect concentration, and surface modification on the PL efficiency and dynamics. The origin of the emission is confirmed to be the DAP recombination in both stable (β) and metastable (γ) phase, with the presence of vacancy defect sites and their separation playing a key role in determining the emission energy and decay. The binding energy of the donor and acceptor levels also shows size dependence, and increases with decreasing NC size. Importantly, the DAP PL can be effectively influenced by capping ligands on the NC surfaces. The competitive trapping of the photogenerated valence band holes by the acceptor sites and surface defects (OH-or O^{2-}) determines the quantum yield of the DAP recombination. The removal of the surface defect sites by dodecylamine and *tri-n*-octylphosphine oxide is shown to enhance the blue emission. The choice of the NC size and post-synthesis physical and chemical treatment can be used to control and enhance the blue DAP PL.

4.2 Experimental Section

4.2.1 Materials

All chemicals were used as received. Gallium acetylacetonate ($Ga(acac)_3$; 99.99 %) was purchased from Strem Chemicals, oleylamine (70 %) and *tri-n*-octylphosphine oxide (TOPO; 90 %) from Sigma-Aldrich, and 1-dodecylamine (DDA; 98 %) from Alfa Aesar.

4.2.2 Synthesis of Ga_2O_3 Nanocrystals

The detailed experimental procedure for the synthesis of γ-Ga_2O_3 NCs was described in one of our previous paper [6]. All reactions were carried out under argon protection. Nanocrystals having the average sizes of 3.3 ± 0.5, 4.2 ± 0.9, and 6.0 ± 1.0 nm were synthesized at 200, 220, and 310 ℃, respectively. In a typical synthesis $Ga(acac)_3$ (0.5 g) was mixed in a round bottom flask with oleylamine (7.0 g) and stirred under argon at ca. 80 ℃ until the precursor was fully dissolved. The solution was degassed and heated to a desired reaction temperature at the rate of ca. 3 ℃/min. The reaction mixture was subsequently refluxed at the final synthesis temperature for 1 h. The resulting suspension was cooled to room temperature, precipitated, and washed three times with ethanol. The obtained powders were added to molten TOPO and heated for 1 h at 90 ℃. The TOPO-capped NCs were then precipitated and washed with ethanol. The white powders were finally dispersed in hexane. To test the effect of NC surface structure on the PL properties, we performed the heating of NC powders in TOPO and DDA at 90 ℃ for different amounts of time (1, 2, 4, and 24 h) [39]. The obtained surface-capped NCs were precipitated with ethanol and dispersed in hexane.

The annealing of the samples was done in Lindberg heavy-duty box furnace in air. As-synthesized NC samples were split in four parts, three of which were annealed at different temperatures (500, 800, and 1200 ℃) for 2 h. One part was left untreated as a control.

4.2.3 Measurements and Data Analysis

Nanocrystals were characterized by powder X-ray diffraction (XRD), transmission electron microscopy (TEM), and optical absorption and FTIR spectroscopy. XRD patterns were collected with INEL powder diffractometer equipped with a position-sensitive detector, using monochromatic Cu $K_{\alpha 1}$ radiation. TEM imaging was performed with a JEOL-2010F microscope, operating at 200 kV. The specimens for TEM measurements were prepared by dropping dilute suspensions of colloidal NCs in toluene on copper grids with lacey Formvar/carbon support films (Ted Pella, Inc.). The absorption spectra were collected with a Varian Cary 5000 UV-vis-NIR spectrophotometer. For the direct comparison of PL intensities, the concentrations of colloidal samples were adjusted to exhibit absorption of 0.1 at 230 nm. The FTIR spectra were measured with Bruker Tensor 27 spectrometer. The sample powders were dried in a fume hood for 2 days before taking IR measurements. The same amounts of sample and KBr were used for the

preparation of the pallets for FTIR measurements.

PL spectra were recorded with a Varian Cary Eclipse fluorescence spectrometer. For time-dependent PL measurements, the samples were excited at 230 nm with a Xenon flash lamp and the emission intensity was recorded at the maximum of the PL band after different delay times. For variable temperature PL measurements the samples were deposited on high quality quartz substrates by drop-casting the colloidal suspensions of NCs in hexane. The substrates were then mounted in a liquid helium cryostat (Optistat CF, Oxford Instruments), which was placed in the PL spectrometer such that the excitation beam is oriented 45 degrees with respect to the substrate normal. We performed PL measurements in the temperature range from 5 to 300 K.

4.3 Results and Discussion

4.3.1 Sample characterization

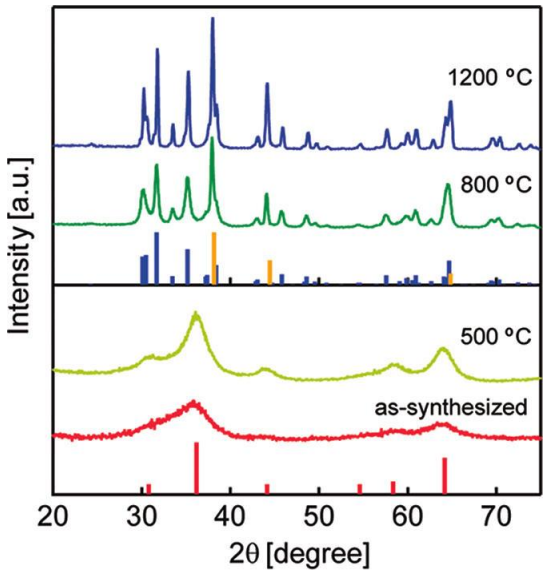

Figure 4.2 XRD patterns of Ga_2O_3 NCs, as-synthesized and upon annealing at different temperatures (as indicated in the graph). Vertical red and blue lines indicate the XRD patterns of bulk γ-Ga_2O_3 (JCPDS 20-0426) and β-Ga_2O_3 (JCPDS 43-1012), respectively. The peaks arising from the Al sample holder are indicated with vertical orange lines.

Figure 4.2 shows XRD patterns of Ga_2O_3 NCs synthesized at 220 ℃ upon annealing at different temperatures (500, 800, and 1200 ℃) for 2 h. The XRD pattern of originally

synthesized NCs (red trace) is well matched to that of γ-Ga_2O_3 having cubic crystal structure (vertical red lines, JCPDS 20-0426). These NCs have quasi spherical shape and uniform sizes, as previously documented. After annealing at 500 ℃ (olive trace) the XRD peaks become narrower and more pronounced, indicating an increase in the average NC size due to their aggregation and ripening. By annealing at 800 ℃ (green trace) the NCs undergo phase transformation to monoclinic β-Ga_2O_3 (vertical blue lines, JCPDS 43-1012), concurrently with a further increase in the grain sizes. It has been reported that nanostructured γ-Ga_2O_3 transforms into β-phase between 600 and 700 ℃ [40], which is in good agreement with our observation. The XRD pattern of NCs annealed at 1200 ℃ (blue trace) is fully resolved and essentially identical to that obtained for β-Ga_2O_3 bulk powder (**Figure 4.3**).

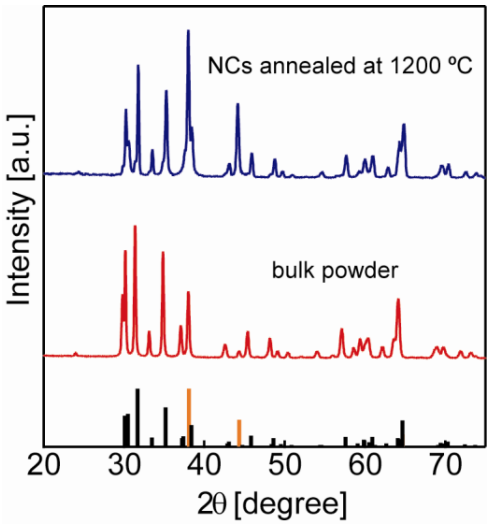

Figure 4.3 XRD patterns of commercial β-Ga_2O_3 powder (red trace) and typical γ- Ga_2O_3 NCs annealed at 1200 °C (blue trace). The vertical black lines represent the XRD pattern of bulk β-Ga_2O_3 (JCPDS 43-1012). The obtained XRD patterns are essentially identical and match the pattern of β-Ga_2O_3, indicating fusion and phase transformation of colloidal NCs from γ- to β-phase upon annealing at 1200 ℃. Vertical orange lines indicate contribution of the Al sample holder to the XRD patterns.

4.3.2 Photoluminescence Spectra of Annealed Samples

The PL spectra of the same samples are shown in **Figure 4.4**. As synthesized γ-Ga_2O_3 NCs exhibit a strong blue emission centered at ca. 430 nm, arising from the DAP recombination as described above. The intensity of this emission decreases, and the center of gravity shifts to ca. 465 nm upon annealing at 500 ℃. Both of these effects are consistent with a decrease in the

concentration of defects (donors and acceptors). A lower concentration of the gallium and oxygen vacancy sites leads to a smaller number of the donor-acceptor pairs (lower PL intensity) and a larger average separation between the recombining pairs (red shift of the PL band). Taken together, XRD and PL data indicate that thermal annealing of NCs causes a change in DAP recombination because of two factors: (i) decrease in the absolute number of defect sites and (ii) increase in the average NC size due to their ripening and fusion.

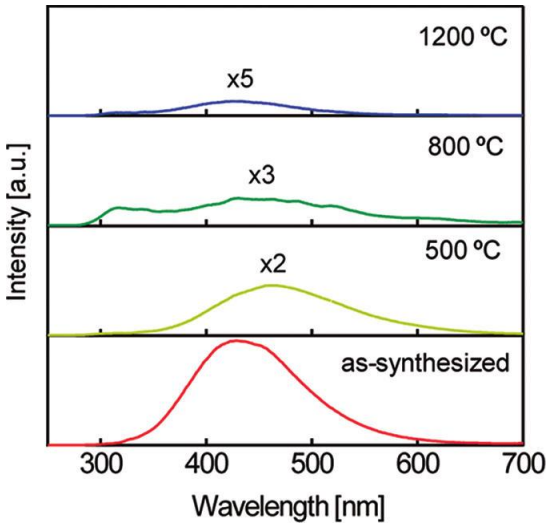

Figure 4.4 Photoluminescence spectra of Ga_2O_3 NCs, as-synthesized and upon annealing at different temperatures. The samples were excited into the band gap with 230 nm radiation. The spectra of annealed NCs are multiplied by different factors, as indicated in the graph, for clarity. The spectra correspond to the same NC concentrations based on the identical band edge absorbance.

At higher annealing temperatures PL is quenched further but experiences a blue shift with respect to the emission of NCs annealed at 500 ℃. The sample annealed at 1200 ℃ shows only a very week emission (ca. 1.5 % of the emission intensity of as-synthesized NCs) centered at 425 nm. This blue shift is opposite from the behavior expected for lower defect concentration in annealed samples, and can be associated with smaller donor and acceptor binding energies in β-Ga_2O_3 relative to γ-Ga_2O_3. This assumption was confirmed by collecting a PL spectrum of commercial β-Ga_2O_3 powder (**Figure 4.5**), which is also blue-shifted compared to γ-Ga_2O_3 NCs.

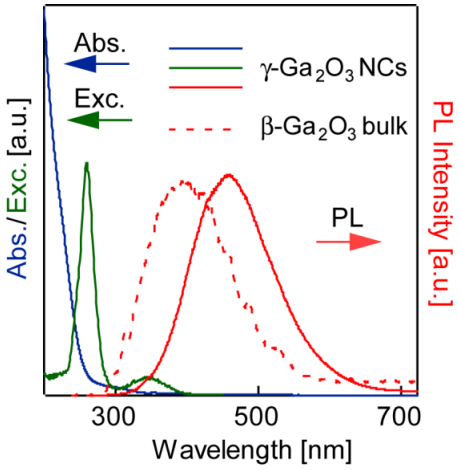

Figure 4.5 Comparison between the PL spectra of colloidal γ-Ga_2O_3 NCs (solid red line) and commercial β-Ga_2O_3 powder (dashed red line), showing a significant blue shift of the emission band of β-Ga_2O_3. The absorption (blue) and excitation (green) spectra of γ-Ga_2O_3 NCs are also shown.

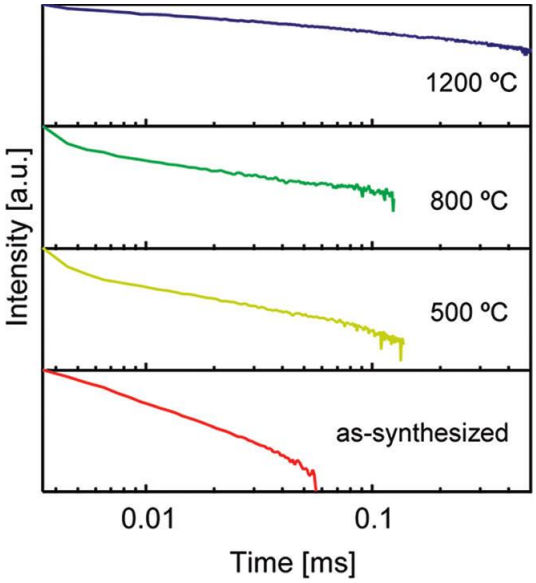

Figure 4.6 Time-resolved photoluminescence measurements of Ga_2O_3 NCs from Figure 4.4, measured at the maximum of the emission band.

Upon excitation into the band gap the DAP recombination occurs in two steps [27]. In the first step an electron transfers from a donor to a neutral acceptor site forming a trapped exciton. In the second step the exciton undergoes radiative recombination on the acceptor site. The rate

determining step of DAP recombination is the transfer of an electron trapped on a donor (often referred to as tunnel transfer) [27]. An increase in the average donor-acceptor separation induces a decrease in the PL decay rate, associated with a decreased probability of the electron capture by an acceptor site. The DAP PL decay has been quantitatively described by a kinetic model [37]. The PL intensity of the blue bands in **Figure 4.4** recorded at different times after the excitation at 230 nm is shown in **Figure 4.6**. The decay curves have a complex nonexponential form confirming that the electron capture by acceptors, rather than an exciton recombination, is the rate determining step. The PL decay rate decreases with increasing annealing temperature, with the emission half-life ranging from 4.6 μs for NCs annealed at 500 °C to 8.0 μs for NCs annealed at 1200 ℃. This decrease in the PL decay dynamics occurs in spite of the NC phase transformation and is directly related to a decrease in the point defect concentration and the donor-acceptor separation. The evolution of the PL properties with increasing annealing temperature is shown schematically in **Figure 4.7**. The annealing at low temperatures induces an increase in the average NC size along with a decrease in defect concentration. This leads to quenching of PL intensity and a decrease in the PL decay rate. By increasing the annealing temperature this trend continues, causing also a phase transformation, as evidenced by the blue shift of PL.

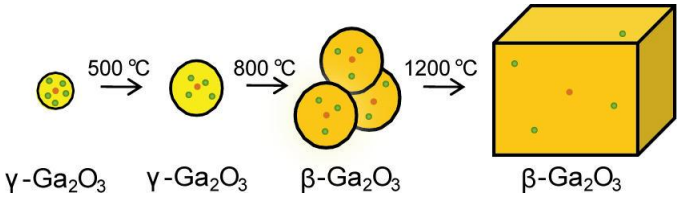

Figure 4.7 Schematic representation of the influence of annealing temperature on the NC ripening, aggregation, defect concentration, and the corresponding DAP emission properties. Green and orange dots indicate donor (majority) and acceptor (minority) sites, respectively.

4.3.3 Low Temperature Photoluminescence Measurements

To further investigate the mechanism of DAP recombination we measured the PL spectra of a series of colloidal NCs having different sizes in the temperature range from 5 to 300 K (**Figure 4.8**). **Figure 4.8a** shows the PL spectra of 6.0 nm diameter γ-Ga_2O_3 NCs. The PL intensity remains unchanged with temperature until ca. 90 K. As the temperature increases above this value, the PL intensity drops and the center of gravity shifts to lower energies. This behavior is

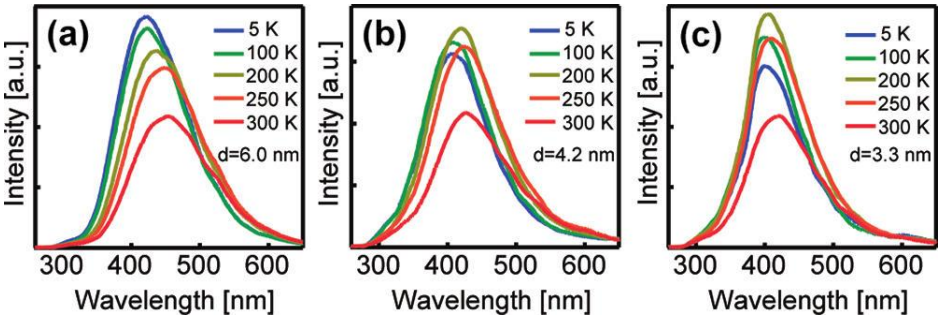

Figure 4.8 PL spectra of γ-Ga_2O_3 NCs having the average sizes of 6.0 ± 1.0 (a), 4.2 ± 0.9 (b), and 3.3 ± 0.5 nm (c) measured at different temperatures between 5 and 300 K, as indicated in the graphs.

distinctly different for smaller sized NCs (4.2 and 3.3 nm average diameter shown in **Figure 4.8**, panels b and c, respectively) for which the PL intensity initially increases with temperature up to ca. 200 K followed by a decrease at higher temperatures. The peak maxima for these samples shift to lower energies with temperature, similarly to NCs in **Figure 4.8a**, although to a lesser extent. The variable temperature PL results are plotted in **Figure 4.9**.The shift in the blue emission energy with temperature (**Figure 4.9a**) follows the Varshni law, typical for the band gap energy behavior:

$$E_{DAP}(T) = E_{DAP}(0) + \frac{\alpha T^2}{\beta + T} \qquad \textbf{(eq 4.3)}$$

where $E_{DAP}(T)$ and $E_{DAP}(0)$ are the DAP emission energies at temperature T and 0 K, respectively, and α and β are constants characteristic for a given semiconductor. For the fixed β value (β = 580 K) [41] $E_{DAP}(0)$ obtained as the fitting parameter ranges from 2.97 eV (for 6.0 nm diameter NCs) to 3.11 (for 3.0 nm diameter NCs). This variation suggests the difference in the smallest separation between a donor and an acceptor in NCs of different sizes and/or the dependence of the E_D and E_A values on the NC size.

The integrated PL intensity of 6.0 nm NCs (**Figure 4.9b**, red squares) can be readily fit to the expression for thermal quenching of DAP emission:

$$I(T) = \frac{I_0}{1 + A e^{\frac{-\Delta E}{kT}}} \qquad \textbf{(eq 4.4)}$$

where I(T) is the PL intensity at a given temperature T, ΔE is the activation energy, and A is a the pre-exponential factor. The PL intensities of 4.2 and 3.3 nm NCs (green and blue squares in

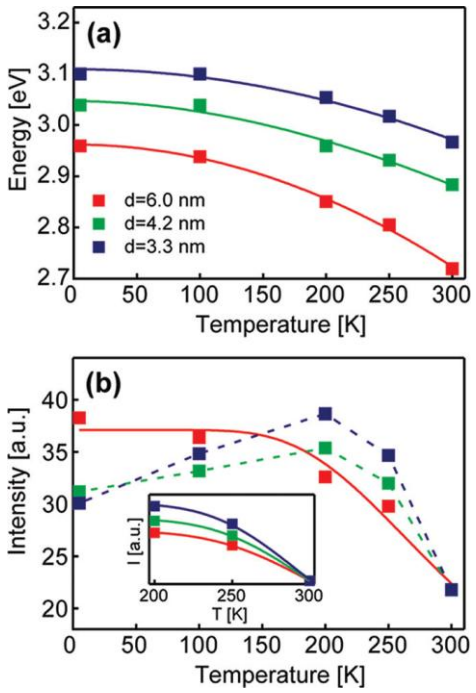

Figure 4.9 Temperature dependence of the maximum energy (a) and relative intensity (b) of PL of colloidal γ-Ga_2O_3 NCs having the average sizes of 6.0 ± 1.0 (red), 4.2 ± 0.9 (green), and 3.3 ± 0.5 nm (blue). The solid lines in (a) are fits to eq 4.3, yielding the $E_{DAP}(0)$ values of 2.97, 3.05, and 3.11 eV for 6.0, 4.2, and 3.3 nmNCs, respectively. The red line in (b) is the fit to eq 4.4 for 6.0 nm Ga_2O_3 NCs. Inset in (b) shows the same fits in the range 200-300K for all three NC sizes; the fitting parameters are given in Table 4.1.

Table 4.1 Parameters Obtained by Fitting the PL Intensity *vs* Temperature Data to eq 4.4 for Different NC Sizes.

nanocrystal size [nm]	I_0 [a.u.]	A [a.u.]	ΔE [mev]
6.0	32.92	1443.8	204.94 ± 0.02
4.2	35.66	3457.8	221.80 ± 0.02
3.3	38.95	8120.4	238.41 ± 0.02

Figure 4.9b, respectively) are well fit to the same function in the temperature range 200-300 K (inset).

The fitting parameters obtained for this range for all three NC sizes are shown in **Table 4.1**. The activation energy in the studied temperature range increases slightly with decreasing NC size, suggesting a larger donor trap depth (donor binding energy) [27] for smaller NCs. In the absence

of quantum confinement in Ga_2O_3 NCs in the studied size range, the increase in binding energy of the donor states (E_D) can be associated with a reduction in the dielectric constant and an increase in induced charge polarization at the interface between a NC and the surrounding solvent with decreasing NC size [42,43]. Both of these phenomena are general and interface related, indicating the proximity of the oxygen vacancy sites to NC surfaces. At temperatures below 200 K, however, the results for PL intensity for 4.2 and 3.3 nm NCs significantly deviate from those for 6.0 nm NCs. The PL intensity increases with temperature forming a maximum at ca. 200 K. This increase becomes more pronounced with decreasing NC size, suggesting that it could also result from stronger electron binding to the donor sites in smaller NCs. To illustrate this hypothesis consider a schematics of the mechanism of electron trapping in Ga_2O_3 NCs shown in **Figure 4.1a**. At room temperature the shallow donor sites can be easily ionized in NCs of all sizes, causing the presence of free electrons in the conduction band (k_D in **Figure 4.1a**)

$$V_o^x \rightarrow V_o^{\blacksquare} + e_{CB}^- \qquad \textbf{(eq 4.5)}$$

The activation energy of this process is approximately equal to the binding energy of a donor ($\Delta E \approx E_D$). Similarly, detrapping of a hole from a localized acceptor to the valence band (k_A in **Figure 4.1a**) occurs by:

$$(V_o, V_{Ga})^x \rightarrow (V_o, V_{Ga})^{'} + h_{VB}^+ \qquad \textbf{(eq 4.6)}$$

This process has higher activation energy due to the larger binding energy of a hole on the acceptor [27]. As the temperature decreases an electron promoted from the valence to the conduction band gets trapped in a localized donor state. Subsequently this electron in captured by an acceptor site (k_{DAP}), followed by a recombination with a trapped hole. Trapping an electron on a donor (reverse of k_D) is the fast step [27], and the PL intensity for larger NCs (6.0 nm diameter) increases with decreasing temperature until saturation of the donor sites. As the NC sizes are reduced, the electrons become more strongly bound to the donors (vide supra). Consequently, a barrier for the electron capture by an acceptor site becomes greater, gradually decreasing the efficiency of the DAP recombination below 200 K. These results also imply that, in the context of the Bohr model [44], the Bohr radius of the donor decreases with decreasing NC size, which can be associated with the influence of the dielectric discontinuity on the defect sites, as mentioned above.

To address the mechanism of DAP recombination and the role of surface termination in this

process we studied the PL properties of surface-modified γ-Ga_2O_3 NCs. The PL spectra of NCs treated in DDA for 1, 2, 4, and 24 h are shown in **Figure 4.10a**. With a prolonged heating of NCs in DDA, the luminescence increases, but the emission band does not shift, indicating that this mild temperature is not sufficient to anneal the existing defects.

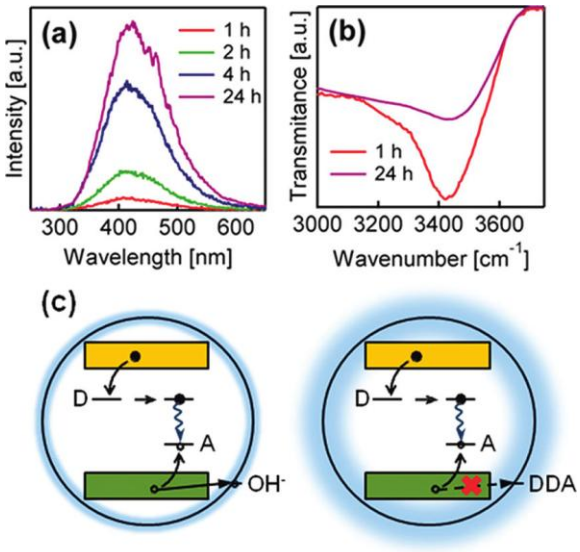

Figure 4.10 (a) Photoluminescence spectra of colloidal 4.2 nm γ-Ga_2O_3 NCs heated in DDA at 90 ℃for 1, 2, 4, and 24 h. (b) FTIR spectra of the same NCs after DDA treatment for 1 and 24 h. The IR band is assigned to the OH- stretching mode. (c) Schematic representation of the hole trapping pathways before (left) and after (right) NC capping with DDA. DDA removes OH- groups from the NC surfaces, allowing for trapping of a hole from the valence band to an acceptor site and leading to an increase in the PL intensity.

Concurrently with an increase in the PL intensity due to DDA capping, a decrease in the OH- concentration on the NC surfaces is observed in the FTIR spectra (**Figure 4.10b**). This behavior is in stark contrast with ZnO NCs for which the green emission decreases with higher surface concentration of DDA [22]. The proposed mechanism of visible emission in ZnO NCs involves transfer of a photogenerated hole in the valence band to a deep hole trap within the NC band gap, which is suggested to be an oxygen vacancy site with a single positive charge ($V_o^{\cdot}$) [9,45]. This process involves initial hole transfer from the valence band to a localized surface defect site (likely OH- or O^{2-}) [9,22]. Efficient capping of the NCs removes the surface hole traps and quenches the green emission. In the case of colloidal Ga_2O_3 NCs a photogenerated hole in the valence band is directly trapped by an acceptor site where it undergoes a recombination with an

electron transferred from a donor. Trapping of the valence band holes by surface defects competes with their capture by the acceptor sites, which quenches the DAP emission (**Figure 4.10c**) [46]. Successive removal of surface defect sites (particularly OH-) by capping with DDA eliminates this trapping channel, allowing for an efficient capture of the valence band holes by the acceptor sites and enhancing the intensity of the DAP emission. Incidentally, we find that TOPO ligands are more readily bound to Ga_2O_3 NC surfaces than DDA, as evidenced by the stronger emission under identical conditions (**Figure 4.11**). The IR spectra of differently treated NCs clearly indicate the different surface modification (DDA and TOPO, **Figure 4.12**). These results demonstrate another approach to effectively impact the defect interactions in colloidal Ga_2O_3 NCs via external NC modification and surface chemistry.

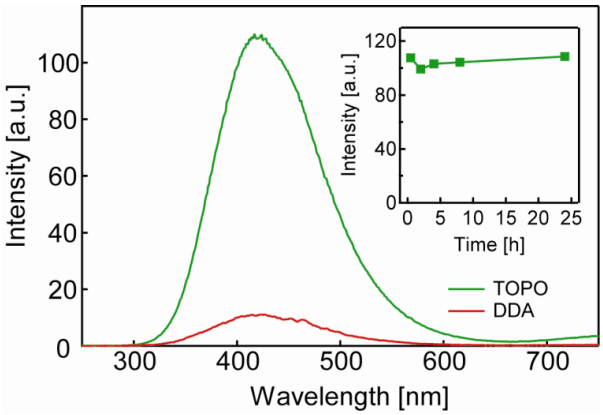

Figure 4.11 Photoluminescence spectra 4.2 nm γ-Ga_2O_3 NCs heated for 24 hours in TOPO (green trace) and DDA (red trace). Inset: PL intensity of TOPO-capped NCs as a function heating time in molten TOPO. The PL intensity remains similar in this time range, indicating that most accessible OH- groups were replaced within the first hour. These results suggest higher binding affinity of TOPO relative to DDA molecules.

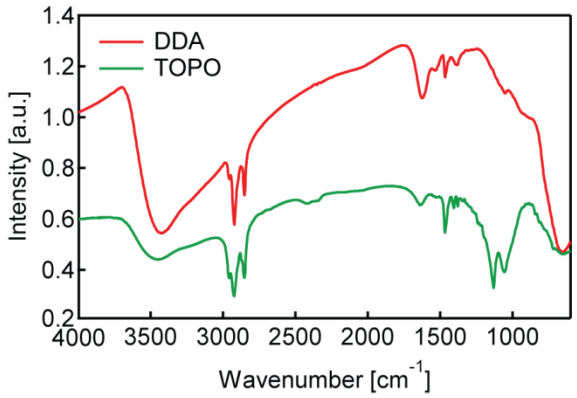

Figure 4.12 IR spectra of the same NCs after DDA treatment (red line) and TOPO treatment

(green line).

4.4 Conclusions

We investigated the PL mechanism of colloidal Ga_2O_3 NCs and the effect of NC size, structure, and surface modification on its efficiency and dynamics. This emission arises from DAP recombination and is sensitive to the NC phase, which determines the localized donor and acceptor binding energies, and the defect concentration, which determines their interactions. The increased separation between donor and acceptor sites increases the lifetime of the DAP emission. The temperature dependent PL studies suggest that the donor binding energy increases with decreasing NC size, owing to the reduction in the dielectric constant and/or an increase in induced polarization at the NC surfaces. The emission of γ-Ga_2O_3 NCs is therefore a complex interplay between the binding energies and interactions of the defect sites, both of which are size dependent. The hole traps on the NC surfaces (surface defects) compete with the acceptor sites for the photogenerated valence band holes, reducing the DAP recombination. Removal of the hole trapping pathways on NC surfaces enhances the blue emission from DAP recombination. Understanding this mechanism allows for manipulation of the DAP recombination by NC surface modification. The colloidal suspensions of Ga_2O_3 NCs are stable in air over a very long period of time (we have not noticed any changes for several months during the course of this work) and have remarkable PL efficiency (ca. 25%, since the emission intensity is very low, for TCOs defect emission we didn't find any reports on the quantum yields), making them excellent candidates for potential applications as LEDs, sensors, and UV photodetectors.

Chapter 5 Dynamically-Tunable Photoluminescence Chromaticity in Colloidal Lanthanide-Doped Ga_2O_3 Nanocrystals

5.1 Introduction

Luminescent colloidal nanocrystals have found a wide range of potential applications in photonic [1-3], optoelectronic [4-6], and biomedical [7] technologies. The development of colloidal nanocrystal systems with novel and tunable luminescence properties is therefore of significant current interest. Trivalent lanthanide ions (Ln^{3+}) have unique spectroscopic features originating from intra-4f transitions. The 4f electrons of Ln^{3+} ions are well shielded by fully occupied outer orbitals, making f-f transitions largely insensitive to the surrounding chemical environment. The resulting photoluminescence spectra are sharp, long lived (usually on the order of milliseconds), and resistant to photobleaching and photodegradation. These characteristics render Ln^{3+} ions indispensable for the fabrication of optical amplifiers for telecommunication, laser gain media, and a variety of phosphors, which has triggered vigorous research on the doping and properties of Ln^{3+} ions in solid state materials [8-15]. More recently, Ln^{3+} ions have also attracted much attention as luminescent probes in biological assays [16-18], because of their stability and their long lifetime PL which can be easily distinguished from the short-lived background fluorescence. Compared to organic fluorophores, lanthanide-based bioprobes have significantly improved detection sensitivity and selectivity, and are often employed in drug monitoring, biosensing and bioimaging [19]. However, an inherent limitation of Ln^{3+} ions in most optical applicationsis that f-f transitions are parity (Laporte) forbidden, resulting in very small extinction coefficients [20]. Furthermore, the luminescence of the excited Ln^{3+} ions can be readily quenched by non-radiative energy transfer to high frequency vibrations (i.e. O-H and N-H) in protic solvents [21,22]. A possible way to overcome these limitations is through the sensitization effect - excitation of Ln^{3+} ions by energy transfer from the coordinating species having large absorption cross section [19,23]. Semiconductor NCs exhibit strong valence-to-conduction band electronic absorption, and can effectively sensitize and protect substitutionally-incorporated Ln^{3+} luminescence. Furthermore, semiconductor NCs have a range of size-tunable optical and electronic properties. Thus, incorporation of targeted Ln^{3+} ions into semiconductor

NC host lattices represents an attractive approach to sensitize Ln^{3+} centers and obtain complex multifunctional colloidal NCs.

Previous reports have indicated that different (semiconductor) NCs, including II-VI (such as CdS, CdSe, ZnS, and ZnO) [24-27], TiO_2 [28-30], and In_2O_3 [31,32]NCs are effective host materials for the sensitization of Ln^{3+} emission. In all of these cases an enhancement of the Ln^{3+} emission intensity has been observed upon excitation of the NC host lattice, relative to the direct excitation of Ln^{3+} 4f electrons. The origin of this sensitization process and how to control it is still not fully understood. Furthermore, these host NCs are either non-emissive or have much shorter lifetime than Ln^{3+} ions (nanosecond to microsecond range), preventing the interactions between the emission properties of the Ln^{3+} dopants and the NC host lattice, and the tunability of the PL properties through the dual emission at the same timescale. Solution-phase incorporation of the Ln^{3+} dopants into a selected NC host lattice which can both strongly sensitize the Ln^{3+} emission and lead to the new properties in combination with Ln^{3+} luminescence is a challenging task which could improve the existing applications and lead to new yet unforeseen ones. It has been suggested that the host lattice defect states play a key role in the Ln^{3+} sensitization by trapping the excitons and non-radiative energy transfer to the Ln^{3+} ions [11,29]. Hence, the ability to control native defects in Ln^{3+}-doped NCs can have a significant consequence on the efficiency of the Ln^{3+} emission and the possibility of modulating the optical properties of these complex NCs. Starting from that hypothesis, we seek here to develop the colloidal Ln^{3+}-doped semiconductor NCs in which the long lifetime host lattice luminescence originates from native defect states that can be formed and manipulated *in situ* during sample preparation.

Gallium oxide (Ga_2O_3) is a wide band gap (~ 4.9eV) semiconductor with promising applications as a catalyst (for example, surface binding with metal catalysts), in gas sensors and in light emitting devices [33,34]. Due to its chemical and thermal stability, and optical transparency, Ga_2O_3 may also act as a good host lattice for efficient Ln^{3+} sensitization. Recently, successful incorporation of Ln^{3+} ions into β–phase Ga_2O_3 crystal lattice upon high-temperature (> 1000 ℃) annealing of as-prepared samples has been reported [35-37]. Some of these studies have demonstrated the sensitization of lanthanide dopants by the β–Ga_2O_3 host lattice. Doping rare earth ions into other polymorphs of Ga_2O_3 (α, γ, δ, ε) have not been investigated. Furthermore, there has been no report of the preparation and properties of truly colloidal Ln^{3+}-

doped Ga_2O_3 NCs, which can be of interest for light emitting devices, displays and bio-analysis. We have recently reported the size-controlled synthesis of colloidal γ-Ga_2O_3 NCs [38]. The synthesized γ-Ga_2O_3 NCs show strong size-tunable blue-green emission with high quantum yield (~ 25%) and lifetime in micro-to-millisecond regime. This blue PL has been attributed to the radiative recombination of donor-acceptor pairs (DAPs) formed by the native structural defects [39-41].

In this chapter, I report the synthesis and optical properties of Eu^{3+}-doped γ-Ga_2O_3 NCs. Time-gated PL measurements reveal distinct emission of Eu^{3+} centers upon excitation of NCs into the band gap, indicating exceptionally strong sensitization of Eu^{3+} by the NC host lattice. This Eu^{3+} sensitization is enabled by energy transfer, which likely involves the NC native defect (donor and acceptor) states. The Eu^{3+} emission originating from intra-4f transitions coexists with the broad-band DAP luminescence, but Eu^{3+} red emission has somewhat slower decay rate (lifetime of tens of milliseconds) than the defect-related DAP blue-green emission. The blue-to-red emission intensity ratio can be tuned either by adjusting the dopant concentration, or by changing the excitation delay time and PL gate time. These phenomena allow for dynamic modulation of the PL chromaticity on the millisecond timescale. The generality of these findings was demonstrated by Tb^{3+} doping, indicating the potential of colloidal Ln^{3+}-doped Ga_2O_3 NCs in multiplexed signaling and complex phosphors. Furthermore, the dynamically-tunable dual emission demonstrated in this work may have a potential application in biosensing and bioimaging processes involving microsecond timing, and in time-sensitive photonic devices.

5.2 Experimental Section

5.2.1 Materials

All reagents and solvents are commercially available and were used as received. Gallium acetylacetonate ($Ga(acac)_3$, 99.99 %), $EuCl_3$ (99.9 % Eu), and $TbCl_3$ $6H_2O$(99.9 % Tb) were purchased from Strem Chemicals. Oleylamine (70 %) and tri-*n*-octylphosphine oxide (TOPO, 90 %) were purchased from Sigma-Aldrich Company. Hexane (99.9 %) and ethanol were obtained from Fischer Scientific.

5.2.2 Synthesis of Eu-Doped γ-Ga_2O_3 NCs

The synthesis of Ln^{3+}-doped γ-Ga_2O_3 NCs was based on the previously reported procedure for the synthesis of pure γ-Ga_2O_3 NCs [38]. All syntheses were performed in the argon atmosphere. In a 100 ml three-neck round bottom flask 0.5 g of $Ga(acac)_3$, 7.2 g of oleylamine, and varying amounts of $EuCl_3$ or $TbCl_3$ (from 0.1-10 mol% relative to Ga) were mixed in the flow of argon. The mixture was degassed and heated to 310 ℃, and the reaction was allowed to proceed for 1 hour while continuously stirring. The reaction mixture was then gradually cooled to room temperature, and Ln^{3+}-doped γ-Ga_2O_3 NCs were isolated as powders by precipitation with 20 ml of ethanol and centrifugation at 3000 rpm for 15 minutes. All NC precipitates were heated in melted TOPO, followed by precipitation with ethanol. This procedure was repeated three times to ensure the removal of surface-bound dopant ions [47]. The obtained NCs were dispersed in hexane, giving a completely transparent colloidal suspensions.

5.2.3 Measurements and Data Analysis

Nanocrystals were characterized by powder X-ray diffraction (XRD), transmission electron microscopy (TEM), and optical absorption. XRD patterns were collected with INEL powder diffractometer equipped with a position-sensitive detector, using monochromatic Cu $K_{\alpha 1}$ radiation. TEM imaging was performed with a JEOL-2010F microscope operating at 200 kV. The specimens were prepared by dropping dilute suspensions of colloidal NCs in toluene on copper grids with lacey formvar/carbon support films purchased from Ted Pella, Inc. The absorption spectra were collected with a Varian Cary 5000 UV-vis-NIR spectrophotometer. To make all sample photoluminescence measurements comparable, the UV spectra of all colloidal samples were taken and the concentration was adjusted to achieve an intensity of 0.1 (at 230 nm) before taking photoluminescence measurements. Luminescence life time measurements were performed using a Varian Cary Eclipse fluorescence spectrometer.

Steady state and time resolved luminescence measurements were recorded with a Varian Cary Eclipse fluorescence spectrometer excited at 230 nm with a pulsed Xenon flash lamp. All measurements were done at room temperature using a 1 cm path length quartz cuvette. Steady state luminescence spectra were recorded using the fluorescence mode of the equipment. Time resolved luminescence made use of the phosphorescence mode with both the excitation and

emission slit (bandpass) set as 10 nm, without specification, the time resolved spectra were acquired with a delay time of 0.1 ms and a gate time of 5 ms.

5.3 Results and Discussion

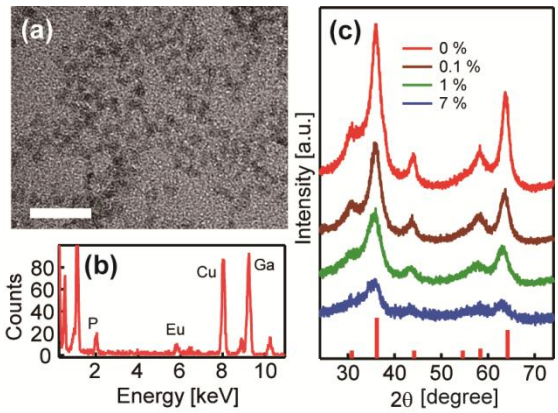

Figure 5.1 (a) Overview TEM image of 7 mol% Eu^{3+}-doped Ga_2O_3 NCs (scale bar, 20 nm). (b) Typical EDX spectrum of NC shown in (a). The average Eu^{3+} content (7 mol %) was determined from the EDX spectra collected for several different areas of the specimen. (c)XRD patterns of undoped and Eu^{3+}-doped γ-Ga_2O_3 NCs. The doping concentrations are indicated in the graph. Vertical red lines represent XRD pattern of bulk γ-Ga_2O_3 (JCPDS No. 20-0426).

The samples of colloidal Eu^{3+}-doped γ-Ga_2O_3 NCs having different doping concentrations were prepared by adapting the procedure for the synthesis of undoped Ga_2O_3 NCs. Transmission electron microscopy (TEM) image of typical Eu^{3+}-doped γ-Ga_2O_3 NCs is shown in **Figure 5.1a**. Elemental analysis performed using the energy dispersive X-ray (EDX) spectrum (**Figure 5.1b**) indicates that the doping concentration of these NCs is 5.2±0.2 mol%. This concentration is nearly identical to the starting precursor Eu^{3+} concentration in the reaction mixture (5 mol%), indicating quantitative incorporation of the dopant ions. Similar observations were made for other doping concentrations in the low Eu^{3+} precursor concentration regime (below 5 mol%), which were detectable by EDX. Increased concentration of the dopant precursor in the reaction mixture leads to a decrease in the average size of the obtained NCs (**Figure 5.2**). This observation is fully consistent with now well-understood phenomena of the suppression of the NC nucleation and grown in the presence of dopant impurities in the reaction mixture [42,43]. This inhibition of growth is associated with an increase in the activation barrier to the NC growth by the surface-bound impurity species. The average NC size changes from 6.1 ± 0.8 nm for undoped NCs to 3.5

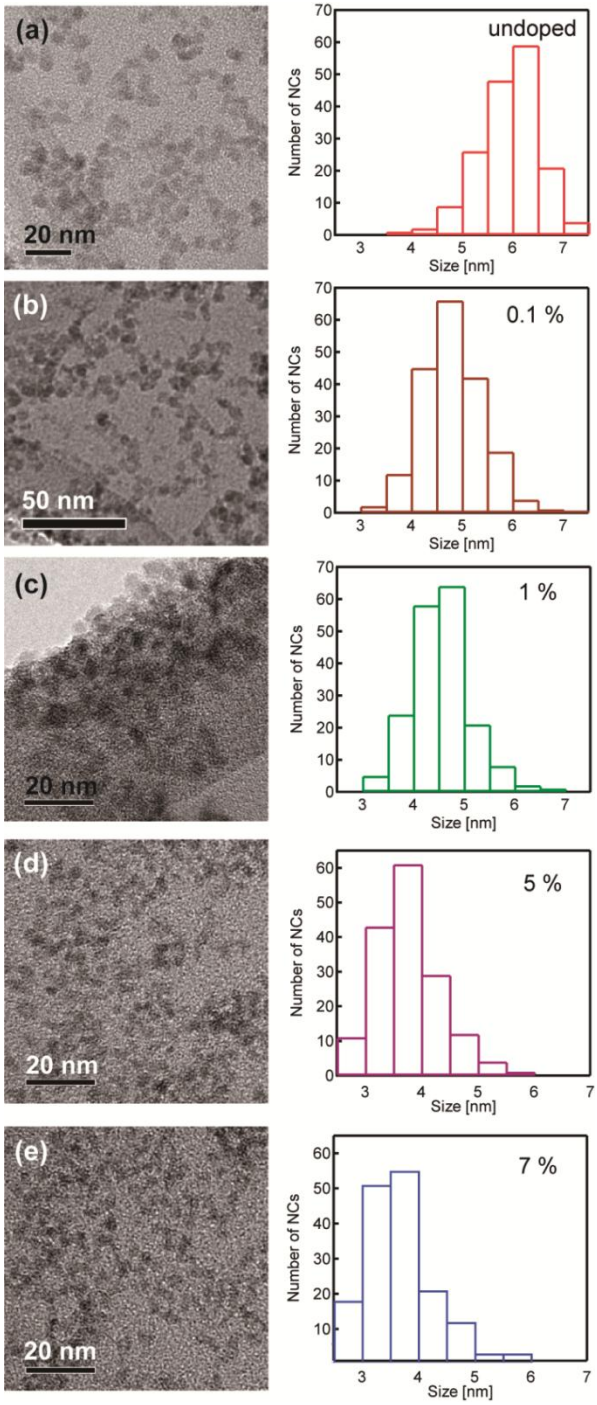

Figure 5.2 TEM images (left) and size distribution histograms (right) of Eu^{3+}-doped Ga_2O_3 NCs, with an average Eu^{3+} doping concentration of: (a) 0 mol% (undoped), (b) 0.1 mol%, (c) 1 mol%, (d) 5 mol%, and (e) 7 mol%. Average sizes of the NCs were (a) 6.1 ± 0.8 nm. (b) 4.8 ± 0.7 nm. (c) 4.5 ± 0.7 nm. (d) 3.8 ± 0.8 nm. (e) 3.5 ±0.7 nm.

± 0.7 nm for NCs prepared with the starting Eu^{3+} concentration of 10 mol%. X-ray diffraction patterns (**Figure 5.1c**) confirmed that all Eu^{3+}-doped Ga_2O_3 NC samples have γ-phase Ga_2O_3 cubic crystal structure (JCPDS No. 20-0426). Increased broadening of XRD peaks with increasing doping concentration is consistent with a decrease in the average NC size.

Figure 5.3a compares steady-state (blue) and time-gated (red) PL spectra of 1 mol% Eu^{3+}-doped γ-Ga_2O_3 NCs upon the excitation at 230 nm, above the band gap energy of Ga_2O_3 NCs. The steady-state PL spectrum is dominated by a broad PL band centered at ca. 400 nm, which corresponds to the γ-Ga_2O_3 NC host lattice DAP emission. Time-gated spectrum was collected 0.1 ms upon the excitation, with 5 ms gate time. After 0.1 ms delay the DAP emission is nearly completely decayed, and the spectrum consists only of the characteristic Eu^{3+} emission pattern. The four relatively narrow emission peaks with the maxima at 594, 615, 656, and 708 nm can be assigned to Eu^{3+} $^5D_0 \rightarrow {}^7F_{1,2,3,4}$ intra-4f transitions, respectively. At high doping concentrations (≥ 5 mol%) both DAP and Eu^{3+} emissions are observed in the steady-state spectrum, because the intensity of the Eu^{3+} emission becomes sufficiently high, while the DAP emission is significantly quenched (**Figure 5.4**). These data indicate that DAP emission has much higher intensity and a faster decay rate than the Eu^{3+} emission. Furthermore, the observation of the Eu^{3+} emission by NC band gap excitation suggests internal Eu^{3+} doping, and its sensitization and protection by the NC host lattice. **Figure 5.3b** shows the steady-state (blue trace) and time-gated (red trace) excitation spectra of 1 mol% Eu^{3+}-doped γ-Ga_2O_3 NCs from **Figure 5.3a**, recorded for the emission at 400 nm (DAP) and 615 nm ($^5D_0 \rightarrow {}^7F_2$), respectively, together with the absorption spectrum (black trace) of the same NCs. The steady-state and time-gated excitation spectra are identical, showing only a rather sharp deep-UV band, which coincides with the absorption edge of Ga_2O_3 NCs [38,40], and can be attributed to the band edge excitation. This result unambiguously confirms the sensitization of the Eu^{3+} dopants by the host NC lattice. No time-gated emission was detected by direct excitation of Eu^{3+} ions (i.e. at 395 nm, based on a typical Eu^{3+} absorption spectrum; **Figure 5.5**) owing to the low absorption cross section of Eu^{3+} f-f transitions, underscoring the necessity of external sensitization by the NC electronic band structure.

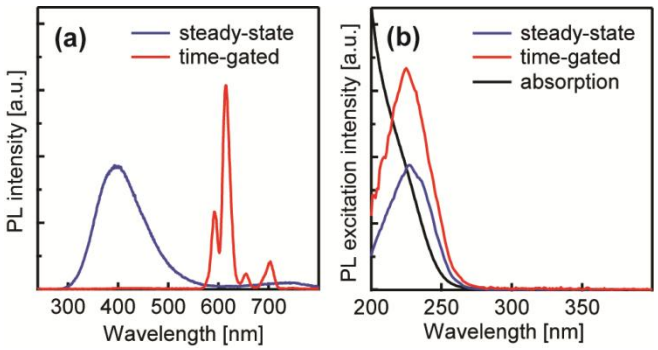

Figure 5.3 (a) Steady-state (blue) and time-gated (red) PL spectra of 1 mol% Eu^{3+}-doped Ga_2O_3 NCs (λ_{exc}=230 nm). (b) Excitation spectra corresponding to the PL spectra in (a), shown with analogous colors, and absorption spectrum of the same sample (black). For steady-state PL spectrum λ_{em}=400 nm, and for time-gated spectrum λ_{em}=615 nm. Time-gated spectra in (a) and (b) were collected with a delay time of 0.1 ms and gate-time of 5 ms.

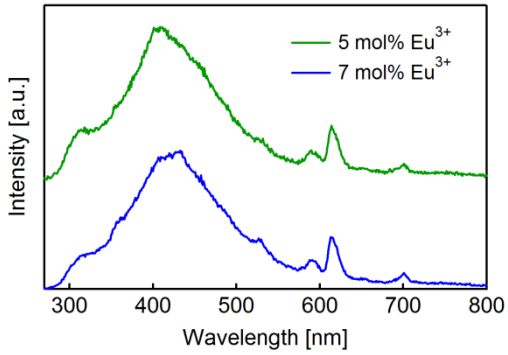

Figure 5.4 Steady-state PL spectra of highly Eu^{3+}-doped (5 and 7 mol %) Ga_2O_3 NCs. Eu^{3+} intra-4f transitions are readily observed even in steady-state spectra.

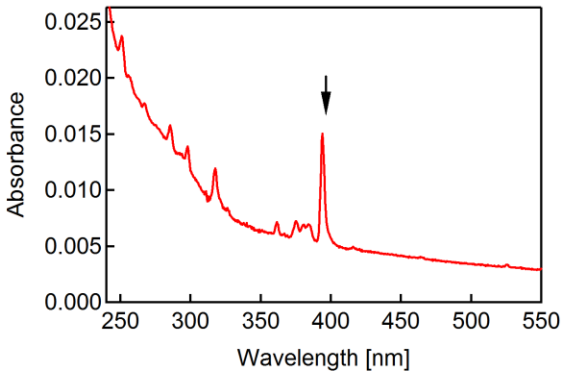

Figure 5.5 Typical electronic absorption spectrum of Eu^{3+} in an aqueous solution. The arrow indicates the peak used for direct excitation of Eu^{3+}.

The analogous spectroscopic measurements were performed for other NC samples containing various amounts of Eu^{3+}dopants. **Figure 5.6a** shows steady-state PL spectra of Eu^{3+}-doped Ga_2O_3 NCs, with doping concentrations ranging from 0 to 0.6 mol%. The concentration of NCs in all measured samples was identical, as determined from their absorption spectra. The PL spectra are qualitatively the same as that shown in **Figure 5.3a**, although a decrease in intensity and a blue shift of the DAP emission is observed with increasing doping concentration. Specifically, for the doping concentration of only 0.6 mol%, the emission intensity drops by about 85 % relative to undoped NCs, and the DAP PL band maximum blue shifts from ca. 450 nm to 420 nm. These observations can be rationalized in the context of our previous results on the origin of size-dependent DAP emission in colloidal γ-Ga_2O_3 NCs [39,41]. The energy of the DAP emission depends on the binding energy of the NC defect sites acting as donors acceptors, and the Coulombic interactions between them. An increase in the Coulombic interactions caused by a decrease in the average separation between donors and acceptors leads to a blue shift in the DAP emission band. We have previously shown that a decrease in NC size leads to a reduction in the average separation between donors and acceptors. As shown in **Figures 5.1b** and **Figure5.2** an increase in the initial Eu^{3+} concentration is accompanied by a decrease in NC size, and therefore the separation between donors and acceptors. However, in contrast to undoped NCs, the DAP emission intensity of Eu^{3+}-doped NCs decreases with decreasing NC size and increasing doping concentration. This decrease in intensity is associated with the energy transfer from the host NCs to the Eu^{3+} ions, which leads to quenching of the DAP emission. The energy transfer to Eu^{3+} and simultaneous quenching of DAP emission as a function of increasing doping concentration was further studied by time-gated PL spectroscopy. **Figure 5.6b** shows time-gated PL spectra of Eu^{3+}-doped Ga_2O_3 NCs, corresponding to the steady-state spectra shown in **Figure 5.6a**. All spectra were recorded with the delay time of 0.1 ms. As expected, with increasing doping concentration the intensity of the Eu^{3+} emission increases at the expense of the DAP emission. Compared to the steady-state spectra, the DAP PL bands are red-shifted and exhibit the maxima at similar wavelength (ca. 460 nm). This red shift arises from the donor-acceptor distance dependent rate of the DAP recombination, which relies on the electron transfer from a donor to an acceptor site as the rate determining step. Consequently, the pairs with a shorter separation recombine faster, and after a certain delay time only more distant pairs with smaller Coulombic interactions contribute to the observed emission. The DAP PL bands in the delay spectra narrow down on the high

energy (short wavelength) side and effectively shift to lower energies. Growing evidence has suggested that defect states may play a key role in the energy transfer between the host lattice and Ln^{3+} dopant ions. Moreover, Clabau et al [44,45] have suggested that a difference in the ionization potential or electronegativity between dopant and host cations in the same oxidation state can cause a non-random distribution of the host lattice anion vacancy sites relative to the dopant ions. This model proposes that a dopant ion with lower ionization potential than the host lattice cation can more effectively delocalize its electron density to an empty anion vacancy level, thus attracting and stabilizing an anion vacancy. In this work Eu^{3+} ion has significantly lower ionization potential than Ga^{3+} due to its larger size, and is expected to attract oxygen vacancies, which act as the shallow donor states. The proximity of the donor states to the Eu^{3+} dopants could explain an effective energy transfer to Eu^{3+} and sensitization of the Eu^{3+} emission. The mechanistic details involved and a possible role of defects sites in this energy transfer process will be a subject of the future structural and spectroscopic studies. Nevertheless, a shift of DAP emission band and a change in the DAP vs. Eu^{3+} emission intensity ratio with doping concentration allow for tuning of the PL chromaticity of these samples, and their application as phosphors and luminescent probes.

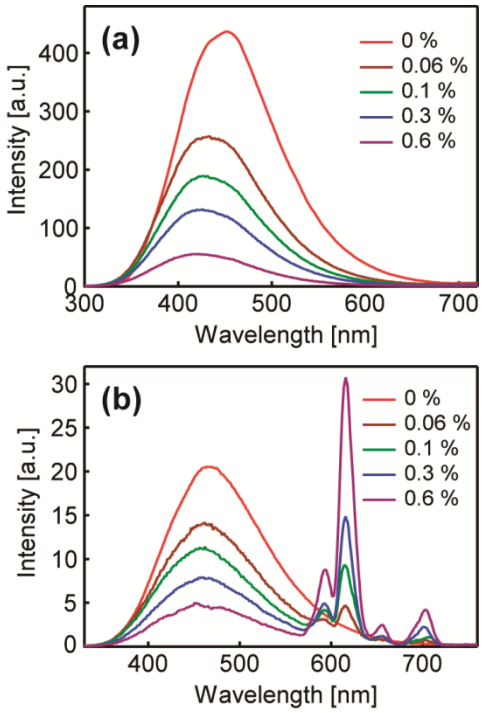

Figure 5.6 (a) Steady-state PL spectra of undoped and Eu^{3+}-doped Ga_2O_3 NCs. (b) Time-gated PL spectra of the same samples (delay time, 0.1 ms; gate time, 5 ms). Excitation wavelength in (a) and (b) was 230 nm, and the doping concentrations corresponding to the spectra are indicated in the graphs. The concentration of NCs in all measured samples was identical, based on the absorption spectra.

Importantly, the emission chromaticity can also be tuned dynamically over a period of several milliseconds. As evident from **Figure 5.6**, the DAP PL band energy and the DAP/Eu^{3+} intensity ratio also change as a function of the delay time. This temporally-tunable dual emission is possible owing to the comparable decay rates of the DAP and Ln^{3+} luminescence. In contrast to Ga_2O_3 NCs, majority of the semiconductor NC host lattices have much shorter PL lifetime (ns-μs), determined by the exciton recombination probability. The fact that PL dynamics in Ga_2O_3 is determined by inter-site electron transfer makes colloidal Eu^{3+}-doped Ga_2O_3 NCs a unique photophysical system. **Figure 5.7a** shows the DAP PL decay as a function of time for Eu^{3+}-doped γ-Ga_2O_3 having different doping concentrations (0-0.6 mol%). This emission decay dynamics and its size dependence have been theoretically modeled and explained in the context of the DAP recombination model. The key parameters determining the PL decay rate are an average separation between donors and acceptors (determined by NC size and preparation conditions), and the native defect locale (internal in bulk vs surface segregated in NCs). The rate of the DAP emission decay increases with increasing doping concentration, with the half-life ranging from 5.67 μs for undoped NCs to 4.21 μs for 0.6 mol% Eu^{3+}-doped NCs (**Table 5.1**). The decrease in the decay rate is related to a decrease in the average NC size (**Figures 5.1** and **Figures 5.2**), and increased quenching of the DAP emission by energy transfer to Eu^{3+} dopants. The latter process may be further enhanced by increased probability of dopant-donor association with increasing doping concentration. Time decay curves for Eu^{3+} emission were obtained by monitoring $^5D_0 \rightarrow {}^7F_2$ peak (at 615 nm) following NC band gap excitation (**Figure 5.3b**). The emission decays are well fit to a biexponential function, and the fitting parameters are listed in **Table 5.2**. The results of this biexponential fitting are used for generic determination of lifetimes for comparative purposes, assuming that the lifetimes are predominantly determined by the intrinsic decay time of the excited Eu^{3+}.The two time constants, τ_1 and τ_2, could be tentatively attributed to Eu^{3+} ions in the interior of NCs and near the NC surfaces, respectively. Emission of the Eu^{3+} close to the NC surfaces may undergo vibrational quenching and exhibit faster decay. For 1 mol%

Eu^{3+}-doped NCs, the average lifetime (τ) obtained by biexponential fitting is ca.1.7ms. With increasing doping concentration this lifetime increases to 1.9 ms for 5 mol% Eu^{3+}, and 2.1ms for 7 mol% Eu^{3+}. An increase in the lifetime of Eu^{3+} emission indicates an increase in the PL efficiency with increasing doping concentration, and suggests that a large fraction of Eu^{3+} ions are isolated and protected from cross relaxation and vibrational quenching even at high doping concentrations. Furthermore, the time constants of the Eu^{3+} emission decay in Ga_2O_3 NCs are large in comparison to those in other oxide NC lattices, confirming exceptionally high efficiency of Eu^{3+} emission [30,31]. A plausible explanation of an increase in the Eu^{3+} sensitization with increasing doping concentration is an increased probability of dopant-oxygen vacancy (donor) association, which can directly determine the energy transfer probability.

Table 5.1 Half-Life of DAP Emission of Eu^{3+}-doped γ-Ga_2O_3 NCs for Different Doping Concentrations.

Eu^{3+} doping conc. (mol%)	half-life (μs)
0	5.67
0.06	5.18
0.1	4.70
0.3	4.56
0.6	4.21

Table 5.2 Fitting Parameters Obtained from Biexponential Fitting to Eu^{3+} PL Decays.

[Eu^{3+}] (%)	τ_1[a] (ms)	τ_2[a] (ms)	τ_{avg} (ms)
1	2.0 (82 %)	0.4 (18 %)	1.7
5	2.7 (62 %)	0.6 (38 %)	1.9
7	2.9 (62 %)	0.7 (38 %)	2.1

[a]The percentages in parentheses indicate the contributions of the corresponding lifetime components to the PL decay.

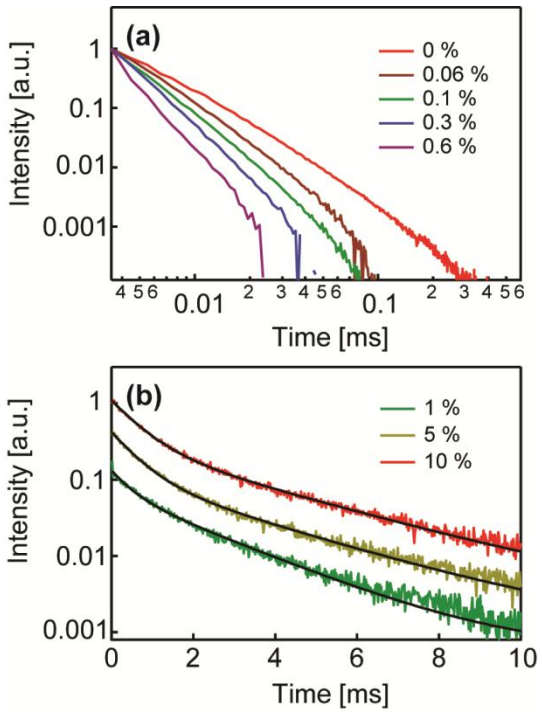

Figure 5.7 PL decay curves of Eu^{3+}-doped Ga_2O_3 NCs, monitored at the maximum of (a) DAP band, and (b) Eu^{3+} $^5D_0 \rightarrow {}^7F_2$ emission (615 nm). The excitation wavelength in (a) and (b) was 230 nm, and Eu^{3+} doping concentrations corresponding to the spectra are indicated in the graphs.

These results imply the possibility of broadly tuning the PL chromaticity not only via doping concentration and NC size, but also as a function of the delay time or gate time over the lifetime of the NC PL. **Figure 5.8a** shows delayed PL spectra of 0.1 mol% Eu^{3+}-doped Ga_2O_3 NCs for the delay time ranging from 0.1 to 1.7ms. At short delay times the spectra are dominated by the intense blue DAP emission. This emission decays significantly faster than the Eu^{3+} emission at this timescale, as evident from **Figure 5.8a**, and with the delay of 0.3 ms in the given experimental set-up the intensities of the DAP and Eu^{3+} ($^5D_0 \rightarrow {}^7F_2$)emissions are nearly equal. With further increase in the delay time Eu^{3+} emission begins to dominate, and the spectra become gradually more weighted in red. The colors of this sample at different delay times are represented by using International Commission on Illumination (CIE) diagram in **Figure 5.8b**. The coordinates were calculated from the corresponding spectra (**Table 5.3**), and the points in **Figure**

5.8b designate the delay times. The emission color varies from blue to red with increasing delay time, based on the spectral changes in **Figure 5.8a**. This dynamic dual emission-based color

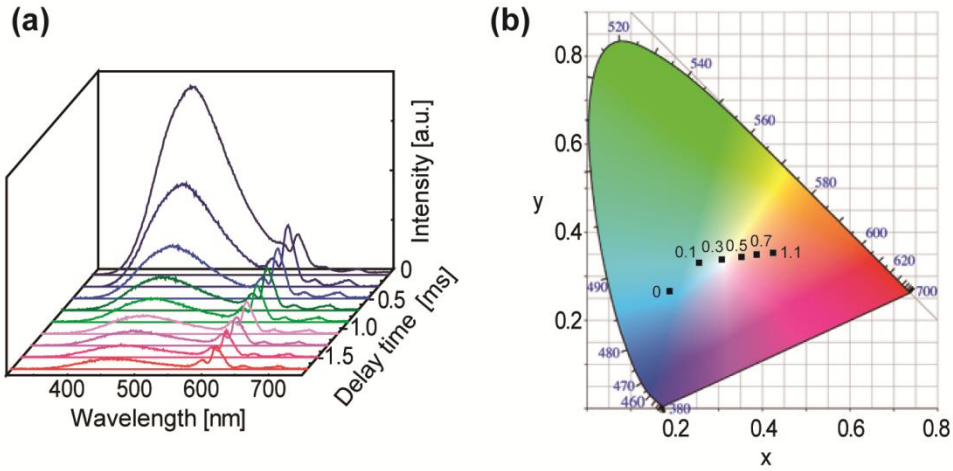

Figure 5.8 (a) Time-gated PL spectra of 0.1 mol% Eu^{3+}-doped Ga_2O_3 NCs for different delay times (the gate time was set to 0.2 ms).Intensity of the first spectrum (0.1 ms delay) is scaled down by a factor of 2.5 for clarity. (b)The CIE chromaticity diagram showing x-y color coordinates(black squares) corresponding to the spectra in (a). The points indicate sample chromaticity for different delay times (in ms), as indicated in the graph.

Table 5.3 CIE Color Coordinates (*x*, *y*) of 0.1 mol% Eu^{3+}-Doped γ-Ga_2O_3 NCs for Varying Delay Times Calculated from the PL Spectra in Figure 5.8b.

delay time (ms)	*x*	*y*
0 (steady-state)	0.210	0.268
0.1	0.274	0.335
0.3	0.338	0.337
0.5	0.385	0.341
0.7	0.414	0.345
1.1	0.451	0.349
1.7	0.475	0.352

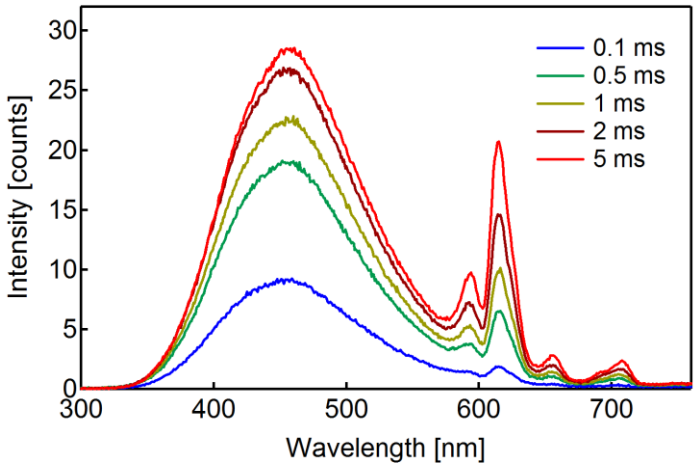

Figure 5.9 Time-gated PL spectra of 0.1 mol% Eu^{3+}-doped Ga_2O_3 NCs, collected for different gate times (0.1, 0.5, 1, 2, and 5 ms). Delay time set to 0.1 ms.

tunability is enabled by sufficiently large difference between the PL decay rate of the blue DAP and red Eu^{3+} emission at the micro-to-millisecond timescale. Similarly, given the dynamic nature of the dual emission on the same time regime, color tuning can also be achieved by changing the gate time (**Figure 5.9**). Although Ln^{3+}doping concentration-induced color change of Ln^{3+}-doped NCs has been reported [46], this dynamic color tunability based on wavelength positions and intensity ratio of the dual emission is a novel phenomenon of potential interest in photonic devices and biological assays.

To demonstrate wide applicability of colloidal Ga_2O_3 NCs as a host lattice for an effective sensitization and protection of Ln^{3+} dopants, and for dynamic tuning of the PL chromaticity of doped NCs, we prepared Tb^{3+}-doped Ga_2O_3 NCs by the same method. **Figure 5.10a** shows steady-state (blue) and time-gated (green) PL spectra of 1 mol% Tb^{3+}-doped NCs, and the corresponding excitation spectra (dashed lines). Similarly to Eu^{3+}-doped NCs, the steady-state spectrum is strongly dominated by the DAP emission band, while in time-gated spectrum Tb^{3+} emission prevails (assignments of Tb^{3+} peaks are given in **Figure 5.11**). However, the intensity of Tb^{3+} emission is noticeably stronger than that of Eu^{3+}, indicating higher energy transfer efficiency. The sensitization of Tb^{3+} by the NC host lattice is also evident from the delayed excitation spectrum, which is identical to the steady-state excitation spectrum of the NC host lattice. The ratio of the DAP to Tb^{3+} emission intensity can be modulated in steady-state and time-gated

modes by adjusting the doping concentration (**Figure 5.10b** and 5.**10c**, respectively), thereby tuning the PL chromaticity. Finally, **Figure 5.10d** demonstrates dynamic tunability of the dual DAP–Tb^{3+} emission, analogously to Eu^{3+}-doped Ga_2O_3 NCs. The DAP emission is clearly quenched faster than in case of Eu^{3+}-doped Ga_2O_3 NCs, which is consistent with more efficient energy transfer to Tb^{3+} relative to Eu^{3+} dopants.

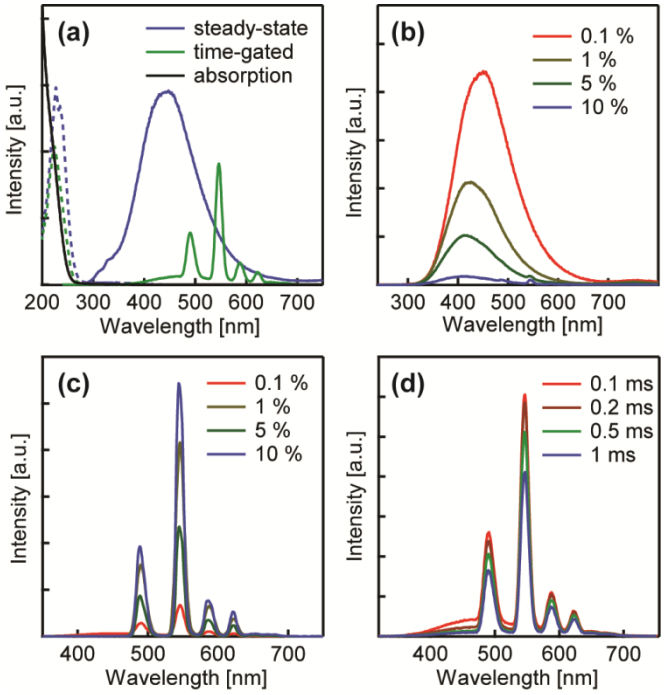

Figure 5.10 (a) Steady-state (blue) and time-gated (green) PL spectra of 1 mol% Tb^{3+}-doped Ga_2O_3 NCs (λ_{exc}=230 nm). The PL excitation spectra are shown with analogous colors as dashed lines; for steady-state spectrum (λ_{em}=435 nm), for time-gated spectrum (λ_{em}=545 nm). Time-gated spectra were collected with a delay time of 0.1 ms and gate-time of 5 ms. Absorption spectrum is shown with black trace. (b,c) Steady-state (b) and time-gated (c) PL spectra of Tb^{3+}-doped Ga_2O_3 NCs having different doping concentrations (as indicated in the graphs). The concentration of NCs in all samples was identical, and for time-gated spectra delay time was 0.1 ms, and gate time 5 ms. (d) Time-gated PL spectra of 0.1 mol% Tb^{3+}-doped Ga_2O_3 NCs for different delay times. The delay times are indicated in the graph, while the gate time was set to 0.2 ms.

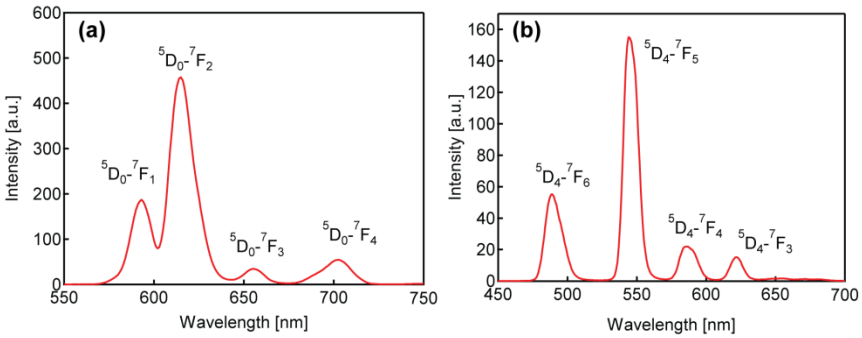

Figure 5.11 Time-gated PL spectrum of 10 mol% Eu^{3+} (a),Tb^{3+} (b)-doped Ga_2O_3 NCs, showing the assignment of the observed f-f transitions.

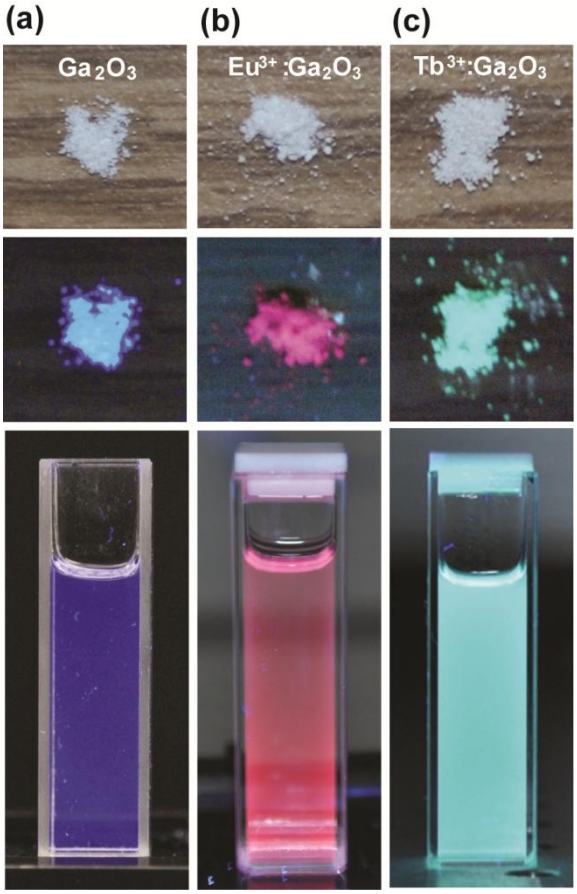

Figure 5.12 Photographs of (a) undoped γ-Ga_2O_3, (b) 7 mol% Eu^{3+}-doped Ga_2O_3, and (c) 10 mol% Tb^{3+}-doped Ga_2O_3 NCs. NC powders (top), NC powders illuminated with 250 nm light (middle), and colloidal NCs illuminated with 250 nm light (bottom).

Figure 5.12 illustrates the range of the emission colors and the versatility of potential applications of colloidal Ln^{3+}-doped Ga_2O_3 NCs. The undoped Ga_2O_3 NCs exhibit a strong deep-blue emission (**Figure 5.12**, left panel), which can be manipulated by substitutional incorporation of Ln^{3+} dopant ions. By doping Ln^{3+} ions into Ga_2O_3 NCs the center of gravity of the emission spectrum shifts to lower energies, changing the emission color to green for high Tb^{3+} concentration (right panel), and red for high Eu^{3+} doping concentration (middle panel). These systems enable a generation of the emission of the three basic spectral colors, which can be fine-tuned by changing NC size and Ln^{3+} doping concentration. Furthermore, these NCs are highly versatile and can be used in a colloidal form, for incorporation into functional structures and devices from the solution phase, or in a powder form as solid-state phosphors. They are also completely transparent to visible light and their emission is sufficiently bright (compared with the lanthanide doped In_2O_3 NCs with the same experimental procedure, Ga_2O_3 lattice showed 8-10 times intensity increase) even in the daylight, allowing for their integration with other photonic and opto-electronics materials and devices.

5.4 Conclusion

In summary, we synthesized a series of colloidal lanthanide (Ln^{3+})-doped γ-Ga_2O_3 NCs having different doping concentrations, and studied their photophysical properties using steady-state and time-resolved PL measurements. By using Eu^{3+}-doped Ga_2O_3 NCs as a model system, we showed that the Ln^{3+} dopants experience a strong sensitization by the NC host lattice, evidenced by the characteristic intra-4f orbital emission upon excitation of the NCs band gap transition. The strong Eu^{3+} sensitization indicates an effective energy transfer from the NC host lattice to the dopant ions. As a result, Eu^{3+}-doped Ga_2O_3 NCs exhibit the luminescence associated with both DAP and Eu^{3+} (f-f) emission and this unique dual emission is the central theme of this article. The energy of the DAP emission and the dual emission intensity ratio can be tuned by changing NC size and doping concentration. This interdependence of NC size, doping concentration, and defect (donor and acceptor) formation allows for a modulation of the emission color (chromaticity) over a broad range. With increasing doping concentration, the DAP emission is gradually quenched while the Eu^{3+} emission increases, owing to the efficient energy transfer. Another unique feature of this system is a difference between the decays of DAP and Eu^{3+} emissions on the millisecond timescale, which enables dynamic tuning of the dual emission. By changing the delay time or

gate time, the emission color of these colloidal NCs can be gradually tuned from blue to red. The generality of these results was demonstrated by using Tb^{3+}-doped Ga_2O_3 NCs, suggesting potential application of these Ln^{3+}-based materials in different optical technologies, such as bioimaging, light emitting devices, and photonics.

The results of this work expand the range of host NCs for sensitization of luminescent Ln^{3+} dopants, and help understand the mechanism of Ln^{3+} sensitization in NC lattices. Native defects, particularly oxygen vacancies, likely play a central role in the energy transfer from the NC host lattice to the Ln^{3+} dopant centers. The oxygen vacancies also form shallow donor states, and as such are responsible for both Ln^{3+} and the DAP emission in Ga_2O_3 NCs. These functional native defects have been implicated in a host of other properties, including electrical conductivity and catalytic activity (such as propane dehydrogenation, methane oxidation), making Ln^{3+}-doped Ga_2O_3 NCs generally very promising class of multifunctional materials for a variety of possible applications.

Chapter 6 Conclusions

The overall goal of this thesis was to synthesis new kinds of TCO materials at nanoscale with controlled size and structure and investigates their optical properties. In particular, this thesis emphasized controlled synthesis of monodispersed colloidal TCO NCs via a simple solution method. In addition, this thesis described the optical features of these TCO NCs. The conclusions of each part of the thesis (ITO, γ-phase Ga_2O_3, lanthanide doped γ-phase Ga_2O_3) are provided below.

In **chapter 2**, we studied colloidal Sn^{4+} doped In_2O_3 (ITO) NCs having different crystal structures. Tin precursor prohibited the NC growth, causing bimodal size distribution (NCs below ca. 5 nm in size have corundum crystal structure, while larger NCs have cubic bixbyite structure). Cubic bixbyite ITO NCs exhibited strong absorption in the NIR region which was a result of the resonant plasmon oscillations arising from the free conduction band electrons in *bcc*-ITO NCs and can be described by the Drude model of the free electron gas. *rh*-ITO NCs did not exhibit a significant absorption in the NIR. The difference between the free electron concentrations in *bcc*- and *rh*-ITO NCs arises from a different electronic structure of the donor states in these two NC phases.

Chapter 3 described the first size-controlled synthesis of colloidal γ-Ga_2O_3 NCs and demonstrated size tunable PL from UV to blue. Also, we demonstrated in situ control of the native defect formation in colloidal NCs in solution, and chemical manipulation of the optical properties of NCs. The long lifetime photoluminescence of the NCs arises from defects induced donor-acceptor pair recombination. These defects are also responsible for electrical conductivity of the NCs. These NCs with tunable optical emission is very promising for application in multifunctional optoelectronic materials and devices. For further understanding the light emitting properties of colloidal γ-Ga_2O_3 NCs, in **chapter 4**, PL mechanism of colloidal Ga_2O_3 NCs and the effect of NC size, structure, and surface modification on its efficiency and dynamics were investigated. This emission arises from DAP recombination and is sensitive to defect concentration. The lifetime of the DAP emission is sensitive to donor acceptor distance. The temperature dependent PL studies suggest that the donor binding energy increases with decreasing NC size.

In **chapter 5**, we demonstrated synthesis of lanthanide doped colloidal γ-Ga_2O_3 NCs with different doping levels. Optical characterization was carried out on colloidal suspensions of these NCs using steady state and time-gated luminescence measurements. With increasing initial doping level, defect based DAP emission quenches while sharp narrow Eu^{3+} emission increases. Time decay curves and delayed PL with different delay times show blue DAP emission with a life time about 4-5 μs while Eu^{3+} emission with a life time in the 1-3 ms range. By changing the delay time, the emission color of these NCs colloidal suspension can be gradually tuned from blue to red. These NCs with time tunable dual emission may have potential applications in bio-labeling, gas sensing, and other optical devices.

Copyright Permissions

Title: Size-Tunable Phosphorescence in Colloidal Metastable γ-Ga2O3 Nanocrystals
Author: Ting Wang, Shokouh S. Farvid, Mutalifu Abulikemu, and Pavle V. Radovanovic
Publication: Journal of the American Chemical Society
Publisher: American Chemical Society
Date: Jul 1, 2010 Copyright © 2010, American Chemical Society Logged in as: Ting Wang

Title: Size-Dependent Electron Transfer and Trapping in Strongly Luminescent Colloidal Gallium Oxide Nanocrystals
Author: Ting Wang and Pavle V. Radovanovic
Publication: The Journal of Physical Chemistry C
Publisher: American Chemical Society
Date: Sep 1, 2011 Copyright © 2011, American Chemical Society Logged in as: Ting Wang

Title: Free Electron Concentration in Colloidal Indium Tin Oxide Nanocrystals Determined by Their Size and Structure
Author: Ting Wang and Pavle V. Radovanovic
Publication: The Journal of Physical Chemistry C
Publisher: American Chemical Society
Date: Jan 1, 2011 Copyright © 2011, American Chemical Society Logged in as: Ting Wang

PERMISSION/LICENSE IS GRANTED FOR YOUR ORDER AT NO CHARGE This type of permission/license, instead of the standard Terms & Conditions, is sent to you because no fee is being charged for your order. Please note the following: Permission is granted for your request in both print and electronic formats, and translations. If figures and/or tables were requested, they may be adapted or used in part. Please print this page for your records and send a copy of it to your publisher/graduate school. Appropriate credit for the requested material should be given as follows: "Reprinted (adapted) with permission from (COMPLETE REFERENCE CITATION). Copyright (YEAR) American Chemical Society." Insert appropriate information in place of the capitalized words. One-time permission is granted only for the use specified in your request. No additional uses are granted (such as derivative works or other editions). For any other uses, please submit a new request.

References for chapter 1

(1) Pan, Z. W.; Dai, Z. R.; Wang, Z. L. *Science* **2001**, *291*, 1947.

(2) Farvid, S. S.; Dave, N.; Radovanovic, P. V. *Chem. Mater.* **2009**, *22*, 9.

(3) Lorenz, M. R.; Woods, J. F.; Gambino, R. J. *J. Phys. Chem. Solids* **1967**, *28*, 403.

(4) Blasse, G.; Bril, A. *J. Phys. Chem. Solids* **1970**, *31*, 707.

(5) Harwig, T.; Kellendonk, F. *J. Solid State Chem.* **1978**, *24*, 255.

(6) Vanithakumari, S. C.; Nanda, K. K. *Adv Mater* **2009**, *21*, 3581.

(7) Arnold, S. P.; Prokes, S. M.; Perkins, F. K.; Zaghloul, M. E. *Appl. Phys. Lett.* **2009**, *95*, 103102.

(8) Yang, H.; Shi, R.; Yu, J.; Liu, R.; Zhang, R.; Zhao, H.; Zhang, L.; Zheng, H. *J. Phys.Chem. C* **2009**, *113*, 21548.

(9) Badeker, K. *Ann. Phys.-Berlin* **1907**, *22*, 749.

(10) Groth, R.; Kauer, E. *Philips Technical Review* **1965**, *26*, 105.

(11) Simonis, F.; van der Leij, M.; Hoogendoorn, C. J. *Sol. Energy Mater* **1979**, *1*, 221.

(12) Drude, P. *Ann. Phys.-Berlin* **1900**, *308*, 369.

(13) Gordon, R. G. *Mrs Bull* **2000**, *25*, 52.

(14) Coutts, T. J.; Young, D. L.; Li, X. *Mrs Bull* **2000**, *25*, 58.

(15) Manifacier, J. C.; De Murcia, M.; Fillard, J. P.; Vicario, E. *Thin Solid Films* **1977**, *41*, 127.

(16) Mott, N. F. *Philos. Mag* **1961**, *6*, 287.

(17) Hamberg, I.; Granqvist, C. G. *J. Appl. Phys.* **1986**, *60*, R123.

(18) Köstlin, H.; Jost, R.; Lems, W. *phys. status solidi (a)* **1975**, *29*, 87.

(19) Blakemore, J. S. *J. Appl. Phys.* **1982**, *53*, R123.

(20) Seto, J. Y. W. *J. Appl. Phys.* **1975**, *46*, 5247.

(21) Dingle, R. B. *Philos. Mag* **1955**, *46*, 831.

(22) Pisarkiewicz, T.; Zakrzewska, K.; Leja, E. *Thin Solid Films* **1989**, *174, Part 1*, 217.

(23) Kim, H.; Horwitz, J. S.; Kushto, G. P.; Qadri, S. B.; Kafafi, Z. H.; Chrisey, D. B. *Appl. Phys. Lett.* **2001**, *78*, 1050.

(24) Kim, H.; Horwitz, J. S.; Piqué, A.; Gilmore, C. M.; Chrisey, D. B. *Applied Physics A: Materials S.* **1999**, *69*, S447.

(25) Burstein, E. *Phys. Rev.* **1954**, *93*, 632.

(26) Feldmann, C.; Jüstel, T.; Ronda, C. R.; Schmidt, P. J. *Adv. Func. Mater.* **2003**, *13*, 511.

(27) Novotny, V. *Can. J. Phys* **1969**, *47*, 1971.

(28) Thomas, D. G.; Hopfield, J. J.; Augustyniak, W.M. *Phys. Rev.* **1965**, *140*, A202.

(29) Herbert, D. C. *Semiconductor Science and Tech.* **1996**, *11*.

(30) Colbow, K. *Phys. Rev.* **1966**, *141*, 742.

(31) Colbow, K. *Phys. Rev.* **1965**, *139*, A274.

(32) Binet, L.; Gourier, D. *J. Phys. Chem. Solids* **1998**, *59*, 1241.

(33) Song, Y. P.; Zhang, H. Z.; Lin, C.; Zhu, Y. W.; Li, G. H.; Yang, F. H.; Yu, D. P. *Phys. Rev. B* **2004**, *69*, 075304.

(34) Harwig, T.; Kellendonk, F.; Slappendel, S. *J. Phys. Chem. Solids* **1978**, *39*, 675.

(35) Vetter, U. *Lanthanide Doped Wide Band Gap Semiconductors: Intra-4f Luminescence and Lattice Location Studies*, 2003.

(36) Ronda, C. R. In *Luminescence*; Wiley-VCH Verlag GmbH & Co. KGaA: 2007, p 1.

(37) Morss, L. R.; Edelstein, N. M.; Fuger, J.; Katz, J. J. *The Chemistry of the Actinide and Transactinide Elements*; Springer, 2011.

(38) Godlewski, M.; Świątek, K.; Suchocki, A.; Langer, J. M. *J. Lumin.* **1991**, *48*, 23.

(39) Dorenbos, P. *J. Lumin.***2003**, *104*, 239.

(40) Dorenbos, P. *J. Alloys Compd.* **2002**, *341*, 156.

(41) Dorenbos, P. *J. Lumin.***2002**, *99*, 283.

(42) Dorenbos, P. *J. Phys.: Condens. Matter* **2003**, *15*, 4797.

(43) Eliseeva, S. V.; Bunzli, J.-C. G. *Chem. Soc. Rev.* **2010**, *39*, 189.

(44) Tanner, P. A.; Hänninen, P., Härmä, H., Eds.; Springer Berlin Heidelberg: **2011**; Vol. 7, 183.

(45) Werts, M. H. V.; Jukes, R. T. F.; Verhoeven, J. W. *Phys. Chem. Chem. Phys* **2002**, *4*, 1542.

(46) Mukherjee, P.; Shade, C. M.; Yingling, A. M.; Lamont, D. N.; Waldeck, D. H.; Petoud, S. P. *J. Phys.Chem. A* **2010**, *115*, 4031.

(47) Ennen, H.; Schneider, J.; Pomrenke, G.; Axmann, A. *Appl. Phys. Lett.* **1983**, *43*, 943.

(48) Asoka-Kumar, P.; Lynn, K. G.; Welch, D. O. *J. Appl. Phys.* **1994**, *76*, 4935.

(49) Edgar, A.; Kasap, S., Capper, P., Eds.; Springer US: 2007, p 983.

(50) Lozykowski, H. J. *Phys. Rev. B* **1993**, *48*, 17758.

(51) Braud, A.; O'Donnell, K., Dierolf, V., Eds.; Springer Berlin / Heidelberg: 2010; Vol. 124, p 269.

(52) Förster, T. *Ann. Phys. Leipzig* **1948**, *437*, 55.

(53) Dexter, D. L. *J. Chem. Phys.* **1953**, *21*, 836.

(54) Clabau, F.; Rocquefelte, X.; Le Mercier, T.; Deniard, P.; Jobic, S.; Whangbo, M. H. *Chem.Mater.* **2006**, *18*, 3212.

References for chapter 2

(1) Beaulac, R.; Ochsenbein, S. T.; Gamelin, D. R. *Colloidal Transition-Metal-Doped Quantum Dots. In Nanocrystal Quantum Dots*, 2nd ed.; Klimov, V. I., Ed.; CRC Press: Boca Raton, FL, 2010; pp 397.

(2) Norris, D. J.; Efros, A. L.; Erwin, S. C. *Science* **2008**, *319*, 1776.

(3) Bhargava, R. N.; Gallagher, D.; Hong, X.; Nurmikko, A. *Phys.Rev. Lett.* **1994**, *72*, 416.

(4) Bol, A. A.; Meijerink, A. *Phys. Rev. B* **1998**, *58*, 15997.

(5) Levy, L.; Feltin, N.; Ingert, D.; Pileni, M.-P. *Langmuir* **1999**, *15*, 3386.

(6) Hoffman, D. M.; Meyer, B. K.; Ekimov, A. I.; Merkulov, I. A.; Efros, A. L.; Rosen, M.; Counio, G.; Gacoin, T.; Boilot, J.-P. *Solid State Commun.* **2000**, *114*, .

(7) Mikulec, F. V.; Kuno, M.; Bennati, M.; Hall, D. A.; Griffin, R. G.; Bawendi, M. G. *J. Am. Chem. Soc.* **2000**, *122*, 2532.

(8) Magana, D.; Perera, S. C.; Harter, A. G.; Dalal, N. S.; Strouse, G. F. *J. Am. Chem. Soc.* **2006**, *128*, 2931.

(9) Norris, D. J.; Yao, N.; Charnock, F. T.; Kennedy, T. A. *Nano Lett.* **2001**, *1*, 3.

(10) Erwin, S. C.; Zu, L.; Haftel, M. I.; Efros, A. L.; Kennedy, T. A.; Norris, D. J. *Nature* **2005**, *436*, 91.

(11) Beaulac, R.; Schneider, L.; Archer, P. I.; Bacher, G.; Gamelin, D. R. *Science* **2009**, *325*, 973.

(12) Nag, A.; Chakraborty, S.; Sarma, D. D. *J. Am. Chem. Soc.* **2008**, *130*, 10605.

(13) Archer, P. I.; Santangelo, S. A.; Gamelin, D. R. *J. Am. Chem. Soc.* **2007**, *129*, 9808.

(14) Farvid, S. S.; Dave, N.; Wang, T.; Radovanovic, P. V. *J. Phys.Chem. C* **2009**, *113*, 15928.

(15) Radovanovic, P. V.; Norberg, N. S.; McNally, K. E.; Gamelin, D. R. *J. Am. Chem. Soc.* **2002**, *124*, 15192.

(16) Bryan, J. D.; Heald, S. M.; Chambers, S. A.; Gamelin, D. R. *J. Am. Chem. Soc.* **2004**, *126*, 11640.

(17) Riwotzki, K.; Haase, M. *J. Phys. Chem. B* **1998**, *102*, 10129.

(18) Heer, S.; Kompe, K.; Gudel, H.-U.; Haase, M. *Adv. Mater.* **2004**, *16*, 2102.

(19) Farvid, S. S.; Ju, L.; Worden, M.; Radovanovic, P. V. *J. Phys. Chem. C* **2008**, *112*, 17755.

(20) Radovanovic, P. V.; Gamelin, D. R. *Phys. Rev. Lett.* **2003**, *91*, 157202.

(21) Ogale, S. B.; Choudhary, R. J.; Buban, J. P.; Lofland, S. E.; Shinde, S. R.; Kale, S. N.; Kulkarni, V. N.; Higgins, J.; Lanci, C.; Simpson, J. R.; Browning, N. D.; Das Sarma, S.; Drew, H. D.; Greene, R. L.; Venkatesan, T. *Phys. Rev. Lett.* **2003**, *91*, 077205.

(22) Ronning, C.; Gao, P. X.; Ding, Y.; Wang, Z. L. *Appl. Phys. Lett.* **2004**, *84*, 783.

(23) Chambers, S. A.; Thevuthasan, S.; Farrow, R. F. C.; Marks, R. F.; Thiele, J. U.; Folks, M. G.; Samant, M. G.; Kellock, J.; Ruzycki, N.; Ederer, D. L.; Diebold, U. *Appl. Phys. Lett.* **2001**, *79*, 3467.

(24) Kanehara, M.; Koike, H.; Yoshinaga, T.; Teranishi, T. *J. Am. Chem. Soc.* **2009**, *131*, 17736.

(25) Nutz, T.; zum Felde, U.; Haase, M. *J. Chem. Phys.* **1999**, *110*, 12142.

(26) Buhler, G.; Tholmann, D.; Feldmann, C. *Adv. Mater.* **2007**, *19*, 2224.

(27) Gilstrap, R. A.; Capozzi, C. J.; Carson, C. G.; Gerhardt, R. A.; Summers, C. J. *Adv. Mater.* **2008**, *20*, 4163.

(28) Ba, J.; Fattakhova Rohlfing, D.; Feldhoff, A.; Brezesinski, T.; Djerdj, I.; Wark, M.; Niederberger, M. *Chem. Mater.* **2006**, *18*, 2848.

(29) Hamberg, I.; Granqvist, C. G. *J. Appl. Phys.* **1986**, *60*, R123.

(30) Choi, S.-I.; Nam, K. M.; Park, B. K.; Seo, W. S.; Park, J. T. *Chem. Mater.* **2008**, *20*, 2609.

(31) Lee, C. H.; Kim, M.; Kim, T.; Kim, A.; Paek, J.; Lee, J. W.; Choi, S.-Y.; Kim, K.; Park, J.-B.; Lee, K. *J. Am. Chem. Soc.* **2006**, *128*, 9326.

(32) Farvid, S. S.; Dave, N.; Radovanovic, P. V. *Chem. Mater.* **2010**, *22*, 9.

(33) Liu, Q.; Lu, W.; Ma, A.; Tang, J.; Lin, J.; Fang, J. *J. Am. Chem. Soc.* **2005**, *127*, 5276.

(34) Narayanaswamy, A.; Xu, H.; Pradhan, N.; Kim, M.; Peng, X. *J. Am. Chem. Soc.* **2006**, *128*, 10310.

(35) Seo, W. S.; Jo, H. H.; Lee, K.; Park, J. T. *Adv. Mater.* **2003**, *15*, 795.

(36) Gurlo, A.; Kroll, P.; Riedel, R. *Chem. Eur. J.* **2008**, *14*, 3306.

(37) The same products were obtained using anhydrous Sn^{4+} precursors, although generally with a greater ratio of small to large NCs. We have previously shown that the main reaction mechanism for the synthesis of In_2O_3 NCs by this method is hydrolysis, which involves the presence of the traces of water in the reaction mixture. Additional crystallization water introduced through the $SnCl_4 \cdot 5H_2O$ precursor speeds up the reaction rate, which in turn counteracts the inhibition in the NC nucleation and growth by the presence of dopant impurity ions.

(38) Wang, C. Y.; Dai, Y.; Pezoldt, J.; Lu, B.; Kups, T.; Cimalla, V.; Ambacher, O. *Cryst. Growth Des.* **2008**, *8*, 1257.

(39) Nadaud, N.; Lequeux, N.; Nanot, M.; Jove, J.; Roisnel, T. *J. Solid State Chem.* **1998**, *135*, 140.

(40) Singhal, A.; Achary, S. N.; Manjanna, J.; Jayakumar, O. D.; Kadam, R. M.; Tyagi, A. K. *J. Phys. Chem. C* **2009**, *113*, 3600.

(41) Gonzalez, G. B.; Cohen, J. B.; Hwang, J.-H.; Mason, T. O.; Hodges, J. P.; Jorgensen, J. D. *J. Appl. Phys.* **2001**, *89*, 2550.

(42) Pujilaksono, B.; Klement, U.; Nyborg, L.; Jelvestam, U.; Hill, S.; Burgard, D. *Mater. Charact.* **2005**, *54*, 1.

(43) Matsuoka, T.; Kuwata, J.; Fujita, Y.; Abe, A. *Jpn. J. Appl. Phys.* **1988**, *27*, L1199.

(44) Maestre, D.; Cremades, A.; Gregoratti, L.; Piqueras, J. *J. Phys. Chem. C* **2010**, *114*, 3411.

(45) T-Thienprasert, J.; Nukeaw, J.; Sungthong, A.; Porntheeraphat, S.; Singkarat, S.; Onkaw, D.; Rujirawat, S.; Limpijumnong, S. *Appl. Phys. Lett.* **2008**, *93*, 051903.

(46) Karazhanov, S. Z.; Ravindran, P.; Vajeeston, P.; Ulyashin, A.; Finstad, T. G.; Fjellvag, H. *Phys. Rev. B* **2007**, *76*, 075129.

(47) Tang, Z.; Kotov, N. A.; Giersig, M. *Science* **2002**, *297*, 237.

(48) Cho, K.-S.; Talapin, D. V.; Gaschler, W.; Murray, C. B. *J. Am. Chem. Soc.* **2005**, *127*, 7140.

(49) Shim, M.; Guyot-Sionnest, P. *J. Chem. Phys.* **1999**, *111*, 6955.

(50) Kosmulski, M.; Maczka, E.; Rosenholm, J. B. *J. Phys. Chem. B* **2002**, *106*, 2918.

(51) Fox, M. *Optical Properties of Solids*; Oxford University Press: New York, 2001.

(52) Mi, Y.; Odaka, H.; Iwata, S. *Jpn. J. Appl. Phys.* **1999**, *38*, 3453.

(53) Rahnamaye Aliabad, H. A.; Hosseini, S. M.; Kompany, A.; Youssefi, A.; Attaran Kakhki, E. *Phys. Status Solidi B* **2009**, *246*, 1072.

(54) Mryasov, O. N.; Freeman, A. J. *Phys. Rev. B* **2001**, *64*, 233111.

(55) King, P. D. C.; Veal, T. D.; Fuchs, F.; Wang, C. Y.; Payne, D. J.; Bourlange, A.; Zhang, H.; Bell, G. R.; Cimalla, V.; Ambacher, O.; Egdell, R. G.; Bechstedt, F.; McConville, C. F. *Phys. Rev. B* **2009**, *79*, 205211.

(56) Walsh, A.; Da Silva, J. L. F.; Wei, S.-H.; Korber, C.; Klein, A.; Piper, L. F. J.; DeMasi, A.; Smith, K. E.; Panaccione, G.; Torelli, P.; Payne, D. J.; Bourlange, A.; Egdell, R. G. *Phys. Rev. Lett.* **2008**, *100*, 167402.

References for chapter 3

(1) Achermann, M.; Petruska, M. A.; Kos, S.; Smith, D. L.; Koleske, D. D.; Klimov, V. I. *Nature,* **2004**, *429*, 642.

(2) Talapin, D. V.; Murray, C. B. *Science*, **2005**, *310*, 86.

(3) Sambur, J. B.; Novet, T.; Parkinson, B. A. *Science*, **2010**, *330*, 63.

(4) Thurston, T. R.; Wilcoxon, J. P. *J. Phys. Chem. B*, **1999**, *103*, 11.

(5) Chan, W. C. W.; Nie, S. *Science*, **1998**, *281*, 2016.

(6) Bawendi, M. G.; Steigerwald, M. L.; Brus, L. E. *Annu. Rev. Phys. Chem.*, **1990**, *41*, 477.

(7) Norberg, N. S.; Gamelin, D. R. *J. Phys. Chem. B*, **2005**, *109*, 20810.

(8) Wang, T.; Farvid, S. S.; Abulikemu, M. and Radovanovic, P. V. *J. Am. Chem. Soc.*, **2010**, *132*, 9250.

(9) van Dijken, A.; Meulenkamp, E.A.; Vanmaekelbergh, D.; and Meijerink, A. *J. Lumin.*, **2000**, *90*, 123.

(10) Xiong, H.-M.; Shchukin, D. G.; Mohwald, H.; Xu, Y.; Xia, Y.-Y. *Angew. Chem., Int. Ed.*, **2009**, *48*, 2727.

(11) Wang, T.; Radovanovic, P. V. *J. Phys. Chem. C*, **2011**, *115*, 406.

(12) Samson, S.; Fonstad, C. G. *J. Appl. Phys*., **1973**, *44*, 4618.

(13) Lorenz, M. R.; Woods, J. F.; Gambino, R. J. *J. Phys. Chem. Solids*, **1967**, *28*, 403.

(14) Roy, R.; Hill, V. G.; Osborn, E. F. *J. Am. Chem. Soc.*, **1952**, *74*, 719.

(15) Binet, L.; Gourier, D. *J. Phys. Chem. Solids*, **1998**, *59*, 1241.

(16) Harwig, T.; Kellendonk, F. *J. Solid State Chem.*, **1978**, *24*, 255.

(17) Blasse, G.; Bril, A. *J. Phys. Chem. Solids*, **1970**, *31*, 707; Herbert, W. C.; Minnier, H. B.; Brown, J. J. Jr., *J. Electrochem. Soc.*, **1969**, *116*, 1019; Vanithakumari, S. C.; Nanda, K. K. *Adv. Mater.*, **2009**, *21*, 3581.

(18) Harwig, T.; Kellendonk, F.; Slappendel, S. *J. Phys. Chem. Solids*, **1978**, *39*, 675.

(19) Chen, T.; Tang, K. *Appl. Phys. Lett.*, **2007**, *90*, 053104.

(20) Nishi, K.; Shimizu, K.; Takamatsu, M.; Yoshida, H.; Satsuma, A.; Tanaka, T.; Yoshida, S.; Hattori, T. *J. Phys. Chem. B*, **1998**, *102*, 10190.

(21) Thomas, D. G.; Hopfield, J. J.; Augustyniak, W. M. *Phys. Rev.*, **1965**, *140*, A202.

(22) Dabbousi, B. O.; Rodriguez-Viejo, J.; Mikulec, F. V.; Heine, J. R.; Mattoussi, H.; Ober, R.; Jensen, K. F.; Bawendi, M. G. *J. Phys. Chem. B*, **1997**, *101*, 9463.

(23) Gill, J. E. *Photochem. Photobiol.* **1969**, *9*, 313.

References for chapter 4

(1) Hamberg, I.; Granqvist, C. G. *J. Appl. Phys*. **1986**, *60*, R123.

(2) Kilic, C.; Zunger, A. *Phys. Rev. Lett*. **2002**, *88*, 095501.

(3) Lorenz, M. R.; Woods, J. F.; Gambino, R. J. *J. Phys. Chem. Solids* **1967**, *28*, 403.

(4) Liu, W.; Xiu, F.; Sun, K.; Xie, Y.-H.; Wang, K. L.; Wang, Y.; Zou, J.; Yang, Z.; Liu, J. *J. Am. Chem. Soc.* **2010**, *132*, 2498.

(5) Wang, T.; Radovanovic, P.V. *J. Phys.Chem.C* **2011**, *115*, 406.

(6) Wang, T.; Farvid, S. S.; Abulikemu, M.; Radovanovic, P. V. *J. Am. Chem. Soc*. **2010**, *132*, 9250.

(7) Whitaker, K. M.; Ochsenbein, S. T.; Polinger, V. Z.; Gamelin, D. R. *J. Phys. Chem. C* **2008**, *112*, 14331.

(8) Meulenkamp, E. A. *J. Phys. Chem. B* **1998**, *102*, 5566.

(9) van Dijken, A.; Meulenkamp, E. A.; Vanmaekelbergh, D.; Meijerink, A. *J. Phys. Chem. B* **2000**, *104*, 1715.

(10) Farvid, S. S.; Dave, N.; Radovanovic, P. V. *Chem. Mater*. **2010**, *22*, 9.

(11) Zhang, H.; Banfield, J. F. *J. Mater. Chem* **1998**, *8*, 2073.

(12) Roy, R.; Hill, V. G.; Osborn, E. F. *J. Am. Chem. Soc*. **1952**, *74*, 719.

(13) Farvid, S. S.; Ju, L.; Worden, M.; Radovanovic, P. V. *J. Phys. Chem. C* **2008**, *112*, 17755.

(14) Philip, J.; Punnoose, A.; Kim, B. I.; Reddy, K. M.; Layne, S.; Holmes, J. O.; Satpati, B.; Leclair, P. R.; Santos, T. S.; Moodera, J. S. *Nat. Mater.* **2006**, *5*, 298.

(15) Matsumoto, Y.; Murakami, M.; Shono, T.; Hasegawa, T.; Fukumura, T.; Kawasaki, M.; Ahmet, P.; Chikyow, T.; Koshihara, S.; Koinuma, H. *Science* **2001**, *291*, 854.

(16) Schwartz, D. A.; Norberg, N. S.; Nguyen, Q. P.; Parker, J. M.; Gamelin, D. R. *J. Am. Chem. Soc.* **2003**, *125*, 13205.

(17) Radovanovic, P. V.; Gamelin, D. R. *Phys. Rev. Lett*. **2003**, *91*, 157202.

(18) Beaulac, R.; Ochsenbein, S.T.; Gamelin, D. R. *Colloidal Transition Metal Doped Quantum Dots. in Nanocrystal Quantum Dots*, 2nded.;Klimov, V. I., Ed.; CRC Press: Boca Raton, FL, 2010.

(19) Norris, D. J.; Efros, A. L.; Erwin, S.C. *Science* **2008**, *319*, 1776.

(20) Fu, Y.-S.; Du, X.-W.; Kulinich, S. A.; Qiu, J.-S.; Qin, W.-J.; Li, R.; Sun, J.; Liu, J. *J. Am. Chem. Soc.* **2007**, *129*, 16029.

(21) Kar, A.; Kundu, S.; Patra, A. *J. Phys. Chem. C* **2011**, *115*, 118.

(22) Norberg, N. S.; Gamelin, D. R. *J. Phys. Chem. B* **2005**, *109*, 20810.

(23) Nishi, K.; Shimizu, K.; Takamatsu, M.; Yoshida, H.; Satsuma, A.; Tanaka, T.; Yoshida, S.; Hattori, T. *J. Phys. Chem. B* **1998**, *102*, 10190.

(24) Geller, S. *J. Chem. Phys*. **1960**, *33*, 676.

(25) Harwig, T.; Kellendonk, F. *J. Solid State Chem.* **1978**, *24*, 255.

(26) Harwig, T.; Kellendonk, F.; Slappendel, S. *J. Phys. Chem. Solids* **1978**, *39*, 675.

(27) Binet, L.; Gourier, D. *J. Phys. Chem. Solids* **1998**, *59*, 1241.

(28) Blasse, G.; Bril, A. *J. Phys. Chem. Solids* **1970**, *31*, 707.

(29) Vanithakumari, S. C.; Nanda, K. K. *Adv. Mater.* **2009**, *21*, 3581.

(30) Song, Y. P.; Zhang, H. Z.; Lin, C.; Zhu, Y. W.; Li, G. H.; Yang, F. H.; Yu, D. P. *Phys. Rev. B* **2004**, *69*, 075304.

(31) Chen, T.; Tang, K. *Appl. Phys. Lett.* **2007**, *90*, 053104.

(32) Yoshioka, S.; Hayashi, H.; Kuwabara, A.; Oba, F.; Matsunaga, K.; Tanaka, I. *J. Phys.: Condens. Matter* **2007**, *19*, 346211.

(33) He, H.; Orlando, R.; Blanco, M. A.; Pandey, R.; Amzallag, E.; Baraille, I.; Rerat, M. *Phys. Rev. B* **2006**, *74*, 195123.

(34) Huppertz, H.; Hering, S. A.; Zvoriste, C. E.; Lauterbach, S.; Oeckler, O.; Riedel, R.; Kinski, I. *Chem. Mater*. **2009**, *21*, 2101.

(35) Farvid, S. S.; Wang, T.; Radovanovic, P. V. *J. Am. Chem. Soc.* **2011**, *133*, 6711.

(36) Dean, P. J. *Prog. Solid State Chem*. **1973**, *8*, 1.

(37) Thomas, D. G.; Hopfield, J. J.; Augustyniak, W. M. *Phys. Rev.* **1965**, *140*, A202.

(38) Nelson, D. F.; Rodgers, K. F. *Phys. Rev.* **1965**, *140*, A1667.

(39) Dave, N.; Pautler, B. G.; Farvid, S. S.; Radovanovic, P. V. *Nanotechnology* **2010**, *21*, 134023.

(40) Kisailus, D.; Choi, J. H.; Weaver, J. C.; Yang, W.; Morse, D. E. *Adv. Mater.* **2005**, *17*, 314.

(41) Cho, S.; Lee, J.; Park, I.-Y.; Kim, S. *Mater. Lett.* **2002**, *57*, 1004.

(42) Tsu, R.; Babic, D. *Appl. Phys. Lett.* **1994**, *64*, 1806.

(43) Lannoo, M.; Delerue, C.; Allan, G. *Phys. Rev. Lett.* **1995**, *74*, 3415.

(44) Fox, M. *Optical Properties of Solids*; Oxford University Press: New York, 2001.

(45) van Dijken, A.; Meulenkamp, E. A.; Vanmaekelbergh, D.; Meijerink, A. *J. Lumin.* **2000**, *90*, 123.

(46) This competition might be particularly relevant due to the proximity of donor and acceptor sites to the NC surfaces.

References for chapter 5

(1) Achermann, M.; Petruska, M. A.; Kos, S.; Smith, D. L.; Koleske, D. D.; Klimov, V. I. *Nature* **2004**, *429*, 642.

(2) Ganesh, N.; Zhang, W.; Mathias, P. C.; Chow, E.; Soares, J. A. N. T.; Malyarchuk, V.; Smith, A. D.; Cunningham, B. T. *Nat. Nanotechnol.* **2007**, *2*, 515.

(3) Klimov, V. I.; Mikhailovsky, A. A.; Xu, S.; Malko, A.; Hollingsworth, J. A.; Leatherdale, C. A.; Eisler, H.-J.; Bawendi, M. G. *Science* **2000**, *290*, 314.

(4) Anikeeva, P. O.; Halpert, J. E.; Bawendi, M. G.; Bulovic, V. *Nano Lett.* **2009**, *9*, 2532.

(5) Dai, J.; Ji, Y.; Xu, C. X.; Sun, X. W.; Leck, K. S.; Ju, Z. G. *Appl. Phys. Lett.* **2011**, *99*, 063112.

(6) Qian, L.; Zheng, Y.; Xue, J.; Holloway, P. H. *Nat. Photonics* **2011**, *5*, 543.

(7) Chan, W. C. W.; Nie, S. *Science* **1998**, *281*, 2016.

(8) Tanabe, S. In *Photonics Based on Wavelength Integration and Manipulation*; Tada, K., Ed.; IPAP Books: 2005; Vol. 2, p 101-112.

(9) Tanabe, S.; Fujita, S.; Yoshihara, S.; Sakamoto, A.; Yamamoto, S. *Proc. of SPIE* **2005**, *5941*, 594112.

(10) Dominguez, M.; Perez-Bernal, M. E.; Ruano-Casero, R. J.; Barriga, C.; Rives, V.; Ferreira, R. A. S.; Carlos, L. D.; Rocha, J. *Chem. Mater.* **2011**, *23*, 1993.

(11) Liu, Y.; Luo, W.; Zhu, H.; Chen, X. *J. Lumin.* **2011**, *131*, 415.

(12) Favennec, P. N.; L'Haridon, H.; Salvi, M.; Moutonnet, D.; Le Guillou, Y. *Electron. Lett.* **1989**, *25*, 718.

(13) Fujii, M.; Yoshida, M.; Hayashi, S.; Yamamoto, K. *J. Appl. Phys.* **1998**, *84*, 4525.

(14) Dai, Q.; Foley, M. E.; Breshike, C. J.; Lita, A.; Strouse, G. F. *J. Am. Chem. Soc.* **2011**, *133*, 15475.

(15) Park, Y.-K.; Han, J.-I.; Kwak, M.-G.; Yang, H.; Sung-Hoo, J.; Cho, W.-S. *J. Lumin.* **1998**, *78*, 87.

(16) Hanaoka, K.; Kikuchi, K.; Kobayashi, S.; Nagano, T. *J. Am. Chem. Soc.* **2007**, *129*, 13502.

(17) Tu, D.; Liu, L.; Ju, Q.; Liu, Y.; Zhu, H.; Li, R.; Chen, X. *Angew. Chem. Int. Ed.* **2011**, *50*, 6306 .

(18) Chen, G.; Ohulchanskyy, T. Y.; Liu, S.; Law, W.-C.; Wu, F.; Swihart, M. T.; Agren, H.; Prasad, P. N. *ACS Nano* **2012**, *6*, 2969.

(19) Eliseeva, S. V.; Bunzli, J.-C. G. *Chem. Soc. Rev.* **2010**, *39*, 189.

(20) Carnall, W. T.; Fields, P. R. In *Lanthanide/Actinide Chemistry*; Fields, P. R., Moeller, T., Eds.; American Chemical Society: Washington, D.C., 1967, p 86-101.

(21) Kropp, J. L.; Windsor, M. W. *J. Chem. Phys.* **1965**, *42*, 1599.

(22) Beeby, A.; Clarkson, I. M.; Dickins, R. S.; Faulkner, S.; Parker, D.; Royle, L.; de Sousa, A. S.; Gareth Williams, J. A.; Woods, M. *J. Chem. Soc., Perkin Trans. 2* **1999**, 493.

(23) Ronda, C. R. In *Luminescence: From Theory to Applications*; Ronda, C. R., Ed.; Wiley: Weinheim, 2008, p 1-34.

(24) Planelles-Arago, J.; Cordoncillo, E.; Ferreira, R. A. S.; Carlos, L. D.; Escribano, P. *J. Mater. Chem* **2011**, *21*, 1162.

(25) Chengelis, D. A.; Yingling, A. M.; Badger, P. D.; Shade, C. M.; Petoud, S. *J. Am. Chem. Soc.* **2005**, *127*, 16752.

(26) Mukherjee, P.; Shade, C. M.; Yingling, A. M.; Lamont, D. N.; Waldeck, D. H.; Petoud, S. *J. Phys. Chem. A* **2011**, *115*, 4031.

(27) Du, Y.-P.; Zhang, Y.-W.; Sun, L.-D.; Yan, C.-H. *J. Phys. Chem. C* **2008**, *112*, 12234.

(28) Li, L.; Tsung, C. K.; Yang, Z.; Stucky, G. D.; Sun, L. D.; Wang, J. F.; Yan, C. H. *Adv. Mater.* **2008**, *20*, 903.

(29) Tachikawa, T.; Ishigaki, T.; Li, J.-G.; Fujitsuka, M.; Majima, T. *Angew. Chem. Int. Ed.* **2008**, *47*, 5348.

(30) Frindell, K. L.; Bartl, M. H.; Robinson, M. R.; Bazan, G. C.; Popitsch, A.; Stucky, G. D. *J. Solid State Chem.* **2003**, *172*, 81.

(31) Vela, J.; Prall, B. S.; Rastogi, P.; Werder, D. J.; Casson, J. L.; Williams, D. J.; Klimov, V. I.; Hollingsworth, J. A. *J. Phys. Chem. C* **2008**, *112*, 20246.

(32) Yu, Y.; Chen, D.; Wang, Y.; Huang, P.; Weng, F.; Niu, M. *Phys. Chem. Chem. Phys* **2009**, *11*, 8774.

(33) Shimizu, K.-i.; Takamatsu, M.; Nishi, K.; Yoshida, H.; Satsuma, A.; Tanaka, T.; Yoshida, S.; Hattori, T. *J. Phys. Chem. B* **1999**, *103*, 1542.

(34) Ogita, M.; Higo, K.; Nakanishi, Y.; Hatanaka, Y. *Appl. Surf. Sci.* **2001**, *175–176*, 721.

(35) Zhu, H.; Li, R.; Luo, W.; Chen, X. *Phys. Chem. Chem. Phys* **2011**, *13*, 4411.

(36) Shen, W. Y.; Pang, M. L.; Lin, J.; Fang, J. *J. Electrochem. Soc.* **2005**, *152*, H25.

(37) Nogales, E.; Garcia, J. A.; Mendez, B.; Piqueras, J.; Lorenz, K.; Alves, E. *J. Phys. D: Appl. Phys.* **2008**, *41*, 065406.

(38) Wang, T.; Farvid, S. S.; Abulikemu, M.; Radovanovic, P. V. *J. Am. Chem. Soc.* **2010**, *132*, 9250.

(39) Wang, T.; Radovanovic, P. V. *J. Phys. Chem. C* **2011**, *115*, 18473.

(40) Wang, T.; Radovanovic, P. V. *Chem. Comm.* **2011**, *47*, 7161.

(41) Hegde, M.; Wang, T.; Miskovic, Z. L.; Radovanovic, P. V. *Appl. Phys. Lett.* **2012**, *100*, 141903.

(42) Bryan, J. D.; Gamelin, D. R. *Prog. Inorg. Chem.* **2005**, *54*, 47.

(43) Farvid, S. S.; Dave, N.; Wang, T.; Radovanovic, P. V. *J. Phys. Chem. C* **2009**, *113*, 15928.

(44) Clabau, F.; Rocquefelte, X.; Le Mercier, T.; Deniard, P.; Jobic, S.; Whangbo, M. H. *Chem. Mater.* **2006**, *18*, 3212.

(45) Clabau, F.; Rocquefelte, X.; Jobic, S.; Deniard, P.; Whangbo, M. H.; Garcia, A.; Le Mercier, T. *Chem. Mater.* **2005**, *17*, 3904.

(46) Wang, F.; Xue, X.; Liu, X. *Angew. Chem. Int. Ed.* **2008**, *47*, 906 .

(47) Dave, N.; Pautler, B. G.; Farvid, S. S.; Radovanovic, P. V. *Nanotechnology* **2010**, *21*, 134023.